Doctoral dissertation

A thesis submitted for the degree of

Doctor of Philosophy in Science

“Odor-functions map”
in the olfactory cortex subareas
characterized by distinct behavioral state signals

Yuta Tanisumi

Supervisor:

Dr. Yoshio Sakurai

Co-supervisor:

Dr. Hiroyuki Manabe

Dr. Junya Hirokawa

Graduate School of Brain Science, Doshisha University, Kyoto, Japan

March 2022

Abstract

The olfactory cortex (OC), which consists of some distinct subareas, receives both olfactory sensory signals from the olfactory bulb and top-down signals from higher-order regions. However, it remains unknown as to how each area of the OC encodes for sensory- and behavior-related information from higher-order regions. We addressed this issue in rodents, particularly focusing on four areas of the OC: the anterior piriform cortex (aPCx), ventral tenia tecta (vTT), nucleus of the lateral olfactory tract (NLOT), and anterior cortical amygdaloid nucleus (ACo). Using electrophysiological recordings in the OC subareas with an odor-guided go/no-go task, we found that each area showed unique behavioral state signals that were predicted by the cue odors (i.e., moving to the reward port, waiting for the reward, and drinking reward state).

First, aPCx, which is the most studied OC subarea, neurons responded to a specific combination of cue odors with increased firings during a specific state of the subsequent behaviors, possibly related to the communication between odor information and all behavioral states (**Chapter 3**). Our findings suggest that bottom-up and top-down communication exists in the OC, and we hypothesized that not only the aPCx but also the other subareas have their own unique top-down signal processing. As one of the candidate

sources of the top-down signals, we next focused on the vTT, which receives top-down projections from the medial prefrontal cortex (mPFC) and projects to the broad olfactory areas (**Chapter 4**). We found that individual vTT neurons tuned to a specific behavioral state, and the vTT state representations were degraded with optogenetic inactivation of the mPFC-to-vTT inputs. These suggest that vTT acts as a hub that sends context-dependent signals from the mPFC to broad olfactory areas.

To investigate how such top-down signals to the OC are distributed to the subareas, we finally focused on the NLOT and ACo, which are not only a part of the OC, but also a part of the cortical amygdala. Many NLOT neurons that selectively responded to go-cue odor also increased their firing rates during drinking reward, suggesting that the NLOT is involved in odor-reward association learning (**Chapter 5**). On the other hand, ACo neurons exhibited two types of reward anticipation signals: one neuron group type exhibited gradual increases in the signals to the reward, while the other type showed phasic anticipation signals, suggesting that the ACo is involved in odor-guided reward-directed learning (**Chapter 6**).

In conclusion, we propose a circuit model in which behavioral state signals are shared to the OC, and each subarea plays a distinct role in the formation of an “odor-functions map” based on the functions that lead to odor-evoked behaviors.

Acknowledgments

I would like to express my deepest gratitude to my supervisors, **Dr. Hiroyuki Manabe** and **Dr. Yoshio Sakurai** for their continuous guidance, scientific advice, and encouragement during the last 5 years. I’m grateful to **Dr. Junya Hirokawa**, **Dr. Kazuki Shiotani**, **Dr. Koshi Murata**, **Dr. Keiji Miura**, **Dr. Kensaku Mori**, and the past and present lab members for their encouragement and insightful comments on this research. Without them, this study would not have been possible. I would like to give special thanks to my thesis committee, **Dr. Susumu Takahashi**, **Dr. Hiroaki Misono**, and **Dr. Yoshito Masamizu** for their time and efforts in my examination. I’m also grateful to the Japan Society for the Promotion of Science (JSPS) and Doshisha University for their financial support and **Mr. Hideki Tanisumi** for providing mice illustrations for the various figures. Finally, I wish to extend my sincere gratitude to my family for their understanding, support, and encouragement. I don’t think I could have achieved this study without their dedication.

● Table of Contents

Chapter 1. General Introduction 14

1.1. What is odor? 14

1.2. What are odorant molecules? 15

1.3. Olfactory neural processing in the olfactory epithelium 16

1.4. Olfactory neural processing in the olfactory bulb 20

1.5. Olfactory neural processing in the olfactory cortex 31

1.6. Olfactory neural processing as links to higher functions 40

Chapter 2. Material and Methods 45

2.1. Animals 45

2.2. Apparatus 45

2.3. Behavioral task: Four odors-guided go/no-go task with rats (Chapter 3) ... 47

2.4. Behavioral task: Two odors-guided go/no-go task with mice (Chapter 4-6) 48

2.5. Electrophysiology 50

2.6. Data analyses: Spike sorting 51

2.7. Data analyses: Spike histograms 53

2.8. Data analyses: Receiver operating characteristic (ROC) analyses 54

2.9. Data analyses: Generalized linear models (GLM) 57

2.10. Data analyses: Population vector construction and analyses 58

2.11. Data analyses: Support vector machine (SVM) decoding analyses 59

2.12. Histology 60

2.13. *In situ* hybridization (Chapter 4) 60

2.14. Retrograde tracing (Chapter 4) 61

Chapter 3. Research: anterior piriform cortex (aPCx) in the OC 63

3.1. Short summary 63

3.2. Introduction 64

3.3. Results: Distributed cue odor representations and sequential behavioral state signals 66

3.4. Results: Associative correlation in the odor and behavioral state firings 74

3.5. Results: Changing formats of individual selective firing of odor and behavioral states during reversal learning 79

3.6. Results: Stable population coding in the aPCx during the completed learning period 85

3.7. Discussion 90

Chapter 4. Research: ventral tenia tecta (vTT) in the OC 94

4.1. Short summary 94

4.2. Introduction 94

4.3. Results: Activity of vTT neurons during the odor presentation phase of the odor-guided go/no-go task 96

4.4. Results: Behavior-specific activity of vTT cells in the odor-guided go/no-go task 102

4.5. Results: Behavioral context-dependent activity of vTT cells 107

4.6. Results: Cell types and connectivity patterns of vTT cells 111

4.7. Results: mPFC-to-vTT top-down input potentially shares behavioral state signals to the olfactory cortex 115

4.8. Discussion 118

Chapter 5. Research: nucleus of the lateral olfactory tract (NLOT) in the OC ... 122

5.1. Short summary 122

5.2. Introduction 122

5.3. Results: *In vivo* recording in the NLOT and the odor-guided go/no-go tasks 124

5.4. Results: Five-type classification of NLOT neurons based on odor-sampling epoch response 128

5.5. Results: Go-cue responsive neurons bi-directionally encode cue odors with excitations and suppressions.. 132

5.6. Results: NLOT neuron population exhibits rapid response dynamics before executing cue-odor-evoked behaviors.. 139

5.7. Results: NLOT neurons provided sufficient information to account for behavioral accuracy.. 145

5.8. Results: Bi-directional cue-outcome encoding following odor-guided behaviors 148

5.9. Discussion: Insights based on the results..................................... 153

5.10. Discussion: The hypothesis of the NLOT with layer-specific functional projections and future directions... 156

Chapter 6. Research: anterior cortical amygdaloid nucleus (ACo) in the OC 160

6.1. Short summary 160

6.2. Introduction 160

6.3. Results: Go-cue-odor preferred responses of ACo neurons during the late phase of odor-sampling epoch 162

6.4. Results: Late phase of go-cue odor preferred responses were evoked by the odor onsets and were stable across trials 167

6.5. Results: Response dynamics of the ACo neuron population during the late phase of odor-sampling epoch 172

6.6. Results: Two types of reward anticipation responses of ACo neurons 176

6.7. Results: Association of go-cue excitations with excitatory responses for the reward anticipation behavior 179

6.8. Discussion: Insights based on the results 183

6.9. Discussion: Two types of reward-related responses that are unique properties of the ACo 184

Chapter 7. General Discussion 188

7.1. "Odor-functions map" hypothesis in the OC 188

7.2. Anatomical evidence for the "odor-functions map" in the OC 196

7.3. Limitations and future direction 199

References 207

● List of Figures

Chapter 1

Figure 1-1 | Olfactory neural processing: Odorant receptors → olfactory sensory neurons in the olfactory epithelium 19

Figure 1-2 | Olfactory neural processing: Olfactory sensory neurons in the olfactory epithelium → olfactory bulb neurons 22

Figure 1-3 | Olfactory neural processing: Odor-molecule map in the olfactory bulb 27

Figure 1-4 | Olfactory neural processing: Olfactory bulb neurons → olfactory cortex subareas 35

Figure 1-5 | Schematic representation of the pattern of inputs and outputs of the olfactory cortex subareas described in the previous work, focusing on vTT, NLOT, and ACo. 37

Figure 1-6 | The previous accumulation of knowledge about anatomy, function, and neural recordings in the aPCx, vTT, NLOT, and ACo 39

Chapter 2

Figure 2-1 | An example of the spike sorting results 52

Chapter 3

Figure 3-1 | Electrophysiological recordings in the aPCx of freely moving rats performing the odor-guided go/no-go association task.................................71

Figure 3-2 | Distributed cue odor representations and sequential behavioral state signals...73

Figure 3-3 | Associative correlation in the odor and behavioral state firings 78

Figure 3-4 | Reversal learning of the odor-guided go/no-go association task 81

Figure 3-5 | Associative correlation in the odor and behavioral state firings after reversal learning..82

Figure 3-6 | Quantifying the firing change of the tuning profile and their speed in each state during reversal learning 84

Figure 3-7 | Stable population coding in the aPCx during the completed learning period 89

Chapter 4

Figure 4-1 | vTT cell activity patterns during the odor presentation phase of the odor-guided go/no-go task 100

Figure 4-2 | Tuning of vTT cells to distinct behaviors in the odor-guided go/no-go task 105

Figure 4-3 | Behavioral context-specific activity of vTT cells 109

Figure 4-4 | Cell types and connectivity patterns of vTT cells 114

Figure 4-5 | mPFC-to-vTT top-down input potentially shares behavioral state signals to the olfactory cortex 116

Chapter 5

Figure 5-1 | Odor-guided go/no-go task and the NLOT 127

Figure 5-2 | NLOT neuron activity patterns during the odor-guided go/no-go task 131

Figure 5-3 | Go-cue responsive neurons show phasic excitation to go-cue odor and persistent suppression to no-go-cue odor 136

Figure 5-4 | Go-cue excitation response triggered by odor onset rather than the initiation of an odor-guided behavior 138

Figure 5-5 | NLOT neuron population response before the initiation of odor-guided behaviors 143

Figure 5-6 | NLOT neurons provided sufficient information to account for behavioral choices 146

Figure 5-7 | NLOT neurons exhibits bidirectional cue-outcome encoding following odor-guided behaviors 152

Chapter 6

Figure 6-1 | Cue-Odor-preferred responses of ACo neurons during the late phase of odor-sampling in the odor-guided go/no-go task 166

Figure 6-2 | Late go-cue odor-preferred responses were evoked by the odor onsets and were stable 170

Figure 6-3 | Dynamics of ACo neuron population response during the late phase of odor-sampling 174

Figure 6-4 | Two types of reward-related responses of ACo neurons 178

Figure 6-5 | Waiting-selective neurons showed go-cue odor-preferred responses during odor-sampling 182

Chapter 7

Figure 7-1 | Summary: “Odor-functions map” hypothesis in the OC 193

Figure 7-2 | The accumulation of knowledge about anatomy, function, and neural recordings in the aPCx, vTT, NLOT, and ACo 195

● Abbreviations: olfactory neural circuits

OR; odorant receptor

OSN; olfactory sensory neuron

OB; olfactory bulb

AON; anterior olfactory nucleus

OC; olfactory cortex

aPCx; anterior piriform cortex

pPCx; posterior piriform cortex

vTT; ventral tenia tecta

NLOT; nucleus of the lateral olfactory tract

ACo; anterior cortical amygdaloid nucleus

OT; olfactory tubercle

LEC; lateral entorhinal cortex

Chapter 1. General Introduction

1.1. What is odor?

Flavor and aroma have a strong influence on the pleasure derived from food and drink. This can be felt by pinching the nose while eating or drinking; when the odor disappears, even the taste seems to have changed. To prepare good food, we need to learn how to make odors as well as taste, and the knowledge will make our daily diet more pleasant. The scents of flowers, incense, perfume, and freshly laundered shirts are good examples of how odors can lead to comfort and mental stability.

Meanwhile, fish, meat, fruits, and other foods decay over time and emit strange odors. The strange odor of food is regarded as a “danger signal” and leads to avoidance of eating. An example of another dangerous odor is volcanic gas that smells like sulfur; it is artificially added to the natural gas used as fuel, which is odorless, to make people aware of the smell in case there is a gas leak. Similarly, the smell of smoke can alert people about a fire.

Odors are important methods of communication in some animals. They use odor to determine whether others are mates or enemies, to identify individuals, to distinguish between males and females, and to detect whether they are in estrus.

"As soon as I taste a madeleine dipped in tea, it recalls my childhood of long ago" is a famous quote from Proust's *In Search of Lost Time*. It often happens that an odor triggers a vivid memory of a distant event or situation in the past that was sad or pleasant. Odors can also make us feel nostalgic and happy by accessing our deeper emotions. Indeed, odors have an extraordinary ability to evoke memorable episodes, learned experiences, and sometimes the far distant past (Chu, 2000; Larsson et al., 2014; Zucco et al., 2012).

Thus, "What is odor for living things?" is an attractive question, but it is difficult to answer clearly because it has various aspects. Moreover, since there are hundreds of thousands of different odor-molecules, how the brain perceives odors and processes them as information remains a mystery (Mori, 2010).

1.2. What are odorant molecules?

Plants, animals, and many other things in the outside world emit a variety of different volatile molecules (very small invisible molecules that floats in the air). However, these volatile molecules are not always odor molecules. Only molecules that are received by the receptors (proteins that directly receive odor molecules and act as sensors) of the olfactory sensory neurons lining the interior of our nose, translated into signals, and sent to the brain are identified as odor molecules. For example, human olfactory sensory neurons do not have receptors for carbon dioxide (CO_2); therefore, CO_2 is not an odor molecule for humans. However, some animals, including mice, do have receptors for CO_2, and for these animals, CO_2 is an odor molecule. In other words, the nature of whether a volatile molecule is an odor molecule is determined by the nature of the olfactory nervous system in humans and animals, rather than by the physicochemical properties of the molecule. Therefore, if we aim to elucidate the mystery of what makes a “molecule” odor, the best way will be to study the olfactory nervous system in the human and animal brain.

1.3. Olfactory neural processing in the olfactory epithelium

Odorant receptors → olfactory sensory neurons in the olfactory epithelium

When the nose sniffs a cup of tea, the odor molecules from the tea are inhaled into the nose through the external nostrils along with the air and reach the olfactory epithelium inside of the nasal cavity (**Figure 1-1A**). The olfactory epithelium is packed with millions of olfactory sensory neurons (OSNs), and when the sniffed odor molecules reach them, they generate electrical signals that are transmitted to the olfactory bulb (OB) at the bottom of the brain.

The OSNs extend numerous cilia from the tips of their protrusions, and the surface membrane of these cilia is equipped with odorant receptors (ORs) (**Figure 1-1A**). The first researchers to discover ORs were Linda Buck and Richard Axel (Buck and Axel, 1991), who were awarded the 2004 Nobel Prize in Physiology or Medicine for their work. ORs are members of a family of proteins called the "seven transmembrane receptor family," which consists of seven transmembrane regions surrounded by a keyhole structure. When a single odor molecule gets caught in the keyhole-like structure of the OR, the structure of the OR changes slightly, and the signal is transmitted to the G-protein (called "Golf" because it is a G-protein of the olfactory system) that connects to the intracellular site of the OR, activating Golf (**Figure 1-1B**). The activated the Golf induces the activation of an enzyme called adenylate cyclase, which is in the surface membrane of the cilia. When adenylate cyclase is activated, it produces a series of molecules called cyclic AMP (cAMP) and increases the concentration of cAMP in the OSN. When the concentration of cAMP increase in the OSN, cAMP combines with cAMP-dependent ion channels in the surface membrane of the cilia, opening holes for the ions (Na^+ and Ca^{2+}) in these channels. When this channel is opened, the ions enter the membrane, and the membrane potential changes to the positive side. In this way, when odor molecules attach to ORs, the membrane potential of the OSN expressing the receptor changes in the positive direction. The signal from the odor molecule is converted into an electrical signal in the OSN, and this series of processes is the odor signal conversion mechanism in the OSN.

The OSN has a single axon that extends to the OB at the base of the brain, where it makes synaptic contacts with OB neurons. When the membrane potential change in the positive direction caused by the odor molecule is large enough, the OSN produces an action potential through the axon and transmits it to the OB.

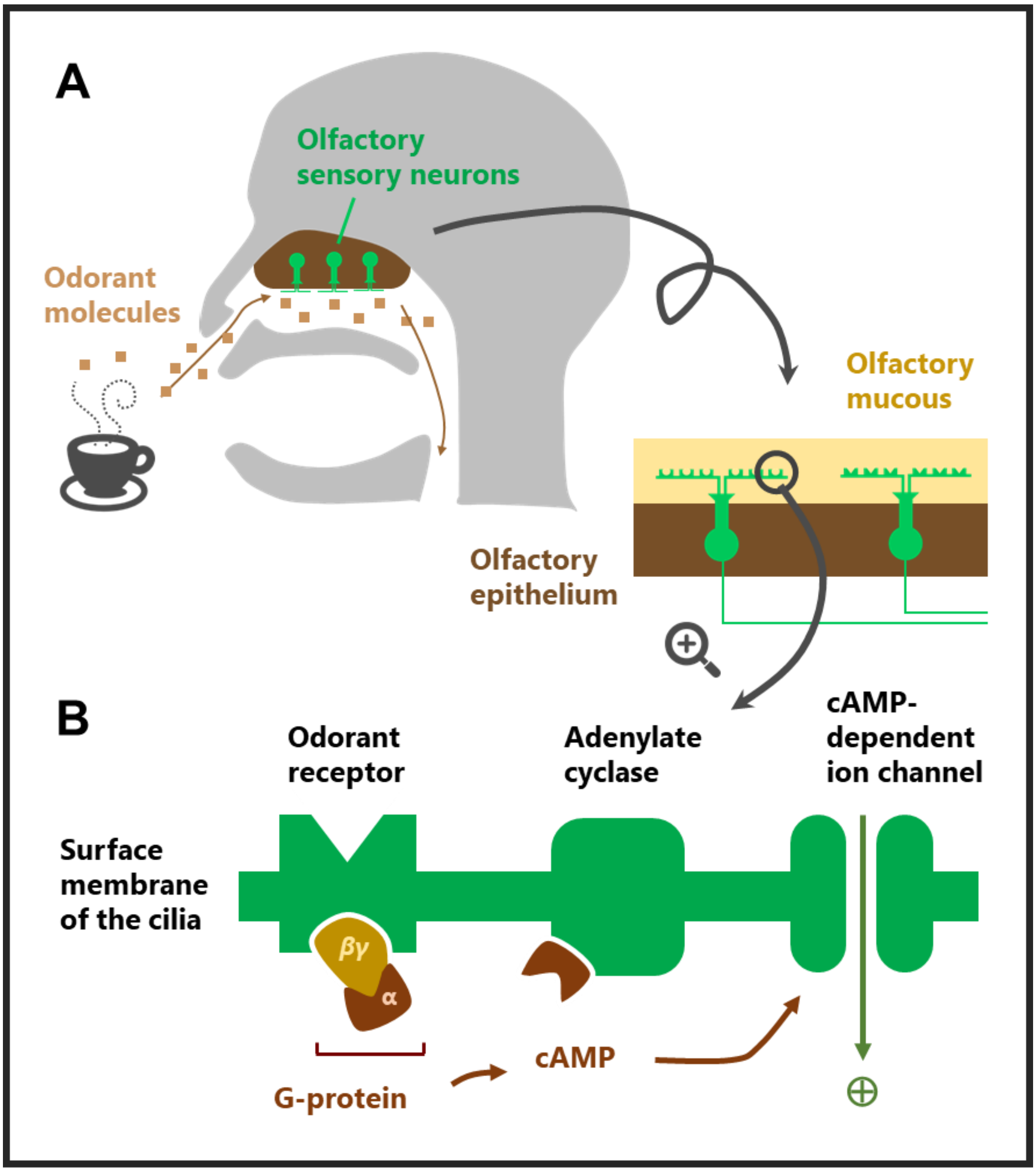

Figure 1-1 | Olfactory neural processing: Odorant receptors → olfactory sensory neurons in the olfactory epithelium

(**A**) Structure and organization of the olfactory epithelium.

(**B**) Odor signal conversion mechanism in the olfactory sensory neuron. The signal from the odor molecule is converted into an electrical signal in the olfactory sensory neuron via G-protein, cAMP, and cAMP-dependent ion channels.

One olfactory sensory neuron–one odorant receptor rule

After the discovery of ORs, the remarkably simple “one OSN–one OR rule” was found: one OSN selects only one type of receptor out of a repertoire of 390 ORs and uses it on the membrane surface of its cilia to equip itself. The many ORs that one OSN is equipped with are all the same type of ORs. Due to this mechanism, to know the combination of ORs activated by an odor molecule, the brain only needs to know the combination of the types of OSNs that are emitting electrical signals. The “one OSN–one OR rule” links the logic of odor molecule identification at the molecular level, in relation to the combination of odor molecules and types of ORs, to the logic of odor molecule identification at the cellular level, in relation to the combination of odor molecules and types of OSNs that emit signals.

1.4. Olfactory neural processing in the olfactory bulb

Olfactory sensory neurons → glomerulus in the olfactory bulb

The axon of the OSN passes through the depth of the olfactory epithelium, enters the skull through a hole called the ethmoid bone, reaches the OB at the base of the brain, and extends into one of the thousands of glomeruli that line the surface of the OB (**Figure 1-2**). The axon is not branched between the OSN and the glomerulus, but once inside the glomerulus, it makes numerous branches and excitatory synapses on the dendrites of principal OB neurons (named mitral cells and tufted cells). When the action potential is transmitted in the axon and reaches the site of the synapse in the glomerulus, the neurotransmitter (glutamate) is released from the end of the axon. When this glutamate is combined with the glutamate receptors on the dendrites of the principal OB neurons, electrical signals are emitted from them. Thus, the electrical signals generated by a single OSN are sent through the axon to only one specific glomerulus. In other words, the glomerulus of the OB is the input terminal for signals from the OSN, and each of the left and right pairs of OBs is equipped with thousands of input terminals. In mice, there are a thousand different OSNs corresponding to approximately a thousand different ORs, and the total number of OSNs is several million. A single glomerulus collects axons from thousands of OSNs.

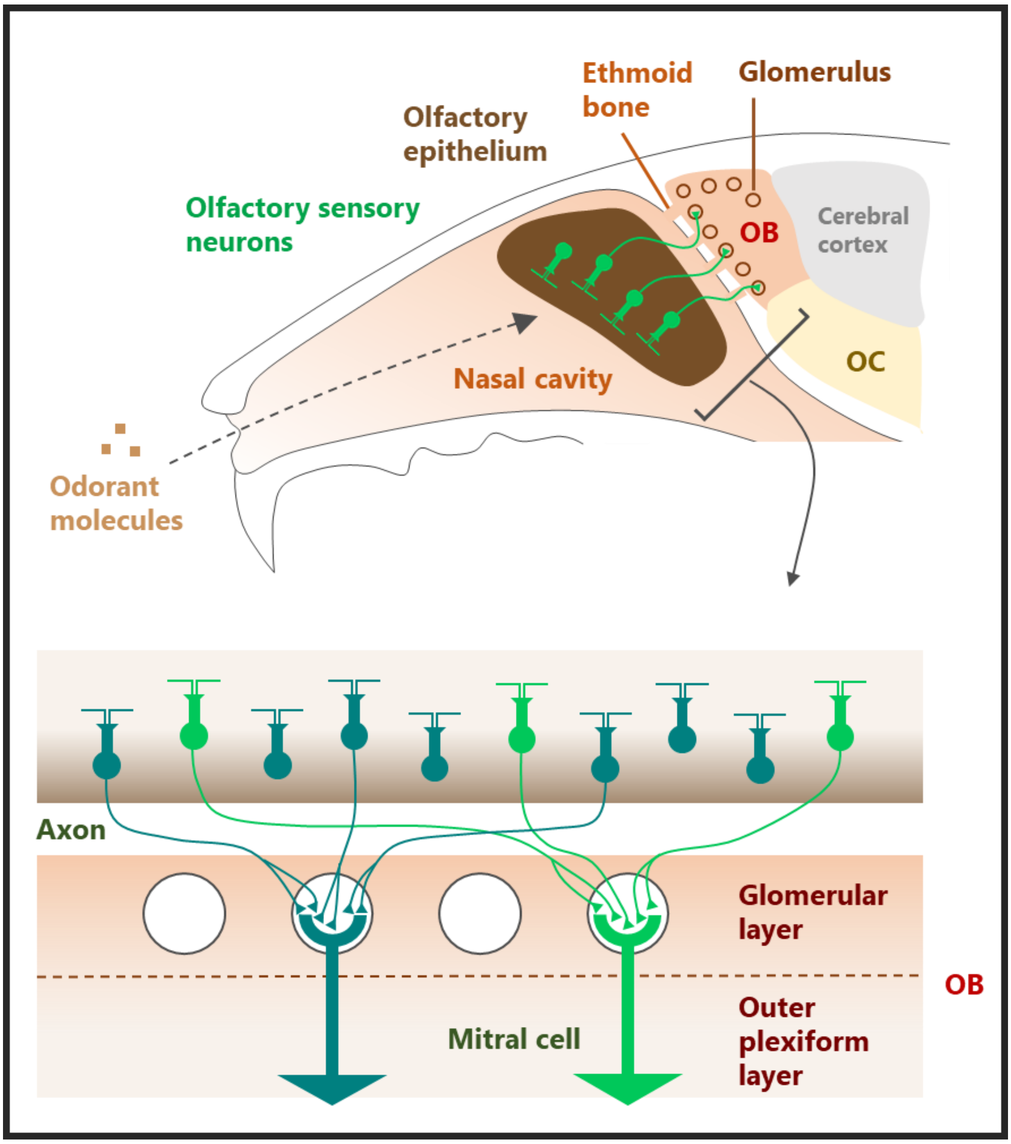

Figure 1-2 | Olfactory neural processing: Olfactory sensory neurons in the olfactory epithelium → olfactory bulb neurons

The axon of the olfactory sensory neurons passes through the depth of the olfactory epithelium, enters the skull through a hole called the ethmoid bone, reaches the OB at the base of the brain, and extends into one of the thousands of glomeruli that line the surface of the OB. It makes numerous branches and excitatory synapses on the dendrites of principal OB neurons (named mitral cells and tufted cells).

One glomerulus–one odorant receptor rule

The “one glomerulus–one OR rule”, which means that thousands of axons assembled in a single glomerulus come from a group of OSNs all expressing the same OR, was revealed. As a result, to know what odor molecule has just been inhaled into the nose, the brain needs to know the combination of activated ORs, i.e., the combination of the types of OSNs emitting electrical signals, as well as the combination of activated glomeruli. As the “one OSN–one OR rule” links the molecular level odor molecule identification mechanism to the cellular level odor molecule identification mechanism, the “one glomerulus–one OR rule” links the molecular and cellular level odor molecule identification mechanisms to the glomerular neural circuit level odor molecule identification mechanism.

Whether a single odor molecule or a complex mixture of different odor molecules, such as the smell of tea, is inhaled into the nose, the corresponding combination of glomeruli is activated in the OB. That is, whether it is a single odor molecule or a mixture of many odor molecules, the odor is encoded in the OB as a combination of activated glomeruli. This spatial distribution of thousands of glomeruli on the OB surface will create the “odor-molecule map”.

Odor-molecule map in the olfactory bulb

In mammals, there are a pair of OBs on each side. How is the “odor-molecule map” of each OB organized? One OB has two maps arranged in almost mirror-like positions (**Figure 1-3**). One is the lateral map, which is in the antero-lateral part of the OB and receives axonal input from a group of OSNs in the antero-lateral part of the olfactory epithelium. The other is the medial map, which is in the posterior medial part of the OB and receives input from the OSNs in the posterior medial part of the olfactory epithelium. The interior of each of the lateral and medial maps is divided into regions called zones and domains. For example, the lateral map is divided into a dorsal zone (D zone) and a ventral zone (V zone). The dorsal zone is further divided into class I domains and class II domains.

It was found that (1) each glomerulus responds to a group of odor molecules with a similar molecular structure, (2) the range of odor molecules to which each glomerulus responds differs between glomeruli, and (3) groups of glomeruli with a similar range of odor molecules cluster together to form “glomerulus clusters” (Igarashi et al., 2012; Mori and Sakano, 2011). Furthermore, the glomerular clusters were arranged in a certain position in the odorant receptor map. Specifically, the OB domain (dorsal zone class I domain) contains glomeruli that respond to odor molecules in the homologous linear fatty acid series, forming a “fatty acid response cluster” (cluster A). Since fatty acids are produced in large quantities when food is decomposed by bacteria, it is assumed that Cluster A is a cluster of glomeruli that responds to decomposing odors and has developed to detect food decomposition. Interestingly, most of the glomeruli in cluster A respond to both odors.

In front and outside of cluster A, glomeruli that respond to odor molecules with structures such as fresh-smelling straight-chain alcohols, anethole, and straight-chain ketones gather to form cluster B. These cluster B-activating odor molecules have a common fresh alcohol-like, anise-like, or fruit-like odor. A little behind cluster B is cluster C, which responds to phenolic odor molecules with a chemical odor like phenol and cresol. In addition, behind cluster C is cluster D, which responds to linear ketones, ketones with cyclic structures, and diketones. Clusters B, C, and D are aligned in this order in the domain (dorsal zone class II domain) with cluster A at a fixed position in the domain and clusters B, C, and D from anterior to posterior in the domain. This arrangement of clusters is the same in all rats examined. In the V zone outside the OB, glomeruli that respond to petroleum odors such as benzenes and linear hydrocarbons are clustered together to form cluster H. In addition to benzene and linear hydrocarbons, cluster I has also been found to contain glomeruli that respond to terpene hydrocarbons (woody or citrusy odors).

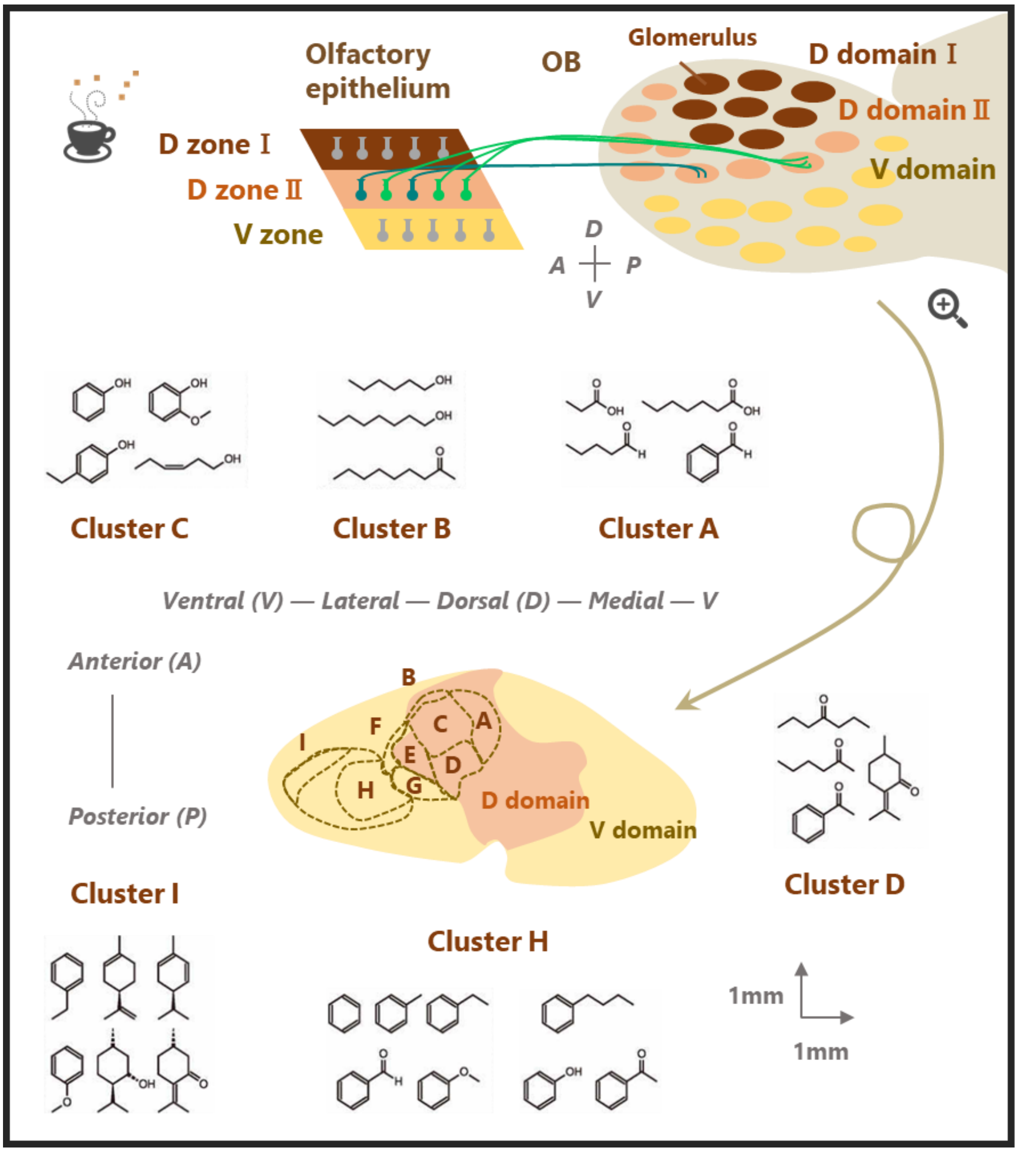

Figure 1-3 | Olfactory neural processing: Odor-molecule map in the olfactory bulb

Upper right diagram: a lateral view of the domain organization of glomeruli in the lateral map of the rodent OB. One OB has lateral and medial maps arranged in almost mirror-like positions. These maps are divided into regions called domains (D-I, D-II, and V). Lower diagram: a dorsal centered view of an unrolled flattened map of glomerular layer of the OB. The glomerular clusters were arranged in a certain position in the odorant receptor map.

Functions associated with the odor-molecular map

Thus, it was found that every rat OB has a certain odor-molecular map in which specific odor response cluster groups are arranged in an orderly fashion at specific positions within the receptor zone or receptor domain. Comparing the rat odor-molecular map with that of the mouse, there is a slight discrepancy in the positions of the odor response clusters, but the relative arrangement of the clusters is the same. What type of function is associated with the well-organized odor-molecular map that is common to many mammals? By observing the behavior of mice lacking the D-zone to odors, it was surprisingly discovered that the innate fear response to the odors of predators such as cats and foxes was eliminated (Kobayakawa et al., 2007). When normal rats and mice smell trimethylthiazoline, which is found in fox feces and is a major component of fox odor, they have a fear response. Researchers investigated how the glomeruli that respond to trimethylthiazoline are distributed in the odor-molecular map of normal mouse OB and found that they clustered together at the back of the domain, but not in the domain. There were also many glomerular clusters that responded to trimethylthiazoline in the V-zone, and they were widely distributed. Based on these experimental results, it can be hypothesized that the receptor zones and receptor domains in the OB odor-molecular map may be related to various behavioral responses induced by odors. For example, when a mouse smell various odor-molecules coming from a cat, both the glomeruli in the V-zone and D-zone are activated in the odor molecular map of the mouse OB, but only the glomeruli in the D-zone may send signals to the brain for a behavioral response called the fear response. The glomeruli in the V zone may be associated with a different behavioral response. Thus, there may be a functional difference in the odor molecular map of OB by region. This understanding may provide the first important insight into the brain neural mechanisms that link various odor information to appropriate behavioral responses. If each region in the odor-molecular map can determine what odor information it receives and what groups of behavioral and emotional responses it is associated with, and then determine where the OB neurons within each region send axons to contact higher olfactory centers, it could be possible to develop a new method of understanding the neural mechanisms that are still largely unknown.

Glomerular module containing mitral and tufted cells

Mitral cells and tufted cells usually extend from one main dendrite to a single glomerulus and receive excitatory synaptic input from OSN axons only within that glomerulus. That is, just as each OSN communicates with one glomerulus, each mitral or tufted cell belongs to one glomerulus. Each glomerulus contains approximately 10 to 20 mitral cells and approximately 50 tufted cells. The thousands of OSNs, their axons, and the dendrites and axons of dozens of mitral and tufted cells belonging to a single glomerulus are collectively called the “glomerular module”. Since a single glomerulus represents one type of OR, the cells in a glomerular module are responsible for the information of the same type of OR. In other words, a group of OSNs in each glomerular module collects information from one type of Ors from a large part of the olfactory epithelium and sends it to that glomerulus, while mitral and tufted cells that receive excitatory synaptic input from OSNs in that glomerulus send information from their receptors to the olfactory cortex (OC). Each glomerular module creates an “odor molecule receptor information channel” that is responsible for the information of a specific OR.

OB neurons, which receive excitatory synaptic input from OSNs axons in the glomerulus and project their axons to the OC, are classified into two types: large cells named “mitral cells” because their cell bodies resemble the hats worn by European monks, and smaller cells named “tufted cells” because the fine branching of dendrites in the glomerulus resembles the ornamentation of a tuft. The cell bodies of mitral cells are arranged in the mitral cell layer, while the cell bodies of tufted cells are distributed in the outer plexiform layer. Since both mitral and tufted cells extend their axons to the OC, one glomerular module (odorant molecular receptor information channel) has two neural pathways that send odor information via mitral or tufted cells. Considering that each glomerular module including mitral cells and tufted cells creates an odorant receptor information channel, the entire OB is a map of odorant receptor information channels.

1.5. Olfactory neural processing in the olfactory cortex

Olfactory bulb neurons → olfactory cortex subareas

Information about the odor sniffed in the nose is encoded in a separate and distinct glomerular module in the OB odor molecular map. To recognize the smell of tea, the information from the many glomerular modules activated by the odor molecules in the "odor-molecular profile" of tea must be further integrated and read out by the OC. Since mitral cells and tufted cells in the OB project axons to the OC and make excitatory synaptic contacts on the dendrites of OC neurons, it is considered that each neuron in the OC integrates information from many "odor-molecular receptor information channels". The mechanism of integration of odor information may be hidden in the connection between OB and OC. However, it is still unclear how the axons of mitral and tufted cells connect to OC neurons, and how these rules relate to the recognition of odors associated with targets.

The OC is a collection of many subareas where the axons of mitral and tufted cells of the OB project. **Figure 1-4** shows a view of the rat brain from the bottom, where the colored areas indicate the OC. The axons of mitral cells and tufted cells branch out in the most superficial layer of these OCs (layer Ia) and make excitatory synapses on the dendrites of OC neurons in this layer. In rats and mice, the OC is spread out so widely that it occupies most of the basal part of the brain, with the anterior olfactory nucleus, anterior piriform cortex, tenia tecta, olfactory tubercles, nucleus of the lateral olfactory tract, amygdaloid cortex, posterior piriform cortex, and entorhinal cortex arranged from anterior to posterior. Most of these OC areas are organized into three layers, namely layer Ⅰ, layer Ⅱ, and layer Ⅲ from the surface, while the entorhinal cortex consists of six layers. Each OC has its own complex neural circuitry, and an OC neuron has excitatory synaptic contacts with many neurons in the same or other OC areas via its axonal lateral branches. However, it is still not well understood how the OC function. Perhaps each area reads the OB odor map differently and has its own olfactory information processing mechanism. Understanding this is a major challenge for olfactory researchers at present. The olfactory nervous system also could recognize if the food we are smelling is the same as something we have eaten before. Neural circuits in the anterior and posterior piriform cortices are expected to play an important role in the process of remembering and recognizing food odor information (Manabe et al., 2011).

Unique inputs and outputs of olfactory cortex subareas

It remains unknown as to how each area of the OC encodes for sensory- and behavior-related information from higher-order regions. This is because most of the OC areas are very small and difficult to access in the deep part. In addition, since previous olfactory researchers have only observed odor responses about OC, there has been no research to investigate the processing of higher-order information such as task variables during behavioral tasks. Indeed, the importance of motor and behavioral state information observed in the whole brain has recently been reported (Musall et al., 2019; Parker et al., 2020; Steinmetz et al., 2019; Stringer et al., 2019). In this thesis, I focused on the OC subareas: aPCx, vTT, NLOT, and ACo (**Figures 1-5 and 1-6**).

The piriform cortex is the largest of the olfactory cortical regions. The aPCx (**Chapter 3**) has strong reciprocal connections with the OB (Ghosh et al., 2011; Igarashi et al., 2012; Luskin and Price, 1983a; Miyamichi et al., 2011; Mori and Sakano, 2011; Nagayama, 2010; Sosulski et al., 2011). On the other hand, the piriform cortex also receives substantial top-down projections originated in higher order regions and projects to the frontal cortex, amygdala, thalamus, and many OC subareas (Mori, 2010). The vTT (**Chapter 4**) has reciprocal connections with the OB, aPCx, and pPCx (Igarashi et al., 2012; Luskin and Price, 1983a, 1983b). In addition, the deep layers of the vTT receive top-down projections from the medial prefrontal cortex (Hoover and Vertes, 2011). The NLOT (**Chapter 5**) receives direct projections from the OB and piriform cortex (Luskin and Price, 1983a; Price, 1973) and, along with the anterior amygdaloid area, anterior cortical and posterolateral cortical amygdaloid nuclei, and amygdalo-piriform transition area, forms part of the olfactory amygdala (Santiago and Shammah-Lagnado, 2004). The NLOT strongly innervates the basolateral amygdala and ventral striatum (Luskin and Price, 1983a; Price, 1973; Santiago and Shammah-Lagnado, 2004). The ACo (**Chapter 6**) receives dense projections from the OB, moderate projections from the piriform cortex, lateral entorhinal cortex, basomedial amygdaloid nucleus, and medial amygdaloid nucleus, and scarce projections from the ventral tegmental area and the tenia tecta (Cádiz-Moretti et al., 2017). The ACo projects densely to basomedial amygdaloid nucleus (Cádiz-Moretti et al., 2017). Thus, each area has unique input and output properties.

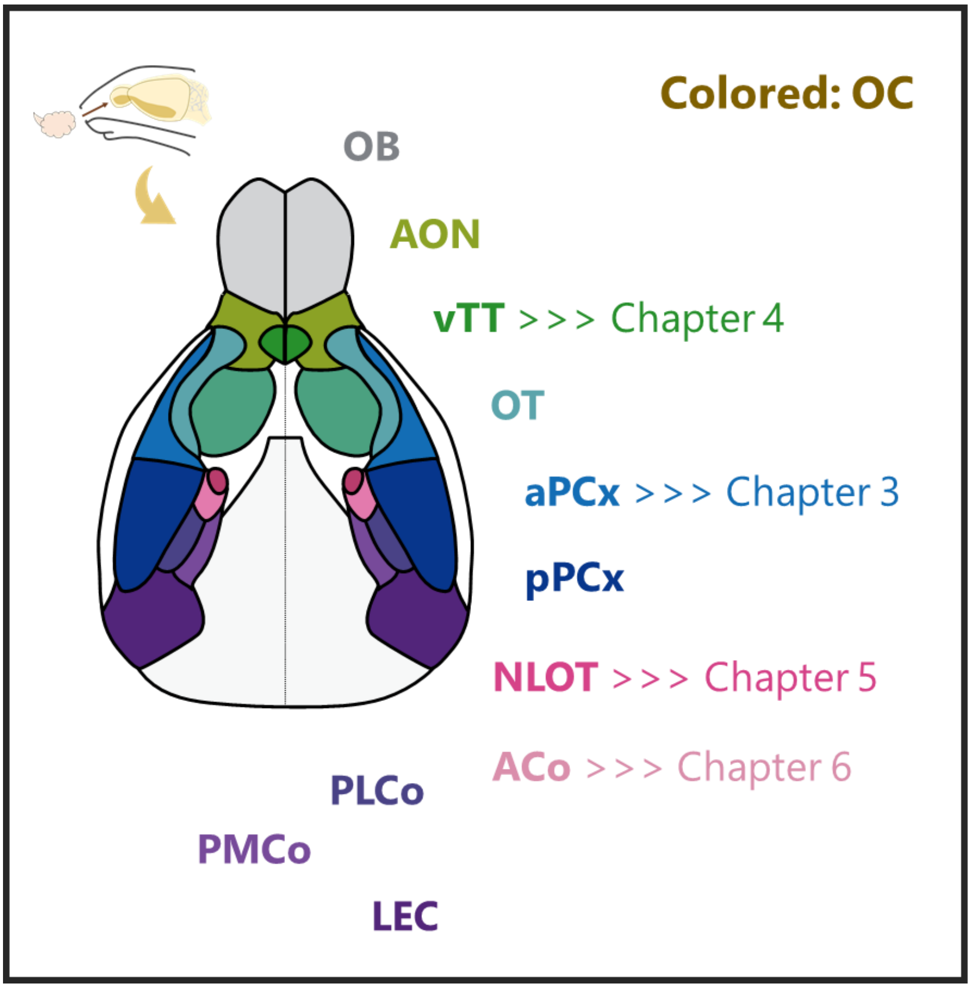

Figure 1-4 | Olfactory neural processing: Olfactory bulb neurons → olfactory cortex subareas

Upper left diagram shows a rat brain, and the olfactory area (OB and OC) is shown by the brown shaded area. Center diagram shows a olfactory area a view of the rat brain from the bottom, where the colored areas indicate the OC. Abbreviations: **ACo**, anterior cortical amygdaloid nucleus; **AON**, anterior olfactory nucleus; **aPCx**, anterior piriform cortex; **LEC**, lateral entorhinal cortex; **NLOT**, nucleus of lateral olfactory tract; **OT**, olfactory tubercle; **PLCo**, postero-lateral cortical amygdaloid nucleus; **PMCo**, postero-medial cortical amygdaloid nucleus; **pPCx**, posterior piriform cortex; **vTT**, ventral tenia tecta.

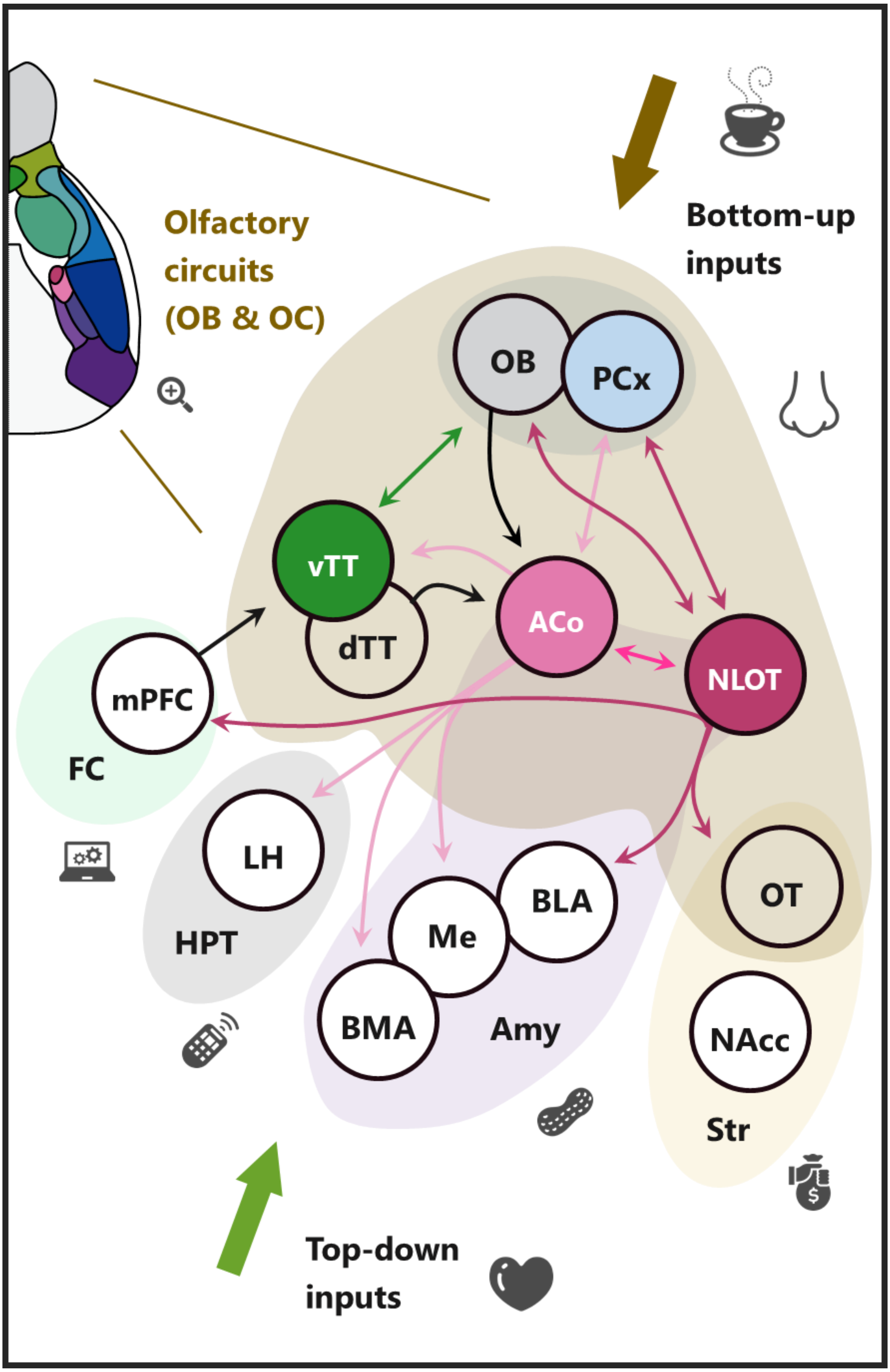
Olfactory
circuits
(OB & OC)
Bottom-up
inputs
OB
PCx
vTT
dTT
ACo
NLOT
mPFC
FC
LH
HPT
OT
BLA
Me
BMA
Amy
NAcc
Str
Top-down
inputs

Figure 1-5 | Schematic representation of the pattern of inputs and outputs of the olfactory cortex subareas described in the previous work, focusing on vTT, NLOT, and ACo.

The olfactory circuits (OB and OC) are shown by the brown shaded area. The aPCx has strong reciprocal connections with the OB and receives substantial top-down projections originated in higher order regions. It projects to the frontal cortex, amygdala, thalamus, and many OC subareas. The vTT has reciprocal connections with the OB and piriform cortex (**PCx**). The deep layers of the vTT receive top-down inputs from the medial prefrontal cortex (**mPFC**). The NLOT receives direct projections from the OB and PCx. The NLOT strongly innervates the basolateral amygdala (**BLA**) and ventral striatum. The ACo receives dense projections from the OB, moderate projections from the PCx, lateral entorhinal cortex, basomedial amygdaloid nucleus (**BMA**), and medial amygdaloid nucleus (**Me**), and scarce projections from the ventral tegmental area and the tenia tecta. The ACo projects densely to BMA. Thus, each area has unique input and output properties. Other abbreviations: **OT**, olfactory tubercle; **dTT**, dorsal tenia tecta; **FC**, frontal cortex; **HPT**, hypothalamus; **LH**, lateral hypothalamus; **Amy**, amygdala; **Str**, striatum; **NAcc**, nucleus accumbens.

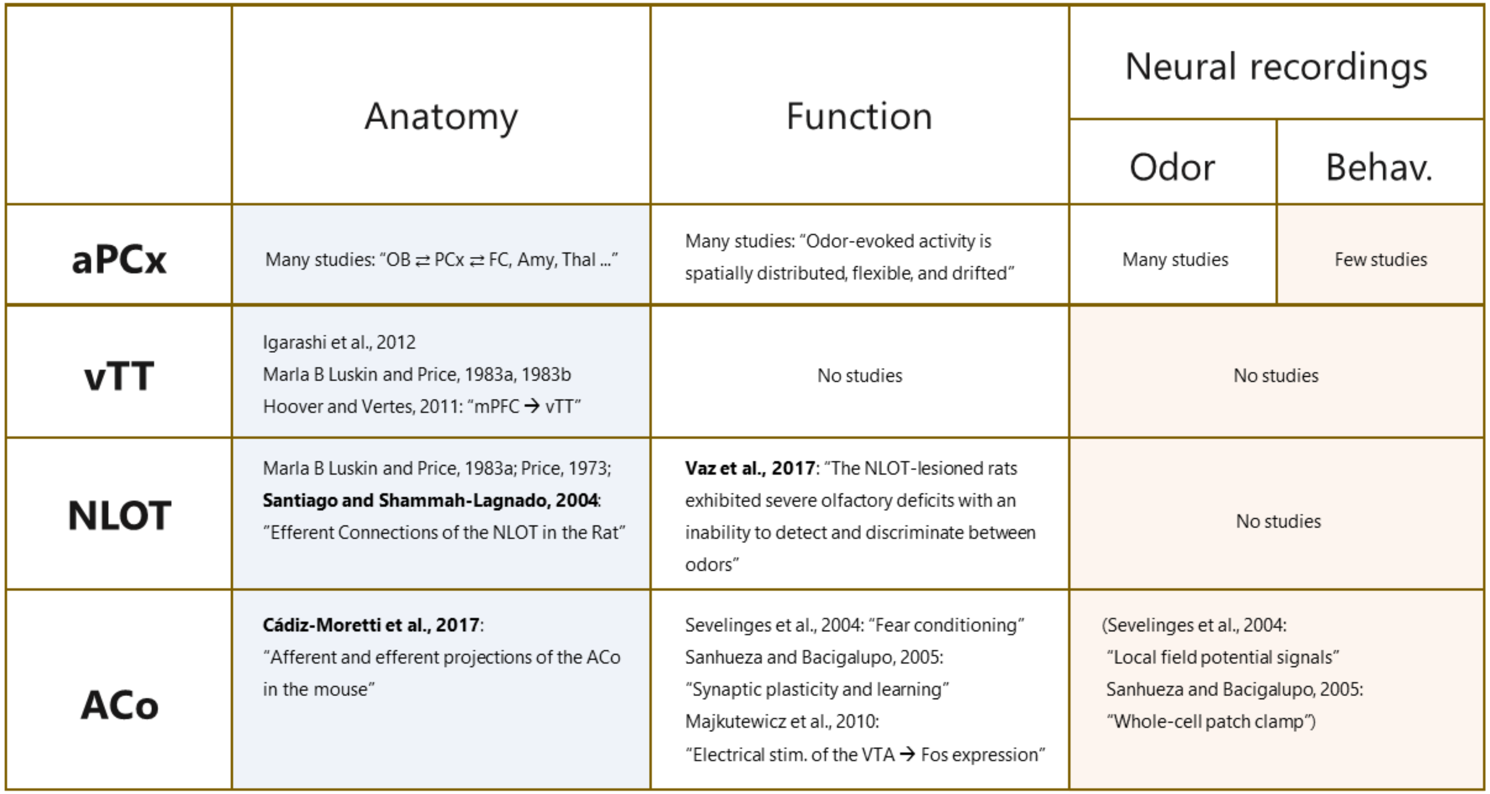

	Anatomy	Function	Neural recordings	
			Odor	Behav.
aPCx	Many studies: "OB ⇄ PCx ⇄ FC, Amy, Thal ..."	Many studies: "Odor-evoked activity is spatially distributed, flexible, and drifted"	Many studies	Few studies
vTT	Igarashi et al., 2012 Marla B Luskin and Price, 1983a, 1983b Hoover and Vertes, 2011: "mPFC → vTT"	No studies	No studies	
NLOT	Marla B Luskin and Price, 1983a; Price, 1973; **Santiago and Shammah-Lagnado, 2004**: "Efferent Connections of the NLOT in the Rat"	**Vaz et al., 2017**: "The NLOT-lesioned rats exhibited severe olfactory deficits with an inability to detect and discriminate between odors"	No studies	
ACo	**Cádiz-Moretti et al., 2017**: "Afferent and efferent projections of the ACo in the mouse"	Sevelinges et al., 2004: "Fear conditioning" Sanhueza and Bacigalupo, 2005: "Synaptic plasticity and learning" Majkutewicz et al., 2010: "Electrical stim. of the VTA → Fos expression"	(Sevelinges et al., 2004: "Local field potential signals" Sanhueza and Bacigalupo, 2005: "Whole-cell patch clamp")	

Figure 1-6 | The previous accumulation of knowledge about anatomy, function, and neural recordings in the aPCx, vTT, NLOT, and ACo

Well-researched fields are shown by the blue shaded area and poorly ones are shown by the red shaded area. In this thesis, I focused on the neural responses to odor-sampling and behavioral epochs of four OC subareas (aPCx, vTT, NLOT, and ACo) during odor-guided behavioral tasks.

1.6. Olfactory neural processing as links to higher functions

Orbitofrontal cortex circuits integrate sensory inputs to evaluate the food

The OC, where the axons of the mitral and tufted cells of the OB project, is an evolutionarily old region of the cerebral cortex. In the neocortex, which is evolutionarily new, where is the olfactory information sent? In 1975, it was reported that neurons receiving odor information were clustered in the lateral posterior part of the orbitofrontal cortex (OFC) in the monkey neocortex (Tanabe et al., 1975). In 1980, a group of neurons receiving olfactory information was discovered in the central part of the OFC (Yarita et al., 1980). In addition, it was found that these cells receive olfactory information from the OC via the dorsomedial nucleus of the thalamus. These studies showed that a large amount of odor information is sent to the OFC in the neocortex. After that, Edmund T. Rolls' group found that neurons in the OFC collect a special combination of taste, smell, temperature, and texture information of food in the mouth (Rolls, 2004, 2000). In other words, the OFC integrates different sensory inputs (smell, taste, and somatosensory). In addition, when the subjects were satiated with a food item, the response of OFC neurons to the sensory input of that food was reduced, while the response to the sensory input of another food was not (O'Doherty et al., 2000). Human brain imaging studies have also reported that OFC activity correlates with subjective ratings of the pleasantness of food tastes and smells. This suggests that the OFC and the neural pathways that communicate with it integrate different sensory inputs to evaluate the food in the mouth. The OFC may play a major role in perceiving the food being chewed in the mouth as tasty and in directing the food to the esophagus.

Olfactory tubercle circuits in the olfactory cortex link odors to motivational states

Various odors induce various behavioral responses and emotional behaviors in rodents. When they detect the odor of food, they move toward the odor to find and eat the food based on the odor. The rodents' brains predict the reward of food based on the odor information and induce the motivational state of appetite. When they detect the odor of a natural enemy such as a cat or fox, they exhibit escape behaviors and fear responses. In this case, rodents' brains predict the approaching cat or fox and induce motivational states such as alarm and fear. The odor of a rival male, which is not a mate, may induce a fight motivation in the brain of rodent. Part of the neural mechanism that links various odor inputs to different motivational states may be hidden in the neural communication from the odor map in the OB to the olfactory tubercle (OT) in the OC. The OT together with the nucleus accumbens forms a structure called the ventral striatum. The output information of OT neurons is transmitted via neurons in the ventral pallidum to dopaminergic neurons in the midbrain, which contain the neurotransmitter dopamine. The neural pathway from OB - OT - ventral globus pallidus - midbrain dopaminergic neurons is assumed to be closely related to the prediction of food and reward by odor. Not only the OT, but also various other areas of the OC may have their own function maps of motivation and emotional behavior induced by odors.

Conversion of the odor processing mode depending on the internal state

Motivation and emotional behaviors induced by odors change significantly depending on the internal states (behavioral and emotional states) of the brains of humans and rodents at the time. For example, when we smell grilled meat in a state of hunger, we feel motivated to eat. However, when we smell grilled meat after eating until we are full, we no longer feel motivated to eat. When we are asleep, the smell of grilled eel does not arouse our appetite. In other words, depending on the internal state of the brain, such as hunger or satiety and wakefulness or sleep, the neural circuits that link odor input to emotional behavior and motivation work in different ways. Interestingly, it has been found that OB neurons are active when odors are inhaled into the nasal cavity during both wakefulness and sleep, while OC neurons respond to odors only during wakefulness and hardly at all during non-REM sleep (Murakami et al., 2005). During wakefulness, olfactory information is sent to the OC and higher centers, but during non-REM sleep, it is sent to the OB, but not to the OC or higher centers. This sleep-induced blocking of sensory information transmission in the central nervous system is also observed in vision as well as auditory and somatosensory perception and is commonly referred to as “sensory gating”. The changes in the mechanisms by which neural circuits work are not only due to changes in sleep and wakefulness. Even when we are awake, the neural circuits of the brain work differently when we are resting than when we are searching for food, and differently when we are eating. Such a change in the information processing mode of the neural circuits depending on the behavioral state is not seen in artificial machines such as computers and is a major characteristic of the brain. In addition to changes in behavioral states, changes in emotional states probably have a significant impact on changes in the information processing mode of neural circuits. Research on the mechanism of conversion of the olfactory information processing mode of the olfactory nervous system depending on the emotional state, which is expected to progress in the future, may provide important clues for studying the relationship between changes in the emotional state and changes in the sensory information.

Closing remarks for future olfactory research

Research on the olfactory nervous system has progressed from studies on odor molecular receptors and the odor molecular map of the OB to studies on the relationship between various regions of the odor map and emotional and motivational behaviors induced by odors. However, research on olfactory neural circuits to understand the brain’s neural mechanisms that make us take appropriate emotional and motivational actions in response to sensory information from the outside world has just started. Since olfaction is closely linked to emotion and motivation, research using olfactory cues is expected to make an important contribution by paving the way for the understanding of neural mechanisms for emotion and motivation.

Chapter 2. Material and Methods

2.1. Animals

All the experiments were performed on Long-Evans rats (11~ weeks old; weighing 250-350 g) and male C57BL/6 mice (9~ weeks old; weighing 20–25 g), purchased from Shimizu Laboratory Supplies Co., Ltd., Kyoto, Japan. The animals were individually housed in a temperature-controlled environment with a 13-hr light/11-hr h dark cycle (lights on at 8:00 and off at 21:00). They were provided with water after the training and recording sessions to ensure that the body weights dipped no lower than 85% of the initial levels, and food was supplied ad libitum. All experiments were performed in accordance with the guidelines for animal experiments at Doshisha University and with the approval of the Doshisha University Animal Research Committee.

2.2. Apparatus

We used a behavioral apparatus controlled by the Bpod State Machine r0.5 (Sanworks LLC, NY), an open-source control device designed for behavioral tasks. The apparatus comprised a custom-designed mouse behavior box with two nose-poke ports on the front wall. The box was contained in another soundproof box (BrainScience Idea. Co., Ltd., Osaka, Japan) equipped with a ventilator fan that provided adequate air circulation and low-level background noise. Each of the two nose-poke ports had a white light-emitting diode (LED) and infrared photodiode. Interruption of the infrared beam generated a transistor-transistor-logic (TTL) pulse; thus, signaling the entry of the mouse head into the port. The odor delivery port was equipped with stainless steel tubing connected to a custom-made olfactometer. In the rat experiment, almond, banana, coffee, lemon, orange, rose, tea, vanilla flavors (Narizuka Co., Ltd., Tokyo, Japan), +limonene, acetophenone, anisole, ethyl butyrate, ethyl hexanoate, eugenol, isoamyl acetate, and m-Cresol (Tokyo Chemical Industry Co., Ltd., Tokyo, Japan) were used as the go/no-go cue odors. In the mouse experiment, eugenol was used as the go-cue odor and amyl acetate as the no-go-cue odor (Tokyo Chemical Industry Co., Ltd., Tokyo, Japan). These odors were diluted to 1:9 by airflow. Water-reward delivery was based on gravitational flow, controlled by a solenoid valve (The Lee Company, CT), and connected via Tygon tubing to the stainless-steel tubing. The reward amount was determined by the opening duration of the solenoid valve and was regularly calibrated.

2.3. Behavioral task: Four odors-guided go/no-go task with rats (Chapter 3)

Rats were trained and tested on an odor-guided go/no-go task in which the recognition of two odors as reward-predicting go-cues (go cue odor-1 and -2) and other two odors as no-reward-predicting no-go-cues (no-go cue odor-1 and -2). Each trial started by the illumination of the LED light at the right odor deliver port, which instructed the rat to nose poke into the odor deliver port. A nose poke in the odor deliver port resulted in the delay and delivery of one of the four cue odors, selected pseudo-randomly, for 500 ms. To decorrelate the timing of port entry and the delivery of odor, opening of the odor valve was delayed following entry into the odor deliver port by 200–500 ms (uniformly distributed). The rat was required to sniff the odor and then keep nose poking during the odor stimulation. If the odor port withdrawal occurred less than the odor deliver delay after odor onset, the rat was required to nose poke into the odor deliver port again. After the odor stimulation, the LED light at the right odor deliver port was turned off, the LED light at the left reward deliver port was turned on, and the rat could withdraw its nose from the odor deliver port. When a go-cue odor was presented at the odor deliver port, the rat was required to move to and nose poke into the left reward deliver port within 2 s. At the reward deliver port, the rat was required to keep nose poking for 500 ms before reward delivery began. Then 80 μl of 5% sucrose water or 40 μl of water was delivered as reward. If a no-go-cue odor was presented, the rat was prohibited from poking its head into the reward deliver port for 2 s after the offset of odor stimulation. An incorrect port entry, or an absence of a port entry, resulted in 10 s interval as punishment with alarm sound. Inter-trial interval was 2 s each trial. Once every 10 trials, we introduced catch trials in which the airstream was delivered through a filter containing no odorants during which, the rats were not rewarded regardless of their choice (go or no-go behavior). During the training sessions, the rats learned to obtain water rewards at the left water port, move from the right odor port to the left odor port, and associate odor cues with the correct action.

2.4. Behavioral task: Two odors-guided go/no-go task with mice (Chapter 4-6)

After a 3 s inter-trial interval, each trial began by illuminating the LED light at the right odor port, which instructed the mouse to poke its nose into that port. A nose-poke into the odor port resulted in the delivery of one of the cue odors for 500 ms. The mice were required to maintain their nose-poke during odor stimulation to sniff the odor. After odor stimulation, the LED light was turned off and the mice could withdraw their noses from the odor ports. If a go-cue odor was presented, the mice were required to move to and nose-poke into the left water reward port within a timeout period of 2 s. At the water port, the mice were required to maintain their nose-poke for 300 ms before water delivery began. Next, 6 μL of water was delivered as a reward. If a no-go-cue odor was presented, the mice were required to avoid entering the water port for 2 s following odor stimulation. Once every 10 trials, we introduced catch trials in which the airstream was delivered through a filter containing no odorants during which, the mice were not rewarded regardless of their choice (go or no-go behavior). During the training sessions, the mice learned to obtain water rewards at the left water port, move from the right odor port to the left odor port, and associate odor cues with the correct action. The accuracy rate was calculated as the total percentage of successes in the go and no-go trials in a session.

To test the time lag between the start of odor stimulation and the arrival of the odor molecules to the mouse's nose, we conducted additional experiments in which odor presentation durations were 100, 200, 300, and 500 ms, without keeping the mice's nose inserted into the odor port during the odor presentation in each session (14, 6, 11, and 7 sessions in three mice) (**Figure 5-1C**). The odor presentation duration was fixed in each session and reduced from 500 ms to 100 ms across sessions.

2.5. Electrophysiology

The rats were anesthetized with ketamine (67.5 mg/kg, i.p.) and medetomidine (0.5 mg/kg, i.p.), and implanted with a custom-built microdrive of 12 to 14 tetrodes targeted to the left aPCx (2.1 mm anterior to bregma and 3.8 mm lateral to the midline). The mice were anesthetized with medetomidine (0.75 mg/kg i.p.), midazolam (4.0 mg/kg i.p.), and butorphanol (5.0 mg/kg i.p.), and implanted with a custom-built microdrive of four tetrodes in the vTT (2.6 mm anterior to bregma, 0.4 mm lateral to the midline), NLOT (0.1 mm anterior to the bregma, 2.0 mm lateral to the midline), and ACo (0.1 mm anterior to the bregma, 2.2 mm lateral to the midline). Individual tetrodes consisted of four twisted polyimide-coated tungsten wires (California Fine Wire, single wire diameter 12.5 μm, gold plated to <500 kΩ). Two additional screws were threaded into the bone above the cerebellum for reference. The electrodes were connected to an electrode interface board (EIB-18, Neuralynx, MT) on the microdrive. The microdrive array was fixed to the skull using LOCTITE 454 (Henkel Corporation, Düsseldorf, Germany). After the completion of surgery, the rats and mice received atipamezole (0.75 mg/kg i.p.) to reverse the effects of medetomidine and allow for a shorter recovery period. Additionally, the rats and mice received analgesics (ketoprofen, 5 mg/kg, i.p.). Behavioral training resumed at least 1 week postoperatively. Electrical signals were obtained with either a Cheetah recording system (Neuralynx) or open-source hardware (Open Ephys). For unit recordings, the signals were sampled at 32 kHz in NeuraLynx and at 30 kHz in Open Ephys and band-pass filtered at 600–6,000 Hz. After each recording, the tetrodes were adjusted to obtain new units. Their locations during each recording session were estimated based on their depth and later confirmed histologically based on electrolytic lesions and on the visible tetrode tracks.

2.6. Data analyses: Spike sorting

All data analyses were performed using built-in and custom-built software in MATLAB 2019a (The Mathworks, Inc., MA).

The spikes were sorted into clusters offline based on their waveform energy, peak amplitudes, and the first principal components (PC) from the four tetrode channels using an automated spike-separation algorithm KlustaKwik (K.D. Harris) (**Figure 2-1**). The resulting classifications were corrected and refined manually using MClust software (A.D. Redish). The clusters were considered as single units only when the following criteria were met: (1) refractory period (2 ms) violations were <0.2% of all spikes, and (2) the isolation distance, estimated as the distance from the center of the identified cluster to the nearest cluster based on the Mahalanobis distance, was >20.

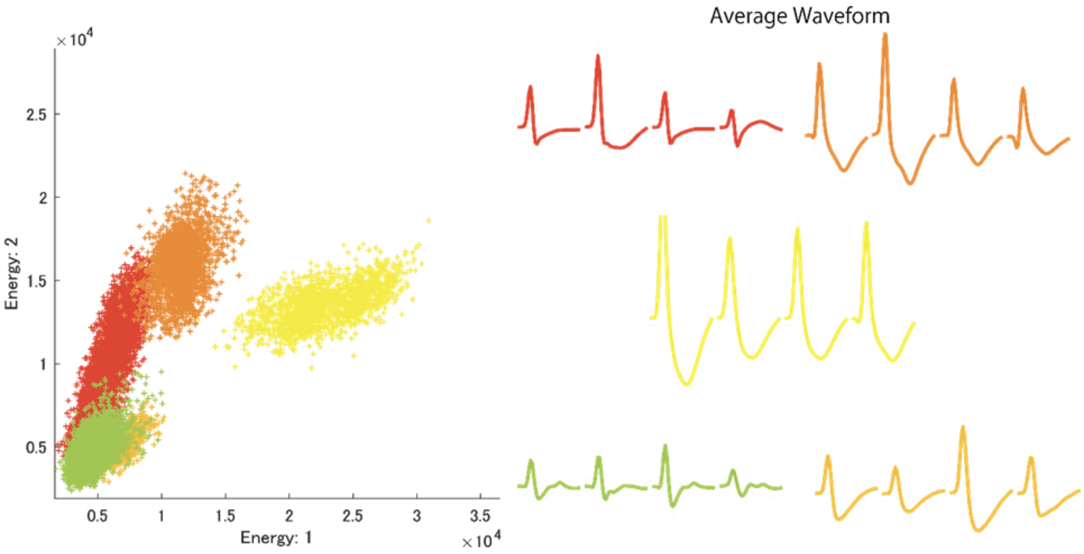

Figure 2-1 | An example of the spike sorting results

The left panel shows five single neurons identified from a tetrode. The x- and y-axes represent energy of spikes detected by ch. 1 and ch. 2, respectively, of the four tetrode chs. Clusters, represented by different colors, indicate different single neurons. The right panel indicates the average spike waveform of the five identified single neurons. The colors correspond to those of the clusters.

2.7. Data analyses: Spike histograms

Neural and behavioral data were synchronized by inputting each event timestamp from the Bpod behavioral control system into the electric signal recording system. To calculate the firing rates during tasks, peri-event time histograms were calculated using a 20 ms bin width and smoothed by convolving spike trains with a 60 ms-wide Gaussian filter. To examine the relationship between the firing rate changes among individual neurons and the development of behavioral epochs in behavioral tasks, we created event-aligned spike histograms (EASHs) (Ito and Doya, 2015). As behavioral epoch durations varied for each trial, the median duration of the epoch was calculated first. The spike timing during each epoch and for each trial was linearly transformed to correspond with the median behavioral duration of each epoch. The number of spikes in each epoch was preserved. In this way, the regular raster plots were transformed into event-aligned raster plots. Consequently, an EASH was calculated using a 20 ms bin width and smoothed by convolving the spike trains with a 60 ms-wide Gaussian filter from the event-aligned raster plots.

2.8. Data analyses: Receiver operating characteristic (ROC) analyses

To quantify the firing rate changes, we used an algorithm based on ROC analyses that calculates the ability of an ideal observer to classify whether a given spike rate was recorded in one of two conditions (e.g., during go-cue or no-go-cue odor presentation) (Felsen and Mainen, 2008). We defined an area under the ROC curve (auROC) equal to 2 (ROC_{area} - 0.5), with the measure ranging from -1 to 1, where -1 signifies the strongest possible value for one alternative and 1 signifies the strongest possible value for the other. The statistical significance of these ROC analyses was determined using a permutation test. For this test, we recalculated the ROC curves after randomly reassigning all firing rates to either of the two groups arbitrarily. This procedure was repeated many times (500~1000 repeats for analyses of dynamics; we shuffled only the trial labels) to obtain a distribution of values. Subsequently, we calculated the fraction of random values exceeding the actual value. For all analyses, we tested for significance at $\alpha = 0.01$. Only neurons (sessions) with a minimum number of three trials for each analyzed condition were included in the analyses.

For analyses of dynamics (width: 100 ms, step: 20 ms), we calculated three measures from the auROC values of correct trials:

(1) Time of center of mass (tuning peak time): This refers to the time corresponding to the center of mass of the significant points of the auROC values ($p < 0.01$, permutation test). The center of mass was calculated as the average of the histogram ($\sum_i[\text{class value}_i \ \text{frequency}_i] \ / \ \sum_i \text{frequency}_i$). Only neurons with significant points for each analyzed condition were included in this analysis.

(2) Duration (tuning duration): This refers to the duration in which the auROC values were significant ($p < 0.01$, permutation test) for ≥5 consecutive bins, containing the time of center of mass. Only neurons with consecutive bins for each analyzed condition were included in this analysis.

(3) Onset time: The onset time refers to the time at which the duration was first evident.

We classified vTT cells (**Chapter 4**) with tuning peak times into five groups based on the epoch in which tuning peak time occurred during correct go trials. Of these, 7% of all cells had tuning peak times in the approach epoch, 24% in the odor-sampling epoch, 23% in the moving epoch, 11% in the waiting epoch, and 15% in the drinking epoch. The distribution of behavioral epoch-specific firing for each cell type (yellow and blue shadows in **Figure 4-2B**) was calculated as follows. First, for each cell group, the number of cells with significant excitatory (or suppressed) firing during each time bin for each task was calculated. Their distribution was estimated using Gaussian kernel smoothing via the fitdist function in MATLAB with a bandwidth of 100 msec. Second, the distribution of the significant excitatory (or suppressed) firing was compared with the cell-shuffled data for each cell group. To calculate the 99% confidence intervals of this distribution, we ran 1,000 iterations in which cellular group identities were randomized. We then calculated the distribution of significant excitatory (or suppressed) firing of each cell group, as above. For each bin in the tasks, the edges of the confidence interval were at the 0.5th and 99.5th percentiles of the distribution, as calculated from the cell-shuffled data. The significance of activity patterns for each cell group was determined by comparing the standard deviations of the data with those obtained from the cell-shuffled data, in which shuffling was performed 1,000 times by randomizing the cell selection.

Based on the ROC analyses during the odor-sampling epoch, we classified the NLOT neurons (**Chapter 5**) into five types (**Figure 5-2**). First, we calculated the auROC values of the go-cue versus baseline (1,000 to 0 ms before the end of the inter-trial interval) and the no-go-cue versus baseline during the odor-sampling epoch in the correct trials. Based on these values, we defined the cue odor selective population that exhibited significant responses for at least one cue odor presentation and cue odor non-selective population (type V neurons). Second, in the cue odor selective population, we also calculated the auROC values of the go-cue versus the no-go-cue during the odor-sampling epoch in the correct trials. Based on these values, we defined go-cue responsive neurons (significant go-cue > no-go-cue, type I neurons) and no-go-cue responsive neurons (significant go-cue < no-go-cue, type II neurons). Finally, in the remaining population, we also calculated the auROC values of cue odors (go-cue + no-go-cue) versus baseline during the odor-sampling epoch in the correct trials. Based on these values, we defined cue excitatory neurons (cue odors > baseline, type III neurons) and cue suppressed neurons (cue odors < baseline, type IV neurons). For all mentioned analyses, we tested for significance at $\alpha = 0.01$ (permutation test).

2.9. Data analyses: Generalized linear models (GLM)

To quantify the contribution of behavioral variables to neural activity, we used generalized linear models (GLM), which was a multiple linear regression with the firing rate of each neuron as the dependent variable, and predictors derived from the behavioral variables as the independent variables (Engelhard et al., 2019). In this analysis, the firing rate (5 ms bin width and smoothed by convolving spike trains with a 25 ms-wide Gaussian filter) of each neuron is described as a linear sum of temporal filters aligned to task events.

We quantified the relative contribution of each behavioral variable to neural activity by determining how the performance of the encoding model declined when each variable was excluded from the model (Engelhard et al., 2019; Pho et al., 2018). We predicted the firing rate of each neuron with all variables (full model) or by excluding one of the variables (partial model). The relative contribution of each behavioral variable was calculated by comparing the variance explained of the partial model to the variance explained by the full model.

2.10. Data analyses: Population vector construction and analyses

We constructed some conditions during the odor-sampling epoch, in which columns contained the auROC values of the correct trials corresponding to the trial-averaged firing rate changes from the baseline. By performing principal component analysis on the data, we reduced the dimensionality of the population from neurons to three PCs and obtained the odor-sampling epoch subspaces. To visualize the population responses, we projected the data onto the three-dimensional subspaces. This allowed us to obtain a point reflecting the response of the entire population for each of the two conditions at a given instant. The distance between the cue responses was computed as the Euclidean distance between pairs of activity vectors of all subspaces at a given instant (Cury and Uchida, 2010). The velocity of population responses was determined as the distance between successive 20 ms bins. These values were compared with the values during the baseline epoch.

2.11. Data analyses: Support vector machine (SVM) decoding analyses

We used a SVM algorithm with a linear kernel as a classifier (Cury and Uchida, 2010; Miura et al., 2012) and a MATLAB function (fitcsvm) for analyses. All analyses were conducted on trial data pooled across animals. A matrix containing concatenated firing rates for each trial and each neuron provided input to the classifier. The matrix dimensions were the number of cells by the number of trials. To avoid over-fitting, k-fold cross-validation (k = 10) was used to calculate the decoding accuracy of trial type discrimination. To compute the decoding accuracy, 20~40 trials for each trial type (from the start of the session) were chosen as the data. Next, the data were partitioned into ten equal parts; one part was used for testing and the remaining parts were used for training the classifier. This process was repeated ten times to test each individual part; the mean value of the accuracy was used for decoding accuracy. To compute the decoding accuracy of a 100 ms bin window (step: 20 ms), the classifier was trained and tested with a 100 ms bin window (step: 20 ms).

2.12. Histology

After recording, the rats and mice were deeply anesthetized using an intraperitoneal injection of sodium pentobarbital. Electric lesions were made using 10–20 μA direct current stimulation for 5 s of one of the four tetrode leads. The rats and mice were perfused transcardially with phosphate-buffered saline (PBS) and subsequently with 4% paraformaldehyde. The brains were removed from the skull and post-fixed in PFA. Next, the brains were cut into 50-μm thick coronal sections and stained with cresyl violet. The electrode track positions were determined in reference to the atlas developed by Paxinos and Watson.

2.13. *In situ* hybridization (Chapter 4)

Adult male mice (n=3) were used. Digoxigenin-(DIG)-labeled RNA probes for *Slc17a7* and *Gad1/2* were generated using an *in vitro* transcription kit (Roche, Basel, Switzerland), according to the manufacturer’s protocol using plasmids generously provided by Drs. Katsuhiko Ono and Yuchio Yanagawa. Brain sections (20-μm-thick) were mounted on glass slides (CREST, Matsunami, Osaka, Japan) using a paintbrush and dried overnight in a vacuum desiccator. The dried sections were then fixed in 4% PFA, digested with Proteinase K (10 μg/mL) for 30 min, and post-fixed in 4% PFA. After prehybridization, the sections were incubated overnight at 65°C with DIG-labeled RNA probes. After stringent washing, sections were blocked with 1% blocking reagent (11096176001, Roche) in TNT for 1 h. Subsequently, sections were incubated overnight at 4°C with alkaline phosphatase-conjugated anti-DIG antibody (1:1,000; Roche). Sections were then washed three times in TNT and once in TS 8.0 (0.1 M Tris-HCl, pH 8.0, 0.1 M NaCl, 50 mM MgCl2). Finally, alkaline phosphatase activity was detected using an HNPP fluorescence detection set (11758888001, Roche), according to the manufacturer's instructions. After three 30-min incubations, sections were washed with PBS. Finally, sections were counterstained with NeuroTrace green (Thermo Fisher Scientific, MA, USA) and mounted in PermaFluor (Thermo Fisher Scientific).

2.14. Retrograde tracing (Chapter 4)

Adult male mice were anesthetized with medetomidine (0.75 mg/kg i.p.), midazolam (4.0 mg/kg i.p.), and butorphanol (5.0 mg/kg i.p.), and then placed in a stereotaxic apparatus (SR-5M, Narishige, Tokyo, Japan). Injections were conducted with a syringe pump (UltraMicroPump III, WPI, FL, USA) connected to a Hamilton syringe (RN-1701, Hamilton, Nevada, USA) and a mounted glass micropipette with 50 μm tip diameter connected to the syringe with an adaptor (55750-01, Hamilton).

Cholera toxin B subunit (CTB) conjugated with Alexa 555 (Thermo Fisher Scientific) was unilaterally or bilaterally injected (300 nL at 100 nL/min) into the medial prefrontal cortex (A/P, 2.4 mm; M/L, 0.4 mm from bregma; D/V, 1.0 mm from the brain surface; n = 3 from 2 mice), OB (A/P, 4.3 mm; M/L, 0.8 mm from bregma; D/V, 1.5 mm from the brain surface; n = 3 from 2 mice), AON (A/P, 2.8 mm; M/L, 1.3 mm from bregma; D/V, 2.6 mm from the brain surface; n = 3 from 2 mice), OT (A/P, 1.5 mm; M/L, 1.0 mm from bregma; D/V, 4.7 mm from the brain surface; n = 5 from 3 mice), aPCx (A/P, 2.3 mm; M/L, 1.8 mm from bregma; D/V, 3.4 mm from the brain surface; n = 4 from 4 mice), or pPCx (A/P, -1.5 mm; M/L, 3.6 mm from bregma; D/V, 4.5 mm from the brain surface; n = 3 from 2 mice), or vTT (250 nL; A/P, 0.3 mm tilted 30°; M/L, 0.4 mm from bregma; D/V, 4.6 mm from the brain surface; n = 3 from 2 mice). After surgery, mice received atipamezole (0.75 mg/kg i.p.) and ketprofen (5 mg/kg, i.p.). One week later, mice were deeply anesthetized and perfused with saline followed by 4% PFA under anesthesia. Brains were sliced into 50-μm-thick coronal sections.

Sections were examined with a confocal laser microscope (FV1200, Olympus, Tokyo, Japan) and a bright-field and fluorescent microscope (Zeiss, Oberkochen, Germany).

In the following chapters, I describe our analyses of the aPCx (Chapter 3), vTT (Chapter 4), NLOT (Chapter 5), and ACo (Chapter 6) neural activity recorded during the odor-guided behavioral tasks (Figure 1-4).

Chapter 3. Research: anterior piriform cortex (aPCx) in the OC

3.1. Short summary

The anterior piriform cortex (aPCx) in the OC mediates the processing of incoming olfactory sensory signals and top-down cognitive signals originated in higher order regions. However, it remains unknown how neurons in the aPCx represent top-down cognitive signals and integrate them with olfactory sensory signals. Using an extracellular recording, we demonstrated that individual aPCx neurons responded and maintained a specific state of subsequent animals' behaviors that were predicted by the cue odors even after the reversal learning, whereas the firing pattern during odor presentation exhibited various changes during the reversal learning. Based on these results, we report here unique behavioral state representations in the OC and speculate that aPCx neurons have

an important role in the association between flexible odor representations and top-down signals related to odor-guided learned behaviors.

3.2. Introduction

The piriform cortex, the largest of the olfactory cortical regions, receives not only olfactory sensory signals but also top-down cognitive signals originated in higher order regions. On one hand, the piriform cortex, particularly the aPCx, has strong reciprocal connections with the olfactory bulb shown by neural tracing studies (Ghosh et al., 2011; Igarashi et al., 2012; Luskin and Price, 1983a; Miyamichi et al., 2011; Mori and Sakano, 2011; Nagayama, 2010; Sosulski et al., 2011). Olfactory bulb neurons project broadly to the aPCx, and neural recording studies showed that odor stimulation activates widely distributed neurons in the aPCx without an odor-specific topography (Miura et al., 2012; Rennaker et al., 2007; Stettler and Axel, 2009; Uchida et al., 2014; Zhan and Luo, 2010). On the other hand, the piriform cortex also receives substantial top-down projections originated in higher order regions that are involved in processing expectation, working memory, and decision-making. For example, the aPCx receives projections from the orbitofrontal cortex (OFC) (Johnson et al., 2000). In rats trained to perform an odor-outcome association task, both aPCx and OFC neurons fired during odor-sampling and the outcome-related periods such as the period of expectation of the outcomes (Roesch et al., 2006).

Based on these observations, it has been proposed that the piriform cortex may function not only as a primary sensory region but also as an olfactory association cortex, integrating odor sensory signals with top-down cognitive signals necessary for performing odor-guided behaviors. To investigate the associative relationship in olfactory circuits, the aPCx is a good candidate for the reasons above; however, the electrophysiological features that directly explain the rules has been poorly explored. Specifically, most previous studies have focused on the aspect of the aPCx activity during odor presentation (Miura et al., 2012; Stettler and Axel, 2009) and not on the activity of the olfactory cortex during freely-moving odor-guided behavior (Shiotani et al., 2020b; Tanisumi et al., 2021) driven by top-down inputs. Indeed, recent studies have been emphasizing the importance of behavioral states and motion signals supplied to the sensory cortex in information processing (Parker et al., 2020; Speed and Haider, 2021; Stringer et al., 2019). Therefore, the purpose of the present study was to understand how top-down signals are expressed in the aPCx and associated with olfactory sensory signals.

Herein we recorded neural ensemble activity in the aPCx of freely moving rats performing the go/no-go association task and its reversal. During odor-sampling, many aPCx neurons responded to a specific combination of cue odors. Many of them also showed increased firings during a specific state of subsequent behaviors that were predicted by the cue odors (i.e., moving to the reward port, reward waiting, drinking, and waiting on no-go trials). Furthermore, most of them maintained their behavioral state selective firings even after the reversal learning, whereas the firing pattern during odor-sampling exhibited various changes during the reversal learning. Our results suggest that aPCx neurons play an important role in the association between flexible cue odor representations and stable top-down cognitive state signals that occur during odor-guided learned behaviors.

3.3. Results: Distributed cue odor representations and sequential behavioral state signals

We recorded data from 251 well-isolated neurons in the aPCx of three rats performing the go/no-go association task using four odors (**Figure 3-1A**). Briefly, the go trial requires the rat to first sample a go-cue odor stimulus presented at an odor port and then to move to a reward port to receive water (go response). Conversely, the no-go trial requires the rat to first sample a no-go-cue odor stimulus presented at the odor port and then to stay near it to wait for the next trial (no-go response). The cue odors used in a session consisted of four of the eight pure odors or four of the eight mixed odors. In each session, two cue odors induced the rat to make go responses, and another two induced the rat to make no-go responses. Below, we describe our analyses of the neural activity recorded during odor-sampling and the performing of odor-guided behaviors.

Firstly, we focused on the odor selective firing during cue odor presentation. For most of the neurons recorded, we found that aPCx neurons had a wide variety of odor selective responses during cue odor presentation irrespective of the odor set used as cue. As a population, 57% of aPCx neurons were activated by at least one of the four odors tested while 44% were activated by two or more ($p < 0.01$, Wilcoxon rank-sum test). Therefore, the aPCx responses to the cue odors were observed in a widely distributed, moderately sparse neural population, which is consistent with previous studies (Miura et al., 2012; Rennaker et al., 2007; Stettler and Axel, 2009; Uchida et al., 2014; Zhan and Luo, 2010).

Secondly, our findings revealed that most of these odor selective neurons also responded to the odor-guided behavioral epochs: the movement to the reward port, waiting for the rewards, consumption of the rewards, and waiting on no-go trials. For instance, the neuron in **Figure 3-1B** left was excited sharply by the reward-predicting odor and the early phase of the reward-waiting epoch. This figure also shows that intervals of time between the behavioral states varied across trials (**Figure 3-1B** left top). To develop an overall response profile despite this timing variability, we created EASH (Ito and Doya, 2015), which is derived by linearly scaling time intervals between behavioral states in each trial to the median interval across all trials. EASH shows clearly that individual aPCx neurons fired to cue odors and the specific behavioral state on go/no-go trials (**Figures 3-1B** right**, 3-2A, and 3-2B**). To quantify the dependence of state-selective firings to each behavioral state, we calculated response changes of EASHs from baseline (during inter trial interval periods) in 100 msec bins using a ROC analysis. We calculated the auROC at each time bin. auROC values ranged from -1 to +1, with positive and negative values reflecting increased and decreased firing rates relative to baseline, respectively. We further determined the auROC value significance using a permutation test. Across the population, we found that many cue odor-selective cells significantly responded to each behavioral state (**Figures 3-2C and 3-2D**; colored lines were significantly selective, $p < 0.01$, permutation test). Go-cue odor selective neurons significantly increased from the baseline rate for two consecutive bins (200 msec) during moving epoch (27.7%), waiting for the reward epoch (21.1%), and drinking epoch (20.3%). No-Go-Cue odor-selective neurons increased from the baseline rate for two consecutive bins (200 msec) during waiting epoch (42.3%) on no-go trials.

Compared to the wide variety of odor-selective responses, behavioral state-selective responses did not differ between cue odors having the same meaning (go cue odor-1 [G1] vs. go cue odor-2 [G2], no-go cue odor-1 [N1] vs. no-go cue odor-2 [N2]). To qualify this, we also calculated the auROC values between these same cue odors. We firstly calculated the values during the odor presentation between same cue odors and defined “primary preferred go/no-go-cue odor” and “less preferred go/no-go-cue odor” in each session. Then, auROC values were adjusted as a response between primary preferred cue odor vs. less preferred cue odor. Across the population, we found that many cue odor-selective neurons had no selectivity for a single cue odor after odor port exit (**Figures 3-2E and 3-2F right**; colored lines were significantly preferred, $p < 0.01$, permutation test). We next defined the peak time of behavioral state responses, which is the center of mass of the significantly increased points from baseline ($p < 0.01$, permutation test). Each peak was calculated using the auROC values between each cue odor and the baseline after the odor port exit. These peaks overlapped across the population, appearing at approximately the same time for go-cue odors (**Figure 3-2E left**) and at slightly different times for no-go-cue odors (**Figure 3-2F left**). Thus, individual aPCx neuron expressed not only odor signals, but also the odor-guided behavioral state signals. In the following sections, we focus on the relationships between odor selectivity and odor-evoked behavioral state selectivity.

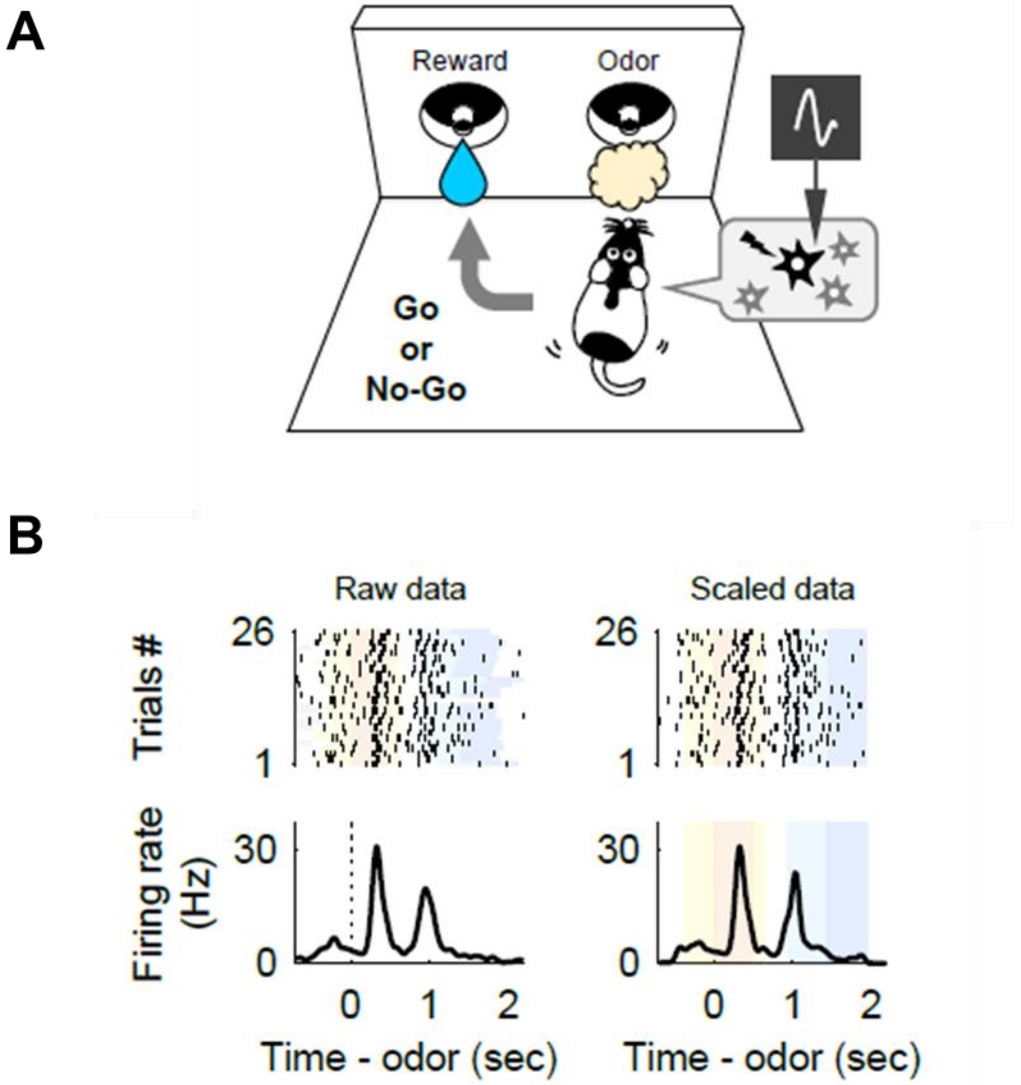

Figure 3-1 | Electrophysiological recordings in the aPCx of freely moving rats performing the odor-guided go/no-go association task

(**A**) Schematics of the odor-guided go/no-go association task.

(**B**) An example of event-aligned spike data. Colored shading indicates the odor delay (yellow), odor presentation (orange), odor valve offset to odor port exit (yellow), waiting (light blue), and drinking (blue) behavioral epoch.

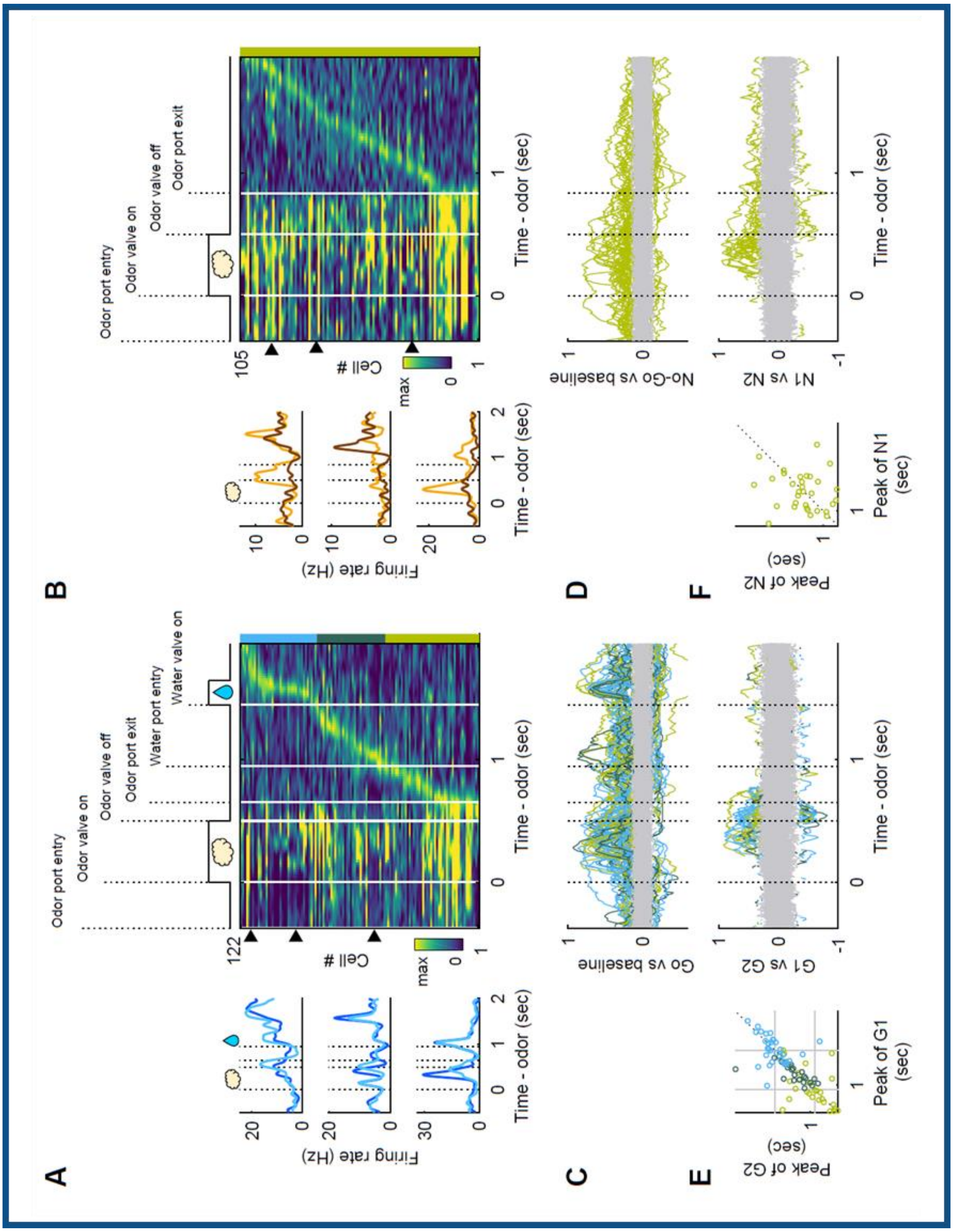
A
B
C
D
E
F
Odor port entry
Odor valve on
Odor valve off
Odor port exit
Water port entry
Water valve on
Firing rate (Hz)
Time - odor (sec)
Cell #
122
105
max
0
Go vs baseline
G1 vs G2
No-Go vs baseline
N1 vs N2
Peak of G1 (sec)
Peak of G2 (sec)
Peak of N1 (sec)
Peak of N2 (sec)

Figure 3-2 | Distributed cue odor representations and sequential behavioral state signals

(**A**) Left panel: examples of event-aligned spike data for three representative cells tuned to specific go-cue odors and behaviors (go cue odor-1 and -2). Right panel: event-aligned firing rates for correct go trials for go-cue odor selective neurons, sorted by the peak time for the max values after odor-sampling. Each row corresponds to one cell. Vertical white lines indicate transitions between behavioral epochs. Right top panel: event-aligned behavioral epochs of the task by EASHs (time scale: odor valve on ~ off, 0.5s). As behavioral epoch durations varied for each trial, the median duration of the epoch was calculated. Spike timing during each epoch and for each trial was linearly transformed to correspond with the median duration of each behavioral epoch.

(**B**) Same as (**A**), for correct no-go trials.

(**C**) auROC values were calculated from event-aligned spike data for the cells. The values were calculated by comparing go correct trials to baseline in sliding bins. Colored lines were significantly selective, $p < 0.01$, permutation test; each line color was defined by where the firing peak after odor-sampling in (**A**).

(**D**) Same as (**C**), for correct no-go trials.

(**E**) Left panel: the center of mass (peak) of the significantly increased points from baseline of each go-cue condition. Right panel: auROC values were calculated as a response between primary preferred go-cue odor vs. less preferred go-cue odor. Colored lines were significantly preferred, $p < 0.01$, permutation test.

(**F**) Same as (**E**), for correct no-go trials.

3.4. Results: Associative correlation in the odor and behavioral state firings

In the odor and behavioral state-selective population, the neurons that expressed go-cue odors-selective firings during odor presentation tended to enhance their behavioral state firings during go-cue odor-guided behaviors (**Figures 3-2A and 3-2C**). Conversely, the neurons that expressed no-go-cue odors-selective firings during odor presentation tended to slightly enhance their firings to the early phase of the waiting state during a no-go-cue odor-guided behavior (**Figures 3-2B and 3-2D**). To quantify the encoding relationship between the odor and behavioral state firings, we calculated the auROC values during the behavioral states in each odor-selective subpopulation (**Figure 3-3A**). The cumulative sums of the auROC values that significantly increased from baseline (**Figure 3-3B**; $p < 0.01$) were higher than the control at each time bin (shuffled categories of odor selective neurons), excluding the that of the late phase in the less preferred no-go cue odor-selective neurons. In addition to this evaluation, we calculated the Lorenz curve of these cumulative sums, describing inequality among the sequential behavioral state firings (**Figure 3-3B**). The Gini coefficient, which is the ratio of the area that lies between the line of perfect equality and the observed Lorenz curve over the total area under the line of equality, was significantly higher than the control ($p < 0.01$, shuffled categories of odor-selective neurons). These results suggest that each odor-selective population represented a relatively equal tiling of the behavioral states evoked by the odor.

Thus, when a group of neurons that selectively respond to each odor was collected, the behavioral state signals were assembled to cover the behaviors lead by that odor. It is possible that subpopulations defined based on go/no-go cue response profiles exhibit behavioral states that reflect go/no-go directional profiles, indicating that go/no-go association relationships are represented within the aPCx when subpopulations are overlooked. To verify the details of the behavioral state signal contained in the subpopulation determined by the odor response profile, we first used k-means clustering to classify the odor selectivity of individual neurons into six types based on the auROC epoch values of the go/no-go odor conditions (**Figure 3-3C**). Clusters were ordered in the high value of go-cue odors vs. no-go cue odors and were stable. Then, we calculated the cumulative auROC values of the go/no-go behavioral states in each cluster (**Figure 3-3D**). The go-cue odors-selective clusters have high values in the go behavioral states, as well as the no-go-cue odors and no-go behavioral states. We summarized this by comparing the mean of go/no-go cue odor preference values with the state value index: the cumulative values of go behavioral states / the cumulative values of no-go behavioral states (**Figures 3-3E**). For a cluster that prefers go/no-go-cue odors and their following go/no-go states, the plot falls along the line x = y. Clearly, values were correlated for go/no-go preference, demonstrating that there was a positive correlation between the selectivity for cue odors and odor-guided behavioral states in the aPCx populations. Furthermore, to maximize the reliability of this result, a set of 80% resampled datasets obtained by subsampling without replacement were clustered into six clusters, and the correlation was evaluated. Similar results were observed for each dataset 1000 times. These results indicate that although individual aPCx exhibit a variety of odor response patterns (Miura et al., 2012; Stettler and Axel, 2009), each of these represents an odor-outcome association that also expresses the behavioral state guided by the odor, thus establishing the aPCx associative representation.

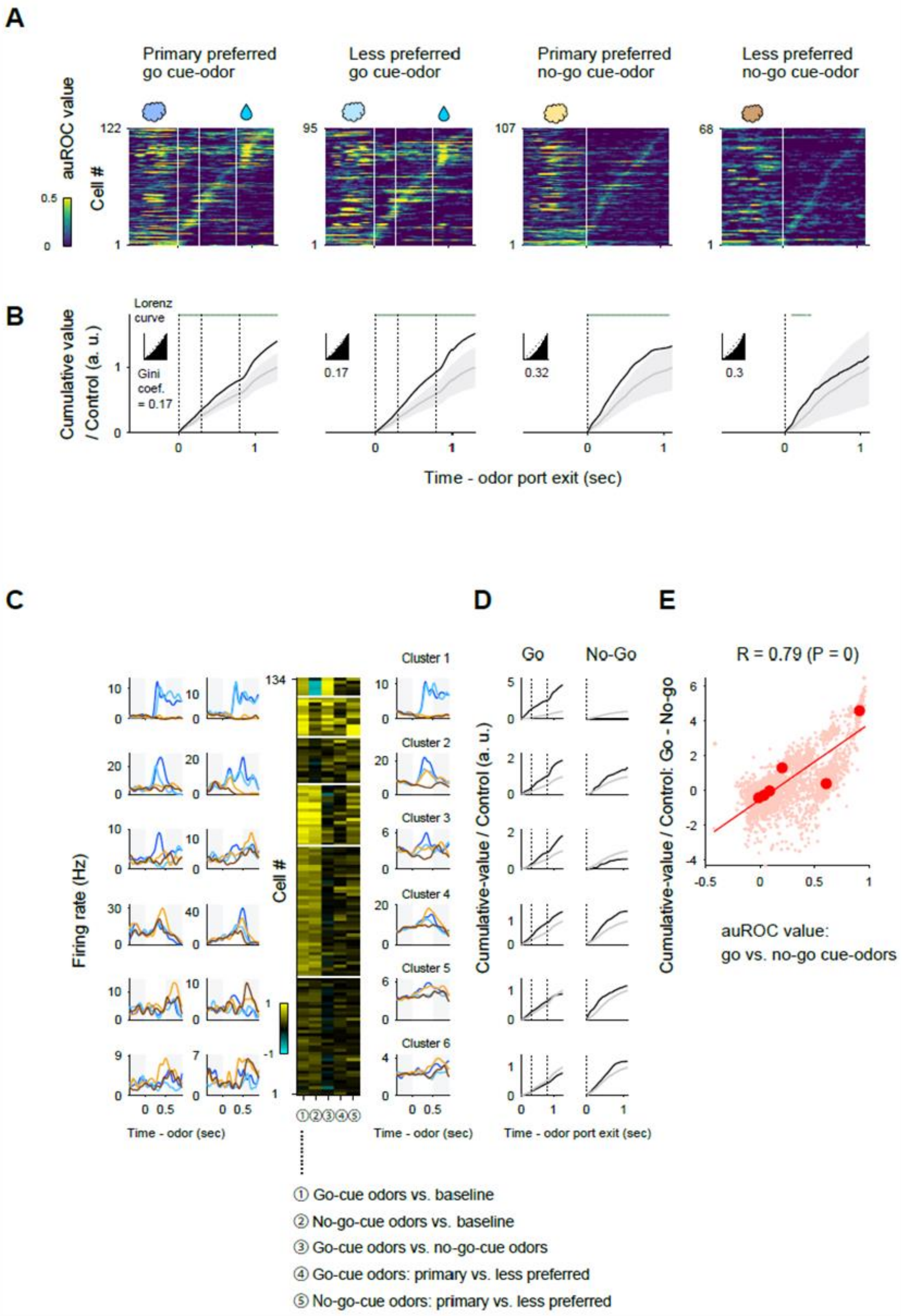
A
Primary preferred go cue-odor
Less preferred go cue-odor
Primary preferred no-go cue-odor
Less preferred no-go cue-odor
auROC value
0.5
0
Cell #
122
95
107
68
1
B
Lorenz curve
Gini coef. = 0.17
0.17
0.32
0.3
Cumulative value / Control (a. u.)
Time - odor port exit (sec)
C
Firing rate (Hz)
Time - odor (sec)
Cell #
134
Cluster 1
Cluster 2
Cluster 3
Cluster 4
Cluster 5
Cluster 6
①②③④⑤
① Go-cue odors vs. baseline
② No-go-cue odors vs. baseline
③ Go-cue odors vs. no-go-cue odors
④ Go-cue odors: primary vs. less preferred
⑤ No-go-cue odors: primary vs. less preferred
D
Go
No-Go
Cumulative-value / Control (a. u.)
Time - odor port exit (sec)
E
R = 0.79 (P = 0)
Cumulative-value / Control: Go - No-go
auROC value: go vs. no-go cue-odors

Figure 3-3 | Associative correlation in the odor and behavioral state firings

(**A**) auROC values were calculated from event-aligned spike data for each odor-selective cells, sorted by the peak time for the values after odor-sampling. Each row corresponds to one cell.

(**B**) The cumulative sums of the auROC values (black line) that significantly increased from baseline. The values were compared to the control values (gray line, shuffled categories of odor selective neurons) at each time bin. The Lorenz curve of these cumulative sums describes inequality among the sequential behavioral state firings.

(**C**) Clustering results based on the auROC epoch values of the go/no-go odor conditions. Clusters were ordered in the high value of go-cue odors vs. no-go cue odors. The right panel indicates averaged firing rates for each cluster.

(**D**) The cumulative auROC values of the go/no-go behavioral states in each cluster (black value). The values were compared to the control values (gray line, shuffled categories of cluster) at each time bin.

(**E**) The mean of go/no-go cue odor preference values vs. the state value index: the cumulative values of go behavioral states / no-go behavioral states. Light colored plots show the 80% resampled datasets obtained by subsampling without replacement and clustered into six clusters for each dataset 1000 times.

3.5. Results: Changing formats of individual selective firing of odor and behavioral states during reversal learning

To examine the dependence on learning of the odor and behavioral states encoded in the aPCx, we also recorded neural activity in rats engaged in a reversal learning task in which the associations between cue odors and outcomes were first well learned, and then suddenly changed within the same sessions (**Figure 3-4A**). After reversal, rats had learned the reversed cue-outcome associations and reached criterion performance (16/20 correct responses in a moving block of 20 trials for 10 consecutive trials) (**Figure 3-4B**).

After criterion performance was reached, the associations between the odor and behavioral state firings were also observed (**Figure 3-4C**) across the aPCx population (**Figure 3-5A**; The analysis methods are the same as in **Figures 3-3A and 3-3B**). Across the reversal learning, many odor- and behavioral state-selective neurons maintained the behavioral state-selective firings, respectively, whereas the odor-selective firings during the odor presentation exhibited various changes in their firing patterns before or after reaching criterion performance (**Figure 3-4C**). We qualified these firing changes of the tuning profiles and their speed in each state by the following two analyses. First, we evaluated the similarity of the odor and behavioral state's tuning profiles between the original criterion and reversal criterion based on the Pearson's correlation coefficient

(**Figure 3-6A**). The correlation coefficient distribution of the odor tuning profiles was wide, while that of the behavioral state tuning profiles was close to 1, suggesting a similarity. Second, we evaluated the speed of the firing changes in each state by fitting the firing rates on go response trials after reversal as the psychometric function (**Figure 3-6B**). We then defined trials of the increased peak in each state and compared the odor with the behavioral state ($p < 0.01$, paired t-test). The firing change speed in each behavioral state tended to be faster than the change speed of odor-selective firings. These results indicate that the firing changes of the odor and behavioral states encoded in the aPCx depended on learning and expressed two features, flexible odor representations and steady top-down signals related to odor-guided behaviors.

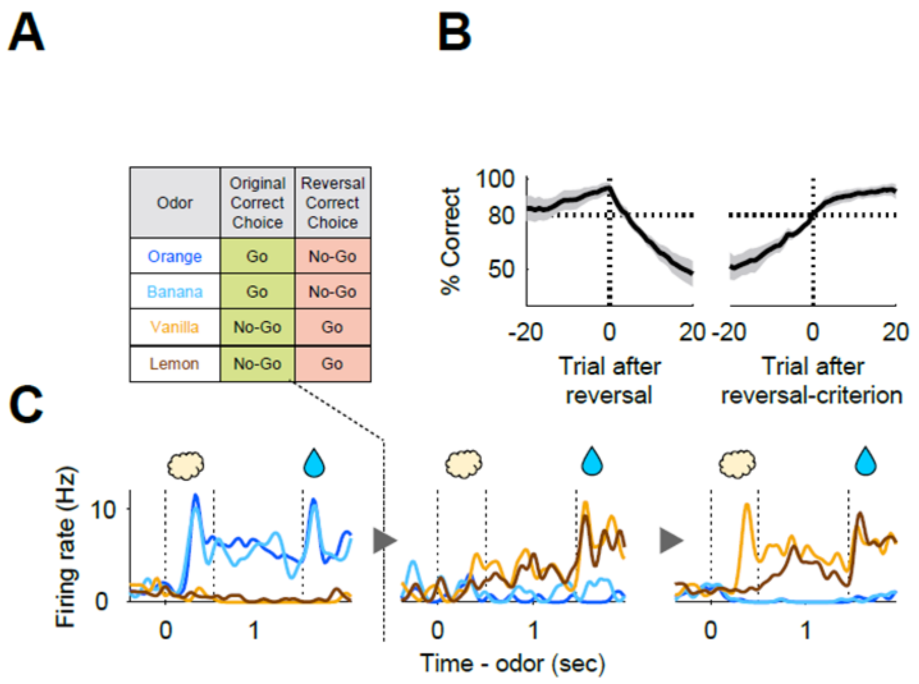

Odor	Original Correct Choice	Reversal Correct Choice
Orange	Go	No-Go
Banana	Go	No-Go
Vanilla	No-Go	Go
Lemon	No-Go	Go

Figure 3-4 | Reversal learning of the odor-guided go/no-go association task

(**A**) Table of correct choices in an example session.

(**B**) Averaged learning curve before and after reversal.

(**C**) Change of firing rate of an example cell during reversal learning: original, before, and after reaching criterion performance.

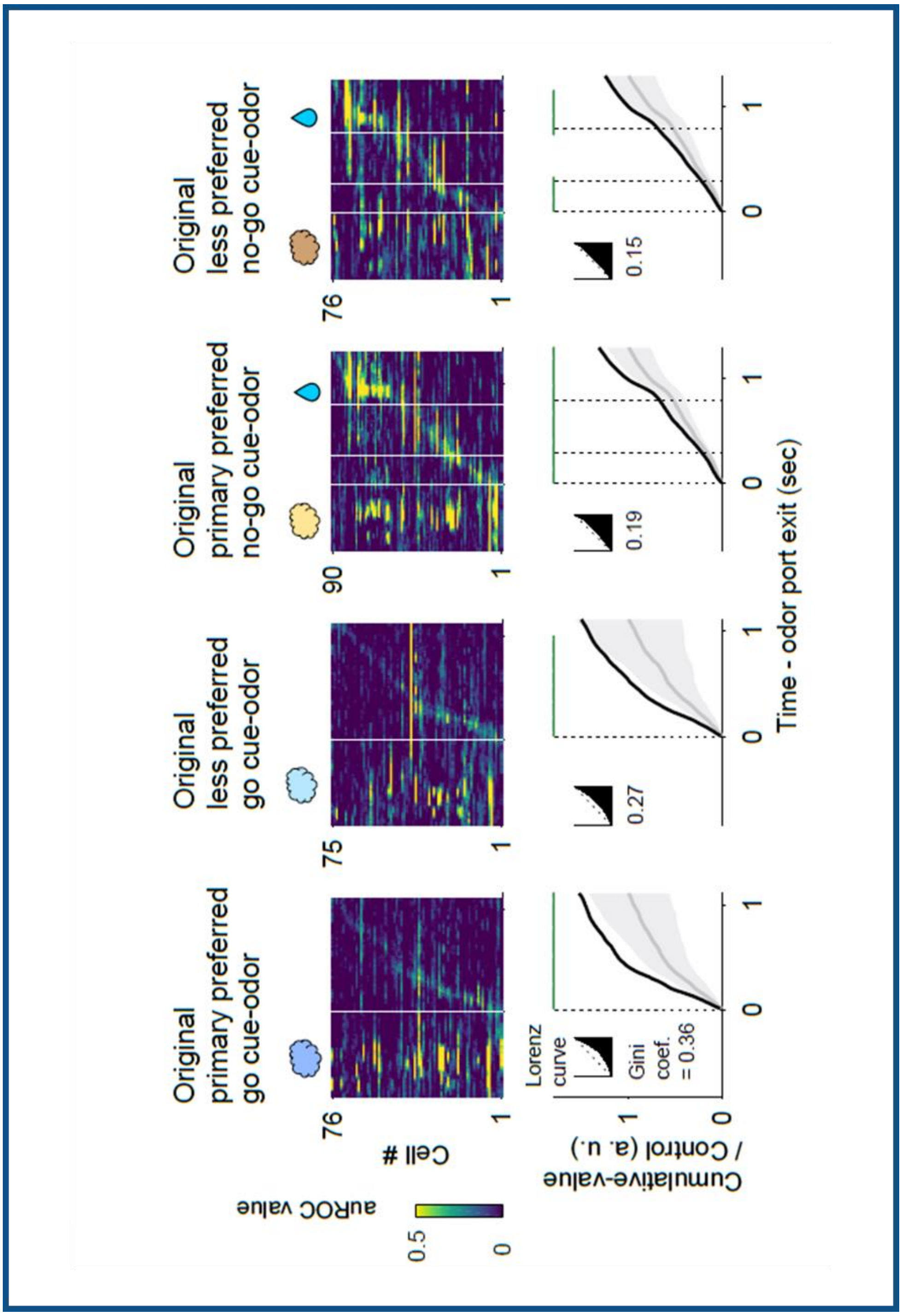

Figure 3-5 | Associative correlation in the odor and behavioral state firings after reversal learning

Same as **Figures 3-3A and 3-3B**, for after reversal learning.

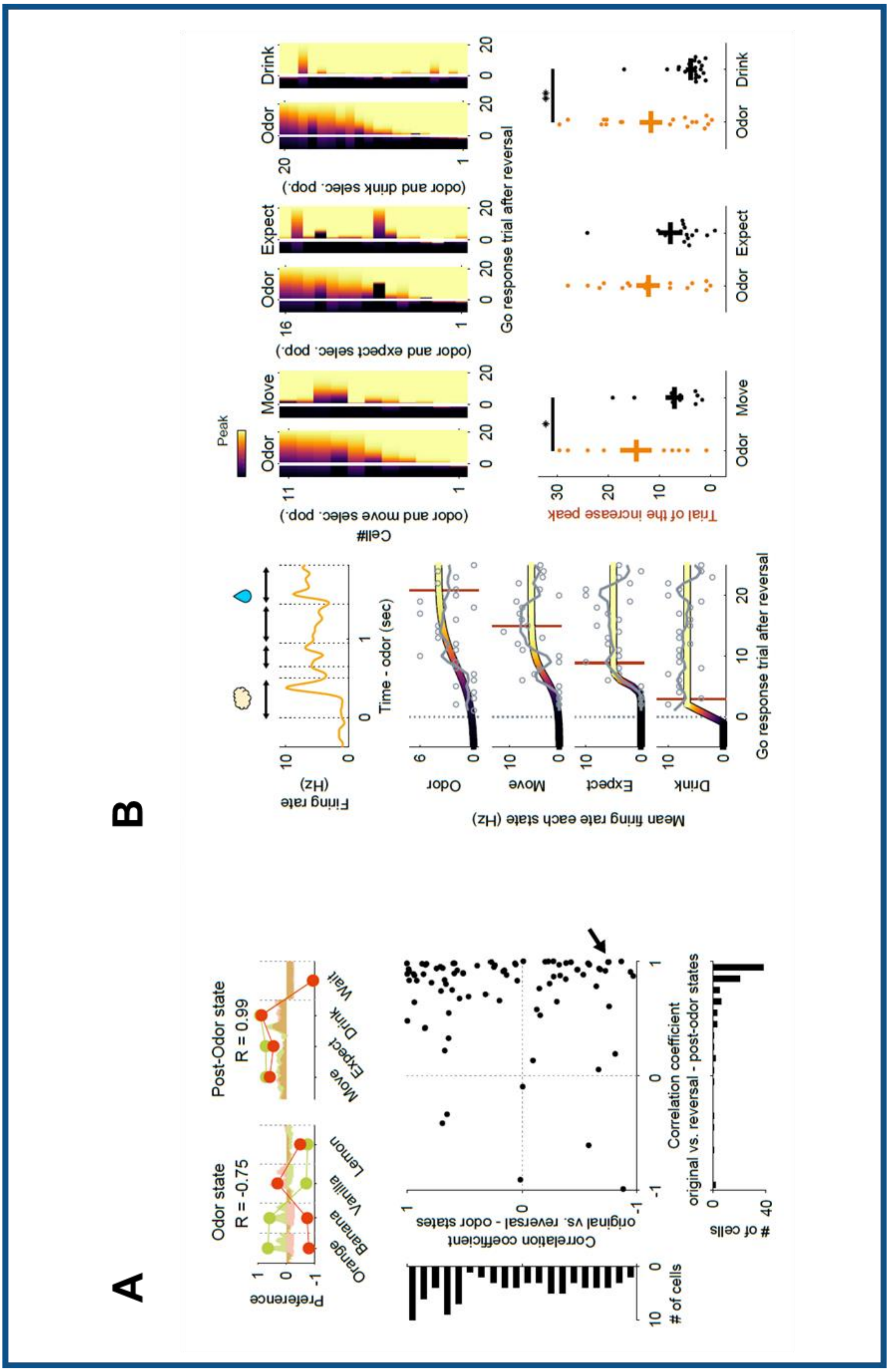
A
Odor state
R = -0.75
Post-Odor state
R = 0.99
Preference
1
0
-1
Orange
Banana
Vanilla
Lemon
Move
Expect
Drink
Wait
Correlation coefficient
original vs. reversal - odor states
Correlation coefficient
original vs. reversal - post-odor states
# of cells
10
0
40
-1
0
1
B
Firing rate (Hz)
Time - odor (sec)
Mean firing rate each state (Hz)
Odor
Move
Expect
Drink
Go response trial after reversal
Peak
Cell#
(odor and move selec. pop.)
(odor and expect selec. pop.)
(odor and drink selec. pop.)
11
16
20
1
Trial of the increase peak
30
20
10
0
*
**

Figure 3-6 | Quantifying the firing change of the tuning profile and their speed in each state during reversal learning

(A) Response similarity of the odor and behavioral state's tuning profiles between the original criterion and reversal criterion based on the Pearson's correlation coefficient. Tuning profile values were calculated by the auROC values relative to baseline in each state. The top panel indicates a tuning profile of an example cell (green, original criterion; red: reversal criterion).

(**B**) Quantifying and comparing the number of trials to reach the peak of response increase for each go-behavioral state response. The left panel indicates a response fitting in each state of an example cell. To qualify the firing changes each state and define their peaks during reversal learning, we first extract significantly odor- and behavior-state selective cells base on the auROC value for each state (the right top panels) and fit them using a psychometric function. The defined increase peaks were compared between odor- and behavior-state selective firings ($p < 0.01$, paired t-test) for each state (the right bottom panels).

3.6. Results: Stable population coding in the aPCx during the completed learning period

While individual aPCx neurons' odor–outcome encoding properties change in a learning-dependent manner (**Figures 3-4, 3-5 and 3-6**), does the structure of the relationship between population activity patterns change or remain stable? To gain insight into the dynamics of the population response, we visualized the average population activity using principal component analysis, a dimensionality reduction method. **Figure 3-7A** top shows the trajectories of the mean response of the aPCx neuron population to go-cue and no-go-cue odors, represented as the projections onto the first three PCs during the odor sampling epoch. For the evaluation of coding differences between conditions for population activities at each learning stage, the instantaneous separation of the population responses was measured in the original criterion, reversal learning, and reversal criterion periods, respectively (**Figure 3-7A** bottom). Across all learning stages, the trajectory remained convergent for approximately 200 ms after the odor onset, and there was little difference between conditions when compared to the degree of convergence during the baseline. During the 300–700 ms after the onset of the odor, the subspace trajectory of the odor sampling epoch began to spread out and was separated at the population level, suggesting stability of the population coding. Importantly, in the late phase of odor sampling, the distances between odors with the same meaning (primary vs. less preferred go/no-go-cue odors) tended to converge, whereas the distances between conditions with different meanings tended to remain above the baseline levels over the initiation of cue-odor-evoked behaviors. This trend emerged in the original and reversal criterion periods but disappeared in the reversal learning period. Taken together, the population of aPCx neurons developed dramatic transitions in the dynamics of cue encoding at 300–700 ms after odor onset and, specifically, stable population representations of differences between go/no-go conditions in a learning-dependent manner.

To further investigate the stability of population coding, we performed a decoding analysis to evaluate whether population activity explains the accuracy of the animals' behavioral accuracy at each learning stage. This analysis determined whether the firing rates of the aPCx neuron populations could be used to classify each trial as go or no-go. We used SVMs with linear kernels as a decoder. Analyses of the decoding time course based on aPCx neurons using a sliding time window revealed that the decoding accuracy was maintained at chance levels 200 ms after odor onset; subsequently, it increased above the level of animals' behavioral accuracy 300–700 ms after the odor onset (**Figure 3-4B**). The explanation for this animal's behavioral performance was obvious over the initiation of cue-odor-evoked behaviors during the original and reversal criterion periods, but became a little unclear during the reversal learning period. Thus, the aPCx neuron population activity was stable enough to provide sufficient information to explain the accuracy of behavior 300 ms after odor onset, even though individual coding properties were variable.

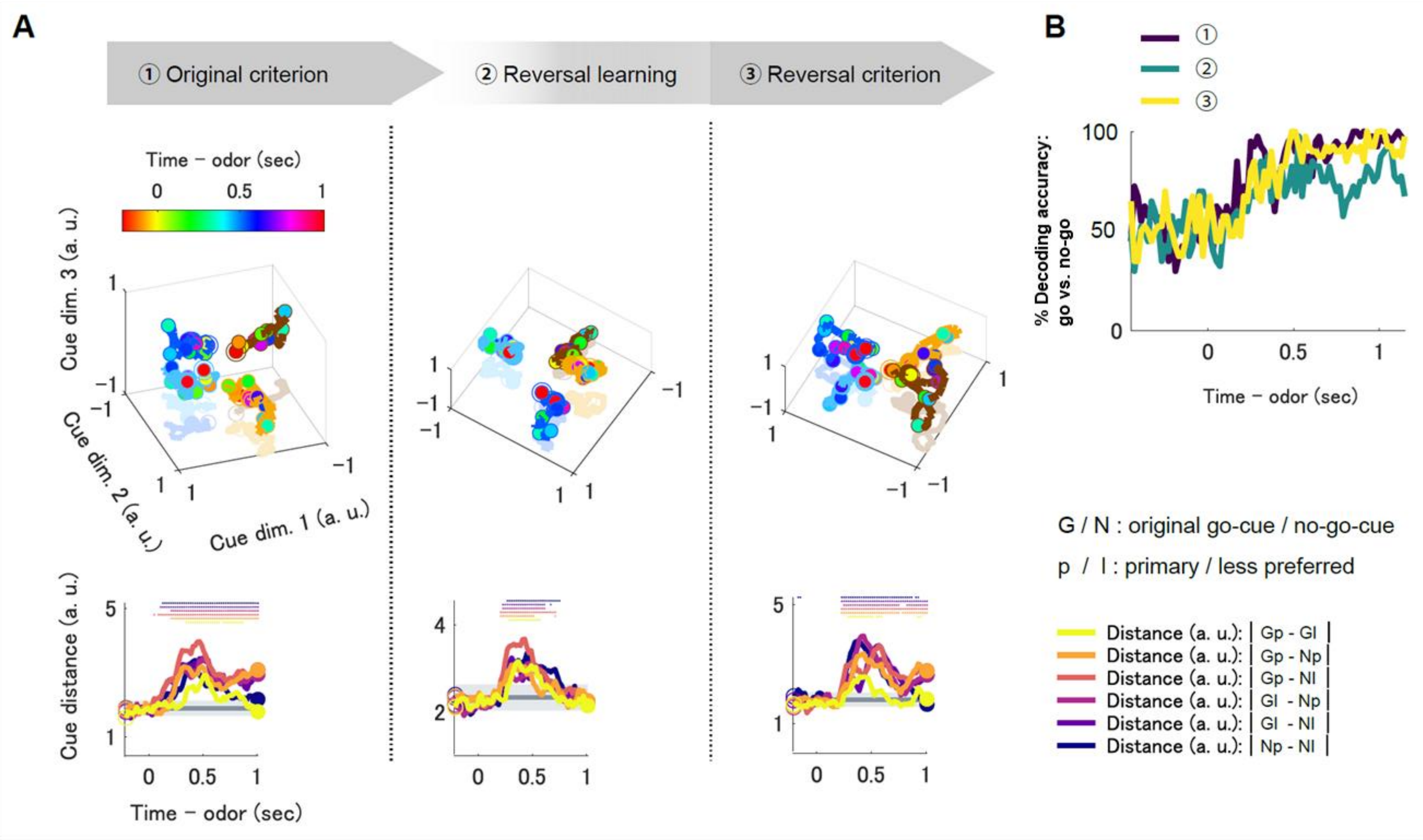
A
① Original criterion
② Reversal learning
③ Reversal criterion
Time − odor (sec)
0
0.5
1
Cue dim. 3 (a. u.)
Cue dim. 2 (a. u.)
Cue dim. 1 (a. u.)
1
−1
Cue distance (a. u.)
5
4
2
1
Time − odor (sec)
B
①
②
③
% Decoding accuracy: go vs. no-go
100
50
0
Time − odor (sec)
G / N : original go-cue / no-go-cue
p / l : primary / less preferred
Distance (a. u.): | Gp - Gl |
Distance (a. u.): | Gp - Np |
Distance (a. u.): | Gp - Nl |
Distance (a. u.): | Gl - Np |
Distance (a. u.): | Gl - Nl |
Distance (a. u.): | Np - Nl |

Figure 3-7 | Stable population coding in the aPCx during the completed learning period

(**A**) Top: visualization of the aPCx neuron population responses during odor-sampling epoch using principal-component analysis. The responses to cue odors are projected onto the first three PCs corresponding to the odor-sampling epoch subspaces. Blue/light blue lines, primary/less go-cue odor; orange/brown lines, primary/less no-go-cue odor. Temporal progression is depicted from unfilled colored spheres to filled colored spheres. Bottom: the distances between the neuron population responses. The gray line and shaded areas show the mean ±2 standard deviation (SD) baseline values during the baseline epoch. Top dots indicate the time bins showing values more than mean +2 SD baseline values.

(**B**) Time course of go/no-go cue decoding accuracy for each learning state. A vector consisting of instantaneous spike counts for all neurons in a sliding window was used as an input for the classifier. Training of the classifier and testing was performed at every time point.

3.7. Discussion

The purpose of the present study was understanding how neurons in the aPCx represent top-down cognitive signals and integrate them with olfactory sensory signals. In this study, we demonstrated that individual odor-selective neurons expressed specific behavioral state signals that were predicted by the go/no-go-cue odors before and after the reversal of cue–outcome contingencies (**Figures 3-3A and 3-5**). These results suggest that aPCx neurons participate in the communication of the flexible odor representations with the sequential top-down signals required for learning of odor-guided behaviors.

One of the most well-researched olfactory cortex areas, aPCx, expressed a variety of behavioral state response patterns (**Figure 3-2**) in addition to the traditional distributed odor information representation patterns (Miura et al., 2012; Rennaker et al., 2007; Stettler and Axel, 2009; Uchida et al., 2014; Zhan and Luo, 2010), possibly related to the association between odor information and animal behavioral states (**Figure 3-3**). These response patterns had the following three properties. First, the response pattern of the aPCx changed in a learning-dependent manner (**Figures 3-4, 3-5, and 3-6**). This finding suggests that the aPCx is not only a sensor that receives odor information, but also has a system that constantly updates the odor-related information. Our results are consistent with recent reports stating that odor representation patterns in the aPCx continue to be updated with learning (Pashkovski et al., 2020; Schoonover et al., 2021). Second, while the odor representations of individual neurons gradually and flexibly varied in response to rule changes, the behavioral state representations stably maintained the same information without changing their responses before and after rule changes (**Figures 3-6A and 3-6B**). In addition, both odor and behavioral state representations were stable at the population level (**Figure 3-7**). The knowledge that neural representations of individual neurons are fluid but stable at the population level has been reported in various regions of the brain (Deitch et al., 2021; Schoonover et al., 2021). The coexistence of drifting representations for odors and stability for behavioral state representations in the aPCx has provided new insights to the previous studies. Third, there were associative relationships between the odor and behavioral state properties of individual neurons that corresponded to the go/no-go conditional directions (**Figures 3-3A, 3-5 and 3-7**). This finding suggests that bottom-up and top-down communication occurs in the aPCx to preserve the association between odor and odor-evoked behavioral states at the population level in response to rule changes, that is, environmental changes, and that the associative information continuously being updated. These three properties support the hypothesis that one of the functions of the aPCx is to adapt to learning and to associate distributed and flexible odor information with stable behavioral state information.

We acknowledge that there are several limitations to this study. First, it is necessary to suppress aPCx directly with muscimol or other such methods to examine whether there is any effect on normal and reversal learning. Second, the source of the behavioral state signals represented by the aPCx remains unclear. As the candidates, the OFC and prefrontal cortex (PFC), which represent the behavioral states, higher-order variables, and state-space of animals (Hirokawa et al., 2019; Hyman et al., 2012; Schuck et al., 2016) are reasonable. Therefore, it is necessary to investigate the causal evidence of the top-down pathway from the OFC to the aPCx and the pathway from the PFC to the aPCx via the ventral tenia tecta (vTT) in the olfactory cortex (Shiotani et al., 2020b) in regulating the behavioral state responses of the aPCx using optogenetic approaches. Third, the effect of these top-down signals on the odor-evoked behavioral choice and odor-reward learning in animals needs to be clarified, since the top-down input from the frontal cortex to the primary sensory cortex has been reported to affect decision-making and learning (Banerjee et al., 2020; Liu et al., 2020; Zhang et al., 2014). Proving functional causality within the same framework will lead to a better understanding of the significance of top-down input to the sensory cortex in the whole brain and the olfactory circuits.

In conclusion, we extended the view that the aPCx processes a wide variety of odor information through distributed coding and proposed the concept that the aPCx can receive stable behavioral state signals from upstream regions while continuously updating the associations between odors and behavioral states. Our study provides a new framework for the existence of rules between the non-topographical and unstable olfactory processing of the aPCx with behavioral state signals and may serve as a basis for developing a circuit model for understanding the active bottom-up and top-down communication in the sensory cortex. Furthermore, it is possible that not only the aPCx but also other olfactory cortex subregions (Shiotani et al., 2020b, 2020a; Tanisumi et al., 2021) have their own unique top-down signal processing.

Chapter 4. Research: ventral tenia tecta (vTT) in the OC

4.1. Short summary

Based on the unique behavioral state representations in the OC (**Chapter 3**), it is assumed that there are some sources of top-down input to the OC wide area. The ventral tenia tecta (vTT) is a component of the olfactory cortex and receives both bottom-up odor and top-down signals. However, it remains unknown how the vTT neurons represent these signals during cognitive and behavioral decision processes. Using an extracellular recording, we demonstrate individual vTT neurons tune to specific time windows in the behavioral context during odor-guided goal-directed behaviors (Shiotani et al., 2020b). The vTT receives top-down projections from the medial prefrontal cortex and projects to the broad olfactory areas, suggesting that vTT acts as a hub that sends context-dependent signals to broad olfactory areas.

4.2. Introduction

The vTT is a relatively unexplored area of the olfactory cortex located in the ventromedial aspect of the olfactory peduncle. Physiological studies of the visual, auditory, and somatosensory cortices have revealed that neocortical sensory area neurons receive sensory signals from the environment, as well as top-down signals that are generated internally by higher-order cognitive and behavioral decision processes, including attention, reward-prediction, working memory, and behavioral choice processes (Allen et al., 2019; Gilbert and Sigman, 2007; Roelfsema and de Lange, 2016). In olfactory circuits, olfactory tubercle neurons encode goal-directed behaviors and exhibit enhanced odor responses when animals selectively attend to specific odors (Carlson et al., 2018; Gadziola and Wesson, 2016). Furthermore, c-Fos expression (a marker of neuronal activity) increases in different cells in the olfactory tubercle during distinct motivated behaviors in mice (Murata et al., 2015). However, the physiological and behavioral functions of the vTT are poorly understood.

To examine whether vTT neurons are modulated by cognitive and behavioral decision-making processes, we recorded neural activity of individual vTT cells during the performance of a series of odor-guided behaviors in mice. We observed that the firing of individual vTT neurons during odor-guided goal-directed behaviors was highly tuned to distinct task-elements that occurred in relation to the flow of goal-directed tasks, with each task-element occurring in a specific behavioral context. Our results indicate that vTT functions are dynamic rather than fixed, whereby changes in information processing mode occur in a context-dependent manner during a sequence of feeding and drinking behaviors.

4.3. Results: Activity of vTT neurons during the odor presentation phase of the odor-guided go/no-go task

We recorded the spiking activity of 270 vTT cells from six mice while they performed the go/no-go task (**Figures 4-1A and B**). After the mice were well trained, their behavioral accuracy remained above 80% throughout the session. The median duration of nose pokes after the onset of odor stimulation was 839 msec (interquartile range: 703-1,003 msec) in the go trials and 738 msec (interquartile range: 621-946 msec) in the no-go trials (57 sessions from six mice).

As the vTT receives direct inputs from mitral and tufted cells of the olfactory bulb, we first focused on whether vTT cells exhibited odor cue-responsive activity during odor presentation. We observed that a subset of vTT cells increased their firing rates during the odor presentation phase during both go and no-go trials (an example is shown in **Figure 4-1C**). To quantify the dependence of firing rate on the odor presentation phase, we calculated firing rate changes from baseline (pre-odor cue period, 1.2 to 1 sec before the odor port entry) in sliding bins (width, 100 msec; step, 20 msec) using a ROC analysis approach. We calculated the auROC at each time bin (spike data were aligned to the onset of odor valve opening). auROC values ranged from -1 to +1, with positive and negative values reflecting increased and decreased firing rates relative to baseline, respectively. We further determined auROC value significance using a permutation test. Using the auROC approach, we defined the odor cue-responsive population ($n = 68$ cells, 25% of the recorded cells) as cells that significantly increased their firing rates from baseline for five consecutive bins (100 msec) during the odor presentation phase (500 msec after the odor valve opening) in correct go or no-go trials. Across all the cells, many exhibited significant increases in firing rate relative to both the go and no-go odor cue presentation phases (top color maps in **Figure 4-1D**, $p < 0.01$, permutation test). No significant differences in the magnitude of these increases between the go and no-go odor cue phases at each time point were observed (bottom lines in **Figure 4-1D**, $p > 0.01$, Welch's *t* test). Changes in firing rate in individual vTT cells exhibited similar time courses for go and no-go trials. We quantified this by calculating the correlation coefficients of response profiles between correct go trials and correct no-go trials for each cell (top lines in **Figure 4-1E**). This analysis revealed that the activity of vTT cells was strongly correlated between go and no-go odor cue presentation phases, whereas different cell pairs did not exhibit this correlation (bottom lines in **Figure 4-1E**, $p < 10^{-13}$, two-sample Kolmogorov–

Smirnov test). These results suggest that individual vTT cells did not represent odor cue differences between go and no-go trials during odor presentation phases. We therefore hypothesized that firing activity mainly reflected animal behavior and was dependent on task context.

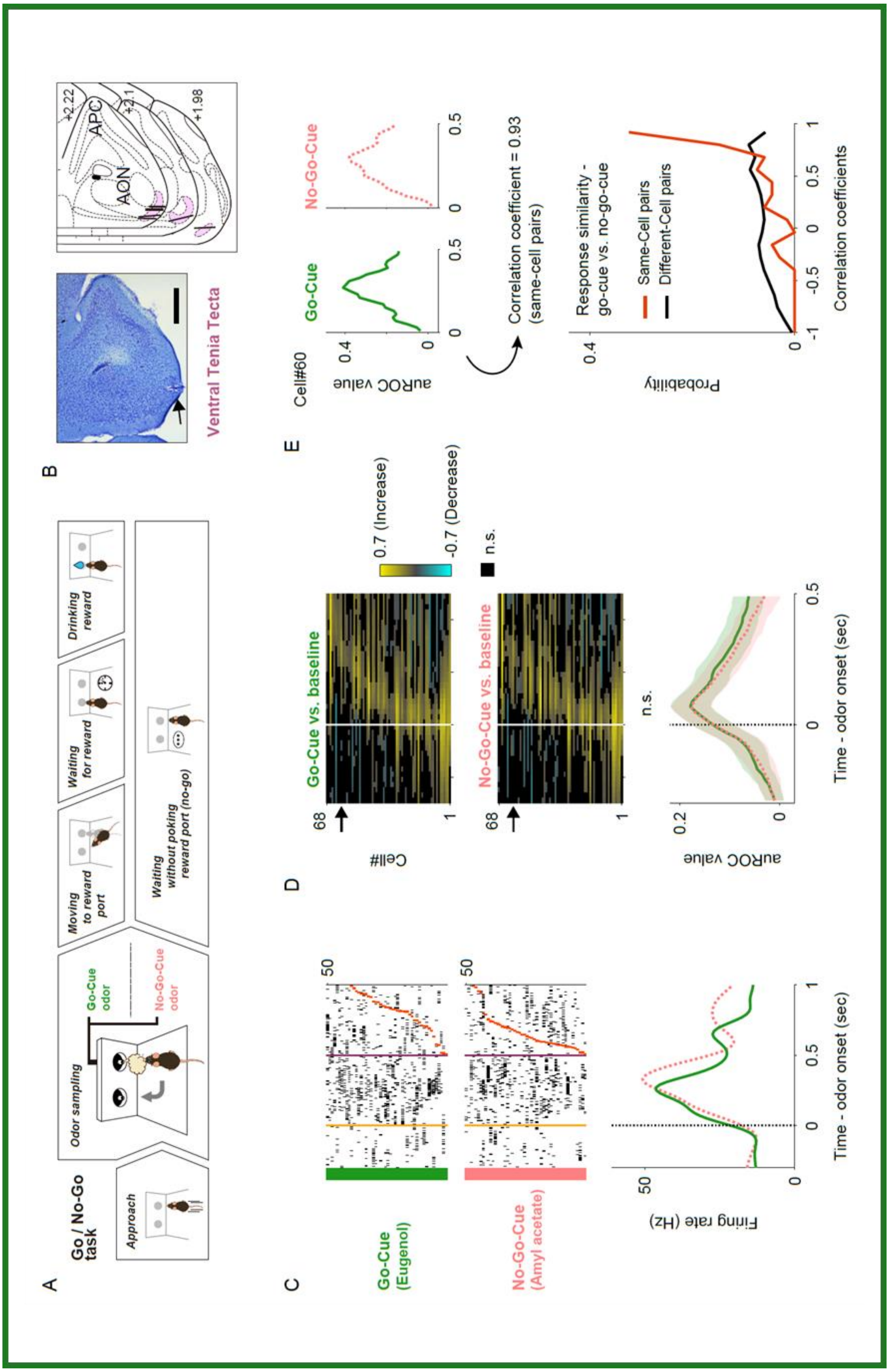
A
Go / No-Go task
Approach
Odor sampling
Go-Cue odor
No-Go-Cue odor
Moving to reward port
Waiting for reward
Drinking reward
Waiting without poking reward port (no-go)
B
Ventral Tenia Tecta
+2.22
+2.1
+1.98
APC
AON
C
Go-Cue (Eugenol)
No-Go-Cue (Amyl acetate)
50
Firing rate (Hz)
0
0.5
1
Time - odor onset (sec)
D
Go-Cue vs. baseline
No-Go-Cue vs. baseline
Cell#
68
1
0.7 (Increase)
-0.7 (Decrease)
n.s.
auROC value
0.2
0
0.5
Time - odor onset (sec)
E
Cell#60
Go-Cue
No-Go-Cue
auROC value
0.4
0
0.5
Correlation coefficient = 0.93 (same-cell pairs)
Response similarity - go-cue vs. no-go-cue
Same-Cell pairs
Different-Cell pairs
Probability
-1
-0.5
0
0.5
1
Correlation coefficients

Figure 4-1 | vTT cell activity patterns during the odor presentation phase of the odor-guided go/no-go task

(**A**) Schematic of the odor-guided go/no-go task.

(**B**) Nissl-stained frontal sections (arrow indicates recording track) and recording tracks (vertical thick lines) of the vTT in the odor-guided go/no-go task. Scale bar: 500 μm.

(**C**) Example firing patterns of vTT cells during the odor-guided go/no-go task. Purple and red ticks indicate times of odor valve closing and odor port exits, respectively.

(**D**) Upper panels: auROC values for cells with significantly higher firing rates than baseline (n = 68 cells) during the odor presentation phase (upper, go trials; lower, no-go trials). Each row corresponds to one cell, with cells in both graphs presented in the same order. auROC values (aligned by odor valve opening) were calculated by comparing odor cue presentation and baseline in sliding bins. Cells were sorted by peak value times of auROC values calculated by comparing go odor cue presentation and baseline for each cell. Color scale shows significant auROC values ($p<0.01$, permutation test). Black boxes indicate bins with non-significant auROC values ($p>0.01$, permutation test). Arrows indicate the same cell as that in (**C**). Lower panel: mean cell auROC values. Green line indicates go odor cue presentation versus baseline; pink dashed line indicates no-go odor cue presentation versus baseline. Shaded areas represent 95% confidence intervals.

(**E**) Neural response similarity measures between go and no-go odor cue presentation. Upper panel: examples of auROC values during the go/no-go odor cue presentation phase for one cell and the correlation coefficient of auROC values during the go/no-go-cue odor presentation phase. Lower panel: comparison of the correlation coefficients and cell-shuffled data, calculated for different pairs of cells.

4.4. Results: Behavior-specific activity of vTT cells in the odor-guided go/no-go task

Many vTT cells exhibited an increase in firing rate during specific behaviors over the course of the odor-guided go/no-go task. Time intervals between behavioral events (the time from odor valve opening until the mouse withdrew its snout from the odor port, and the time from odor port withdrawal until reward port entry) also varied across trials. To develop an overall firing profile accounting for this variability, we created EASHs (Ito and Doya, 2015). An EASH was derived by linearly scaling time intervals between behavioral events in each trial and the median interval for all trials. The EASHs clearly demonstrated that individual vTT cells were activated during different behavioral epochs (between-event intervals), such as when mice were poking the odor port in the approach epoch (plots in bottom left, **Figure 4-2A**) and during the odor-sampling epoch (plots second from the bottom left, **Figure 4-2A**).

To quantify neural activity across behavioral epochs during the go trials, we calculated changes in event-aligned firing rates from baseline (pre-odor cue period, 1.2 to 1 sec before odor port entry) in sliding bins (width, 100 msec; step, 20 msec) using ROC analyses. Across the population, almost all vTT cells exhibited a significant increase in firing rates during a specific behavior in each epoch (right color map in **Figure 4-2A**). Furthermore, individual vTT cells exhibited a significant decrease in firing rates in certain epochs. These results were independent of the size of the window in which auROC values were calculated. To evaluate the relationships between epoch-specific firing rates, vTT cells were classified into five groups based on their tuning peak time with reference to the five go trial behavioral epochs. For each cell group, we calculated relative distributions of significant responses for each bin, according to significantly increased or decreased changes in firing rate throughout the tasks (**Figure 4-2B**). Of vTT cells, 7% exhibited tuning peak times within the time window of the approach epoch, indicating a significantly greater probability of exhibiting an increase in firing rate during the approach epoch; 24% had tuning peak times during the odor-sampling epoch, indicating that the firing rates of these cells were increased during the odor-sampling epoch; 23% and 11% had tuning peak times during the moving and waiting epochs, respectively, indicating that these cells were tuned to each epoch; and 15% had tuning peak times during the drinking epoch, indicating that they were tuned to the drinking epoch. Moreover, we observed that these classified cells tended to decrease their activity during other behavioral epochs, suggesting that individual vTT cells exhibit distinct tuning profiles for specific goal-directed behaviors.

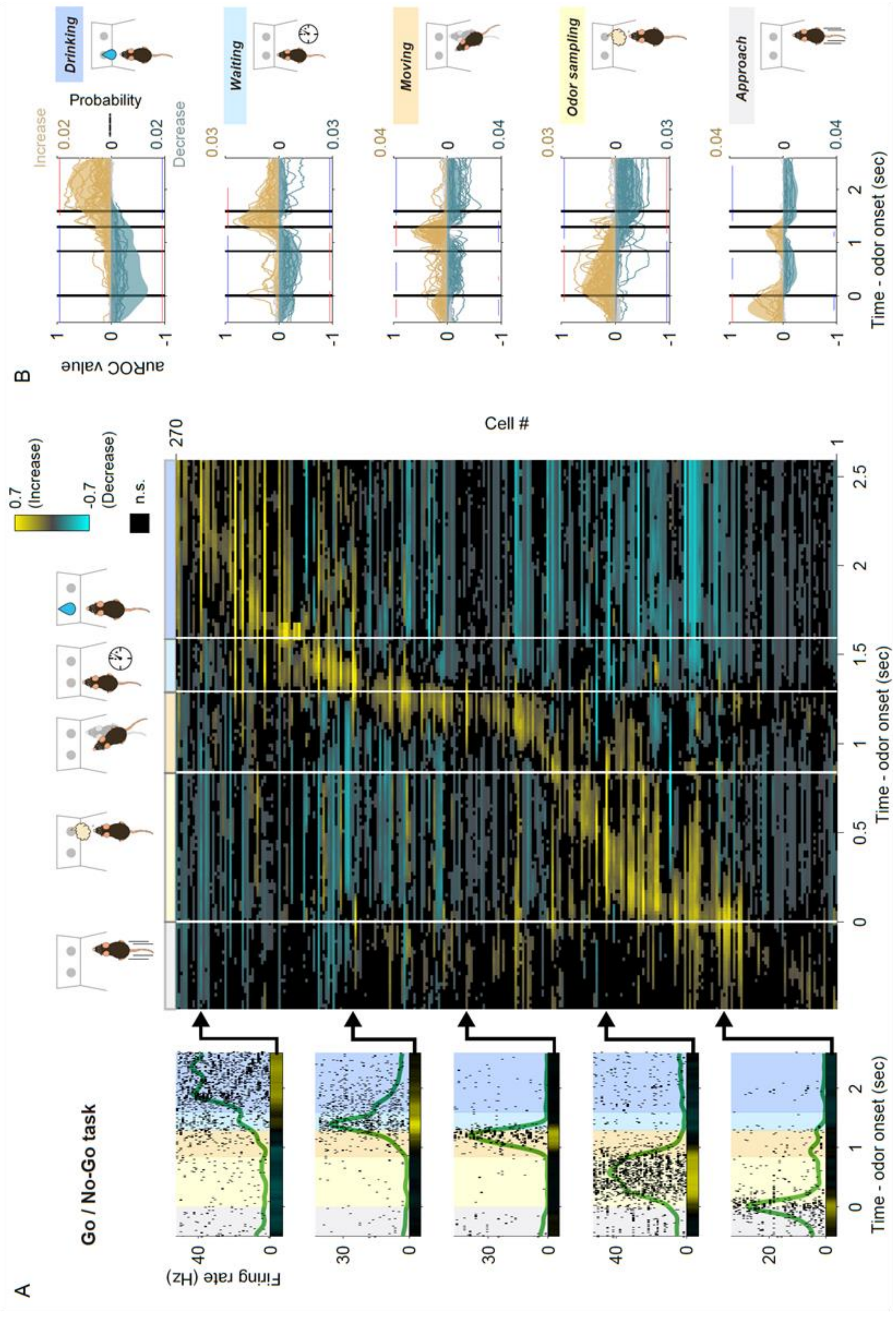
A
Go / No-Go task
Firing rate (Hz)
40
30
20
0
Time - odor onset (sec)
0
1
2
0.7
(Increase)
-0.7
(Decrease)
n.s.
270
Cell #
1
0
0.5
1
1.5
2
2.5
Time - odor onset (sec)
B
auROC value
1
0
-1
Increase
Decrease
Probability
0.02
0.03
0.04
Drinking
Waiting
Moving
Odor sampling
Approach
Time - odor onset (sec)

Figure 4-2 | Tuning of vTT cells to distinct behaviors in the odor-guided go/no-go task

(**A**) Left panel: examples of event-aligned spike data for five representative cells tuned to specific behaviors. Gray shading indicates the approach epoch (500 ms before odor port entry), yellow shading indicates the odor-sampling epoch (from entry into the odor port to exiting the odor port), orange shading indicates the moving epoch (from exiting the odor port to entry into the water port), light blue shading indicates the waiting epoch (water reward delay, 300 ms before water valve was turned on), blue shading indicates the drinking epoch (1000 ms after the water valve was turned on). Right panel: auROC values were calculated from event-aligned spike data for all cells, sorted by the peak time for auROC values. Each row corresponds to one cell. auROC values were calculated by comparing go correct trials to baseline in sliding bins. Vertical white lines indicate transitions between behavioral epochs, including odor port entry (corresponding to odor valve opening), odor port exit, water port entry, and water valve opening. The color scale for this figure is the same as that used in **Figure 4-1D**, with positive and negative values reflecting increased and decreased firing rates relative to baseline, respectively. Right top panel: Schematics of the approach (gray bar), odor-sampling (yellow bar), moving (orange bar), waiting (light-blue bar), and drinking (blue bar) behaviors. As behavioral epoch durations varied for each trial, the median duration of the epoch was calculated. Spike timing during each epoch and for each trial was linearly transformed to correspond with the median duration of each behavioral epoch.

(**B**) Relative distribution of significant auROC values ($p<0.01$, permutation test) per cell group tuned to a specific behavioral epoch in the odor-guided go/no-go task, and the schematics of the approach, odor-sampling, moving, waiting, and drinking behaviors. Cell groups were tuned to the approach, odor-sampling, moving, waiting, and drinking epochs (from bottom to top graphs). Each line corresponds to one cell (left axes, auROC values). Yellow and blue indicate a significant increase and decrease from baseline, respectively. Gray indicates neither a significant increase nor decrease. Shaded regions show the relative distributions of significant auROC valves (right axes, probability). Red dots indicate that a time bin contained more cells with significant responses than in the distribution of 1000 resampling datasets. Blue dots indicate that a time bin contained fewer cells with significant responses than in the distribution of 1000 resampling datasets. Vertical black lines indicate the timing of odor port entry (corresponding to odor valve opening), odor port exit, water port entry, and water valve opening. Note that each cell group exhibited an excitatory response to a specific behavioral epoch, with suppressed responses relative to other epochs.

4.5. Results: Behavioral context-dependent activity of vTT cells

We observed that many vTT cells tended to increase their firing rates before the most preferred behavioral epochs, and some cells maintained their increased firing rate after the epoch (**Figure 4-2B**). We therefore hypothesized that individual vTT cell firing was tuned to a specific behavioral context and was thus dependent on specific task-elements during task progression rather than on specific behaviors. If this were true, the response patterns of vTT cells would change in a different context, even for the same behavior. We assessed nose poke behaviors during the odor-sampling epoch of the odor-guided go/no-go task and observed that a subset of cells exhibited differences in firing rates between the go and no-go trials just before the animals exited the odor port, despite involving the same nose-poking behavior. We quantified this by calculating go-cue versus no-go-cue trial preference using ROC analyses with real-time data. When the differences in firing rate were aligned to odor port exit times, we observed that more cells had differences in firing rate between the go and no-go trials before the animal exited from the odor port compared to that during the odor presentation phase (**Figure 4-3A**). A subset of cells with tuning peak times not during the odor-sampling epoch also exhibited differences in firing rate just before odor port exit times.

To examine whether the population activity of vTT cells could account for behavioral accuracy, we performed a decoding analysis to determine whether the firing rates of vTT cell populations could be used to classify each individual trial as go or no-go. We used SVMs with linear kernels as a decoder (Cury and Uchida, 2010; Miura et al., 2012). Analyses of the decoding time course based on all 270 cells using a sliding time window revealed that decoding accuracy was maintained at chance levels during odor presentations and subsequently increased close to the level achieved during behavioral accuracy just before odor port exit (**Figure 4-3B**). These results suggest that vTT cells were tuned to task elements in a particular behavioral context during goal-directed behaviors.

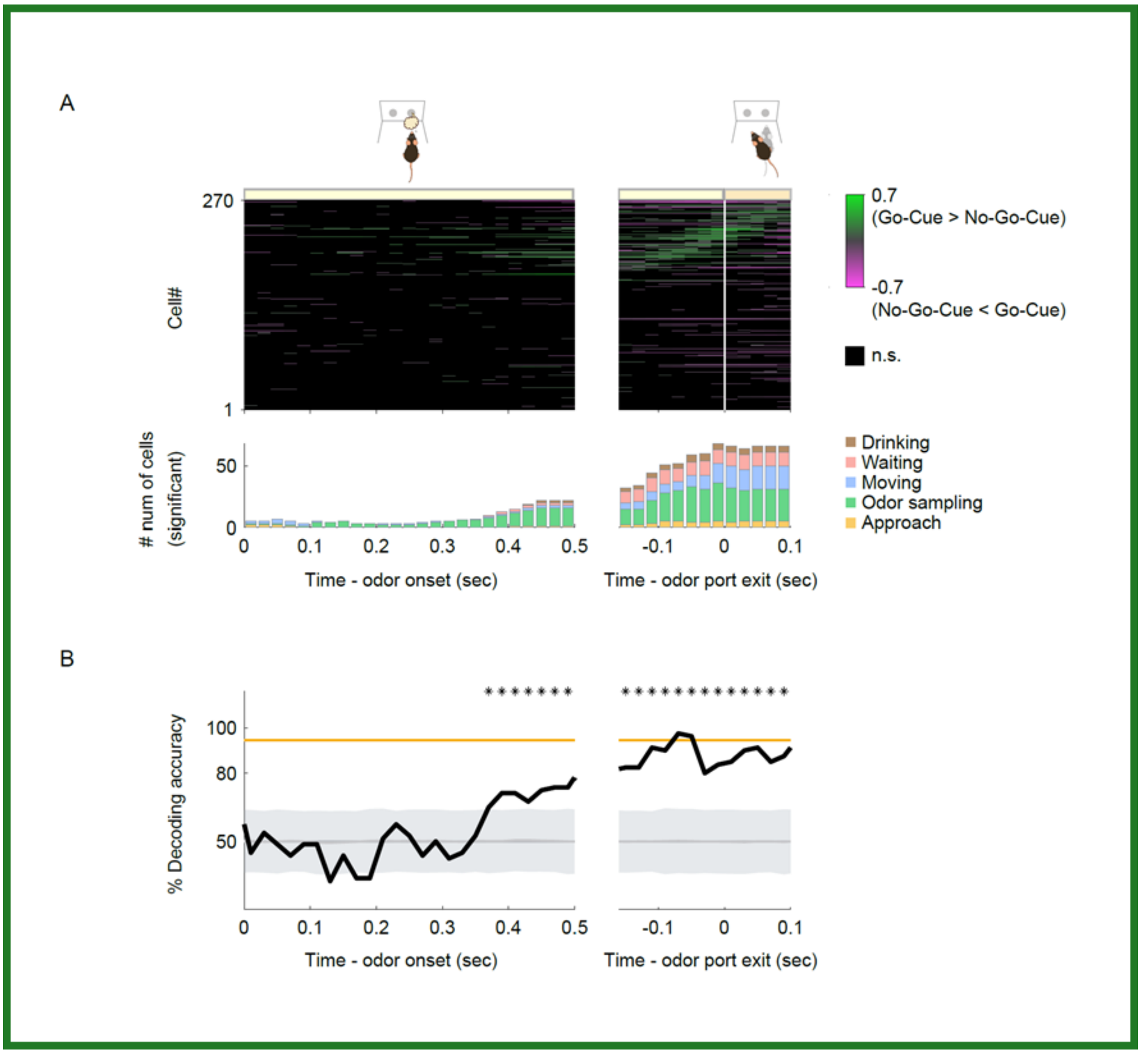

Figure 4-3 | Behavioral context-specific activity of vTT cells

(**A**) Upper panel: auROC values for all cells around the odor sampling epoch in the odor- guided go/no-go task. Each row corresponds to one cell. auROC values (left, aligned to the odor valve opening; right, aligned to the odor port exit) were calculated for correct go trials versus correct no-go trials in sliding bins. These values were sorted based on the time of peak auROC values in the right graph. The color scale indicates significant auROC values (p<0.01, permutation test). The black boxes indicate bins with non-significant auROC values. Lower panel: the number of cells that exhibited significant auROC values (p<0.01, permutation test) for each time bin (orange, cell group tuned to the approach epoch; green, odor sampling epoch; blue, moving epoch; red, waiting epoch; brown, drinking epoch). (**B**) The time course of odor decoding accuracy in the odor-guided go/no-go task. A vector consisting of instantaneous spike counts for 270 neurons in a sliding window was used as input for the classifier. Training of the classifier and testing were performed at every time point. The orange line indicates the level of behavioral performance. The gray line and shaded area indicate the mean ±2 SD of control decoding accuracies calculated from 1000 trial-label-shuffled datasets. Top asterisks indicate accuracies greater than the mean + 2SD.

4.6. Results: Cell types and connectivity patterns of vTT cells

Although many neurons in layer II of the vTT comprise pyramidal cells, the vTT also contains additional cell types (Haberly and Price, 1978; Shepherd, 2004). To examine the distribution of glutamatergic and GABAergic cells in the vTT, we performed in situ hybridization to measure vesicular glutamate transporter 1 (VGluT1) and glutamic acid decarboxylase (GAD) 67 and GAD65 mRNA (Slc17a7 and Gad1/2 mRNAs, respectively) in the vTT (**Figure 4-4A and 4-4B**). Approximately 86% and 8% of vTT cells were Slc17a7-positive and Gad1/2-positive, respectively, suggesting that the principal neurons of the vTT are glutamatergic.

It has previously been reported that the vTT has reciprocal connections with the olfactory bulb (OB), anterior piriform cortex (aPCx), and posterior piriform cortex (pPCx) (Igarashi et al., 2012; Luskin and Price, 1983a, 1983b). In addition, the deep layers of the vTT receive top-down inputs from the medial prefrontal cortex (mPFC) (Hoover and Vertes, 2011). To further examine cortical areas projecting to the vTT, we injected a retrograde tracer, CTB conjugated with Alexa 555, into the mouse vTT (**Figure 4-4C**). A number of retrogradely labelled (CTB-positive) cell bodies were identified in the OB, aPCx, pPCx, and mPFC. In contrast, CTB-positive cell bodies were rarely observed in the anterior olfactory nucleus (AON), which is located just dorsal to the vTT

(**Figure 4-4D**). To examine cortical regions that received axonal projections from vTT cells, we injected CTB into the mPFC, OB, AON, olfactory tubercle (OT), aPCx, and pPCx. We then quantified retrogradely labelled CTB-positive cells in the vTT (**Figures 4-4E and 4-4F**). Many retrogradely labeled vTT cells were observed in mice that received CTB injections in the OB, AON, and aPCx. In contrast, only a small number of retrogradely labeled vTT cells were observed in mice that received CTB injections in the OT and pPCx. Furthermore, retrogradely labeled cells were scarce in the vTT following injections of CTB into the mPFC. These results suggest that, in addition to dense reciprocal connections with the OB, the vTT projects to the AON and aPCx, and receives top-down projections from the aPCx, pPCx, and mPFC (**Figure 4-4G**).

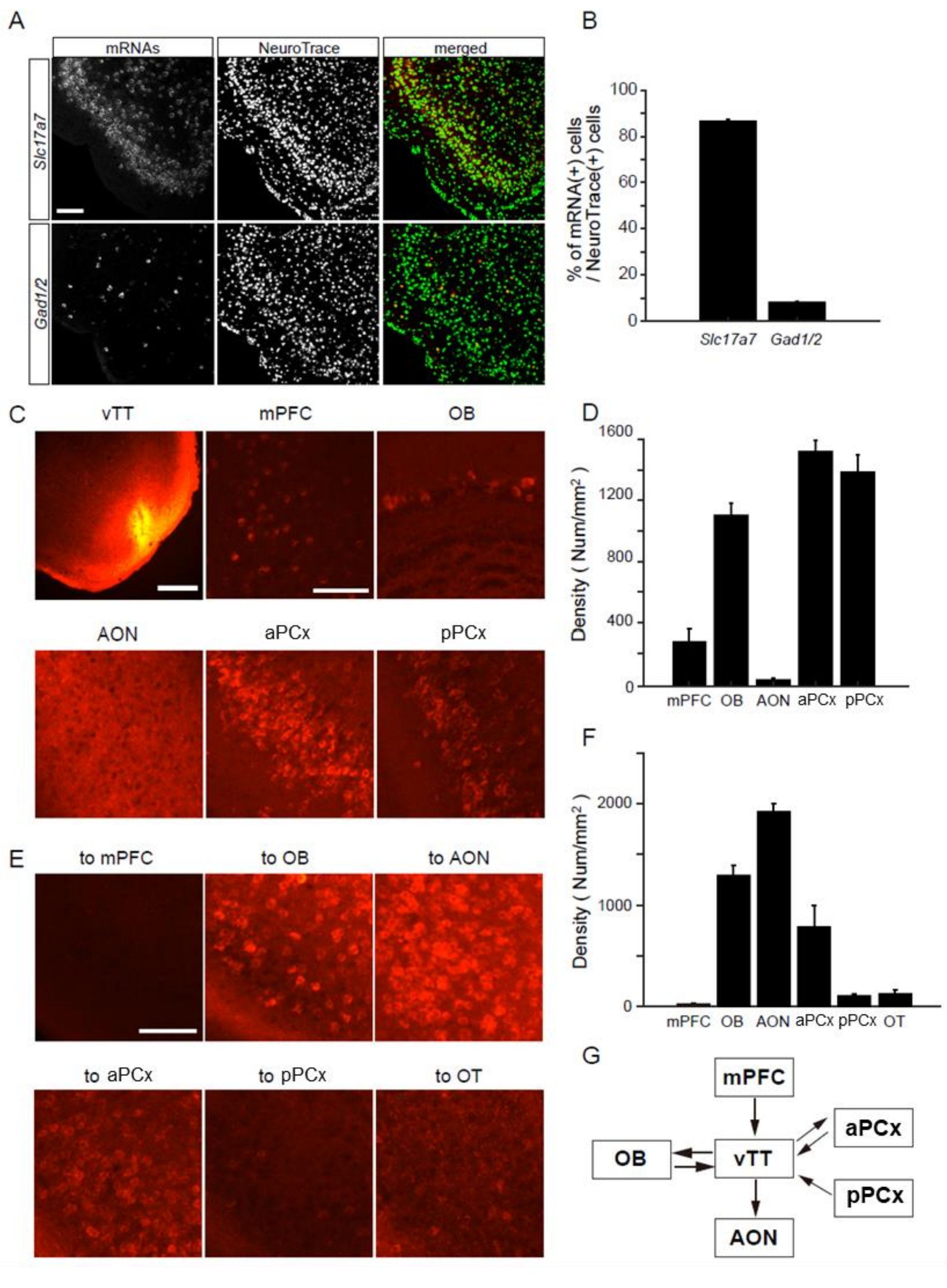
A
mRNAs
NeuroTrace
merged
Slc17a7
Gad1/2
B
% of mRNA(+) cells / NeuroTrace(+) cells
100
80
60
40
20
0
Slc17a7
Gad1/2
C
vTT
mPFC
OB
AON
aPCx
pPCx
D
Density (Num/mm^2)
1600
1200
800
400
0
mPFC
OB
AON
aPCx
pPCx
E
to mPFC
to OB
to AON
to aPCx
to pPCx
to OT
F
Density (Num/mm^2)
2000
1000
0
mPFC
OB
AON
aPCx
pPCx
OT
G
mPFC
aPCx
OB
vTT
pPCx
AON

Figure 4-4 | Cell types and connectivity patterns of vTT cells

(**A**) In situ hybridization of Slc17a7 (upper panels) and Gad1/2 (lower panels) mRNAs with Neurotrace staining of vTT cells. Scale bar, 100 μm.

(**B**) Average percentages of Slc17a7-positive cells (left column) and Gad1/2-positive cells (right column) among Neurotrace-positive cells in the vTT (n = 3 mice). Error bars indicate SEM.

(**C**) Upper left: Coronal section of the vTT after injection of Alexa 555-conjugated cholera toxin subunit B (CTB, red). Scale bar, 500 μm. The five other panels show CTB-labeled cells after CTB injections in the vTT. mPFC, medial prefrontal cortex; OB, olfactory bulb; AON, anterior olfactory nucleus; aPCx, anterior piriform cortex; pPCx, posterior piriform cortex. Scale bar, 100 μm.

(**D**) Average density of CTB-labeled cell bodies in each area (mPFC, n = 5 from three mice; OB, n = 5 from three mice; AON, n = 3 from two mice; aPCx, n = 5 from three mice; pPCx, n = 5 from three mice). Error bars indicate SEM.

(**E**) CTB-labeled vTT cells after injection of CTB into the mPFC (upper left), OB (upper middle), AON (upper right), olfactory tubercle (OT, lower left), APC (lower middle), and pPCx (lower right). Scale bar, 100 μm.

(**F**) Average density of retrogradely labeled CTB-positive cells in the vTT (n = 3 from two mice). Error bars indicate SEM.

(**G**) Schematic diagram of vTT connectivity patterns. Arrows indicate axonal projections.

4.7. Results: mPFC-to-vTT top-down input potentially shares behavioral state signals to the olfactory cortex

As described above, we anatomically elicited the possibility that the mPFC-to-vTT-to-olfactory cortex pathway may be important as a candidate for the top-down input to the olfactory cortex. To test this hypothesis, we expressed inhibitory archaerhodopsin 3.0 (Arch3.0) in the mPFC and recorded from vTT neurons with and without optogenetic inactivation of mPFC axons while head-fixed mice conducted the odor-outcome association task. Without mPFC-to-vTT inputs, the vTT state representations were degraded and less integrated (**Figure 4-5**). Although these results are still preliminary and require data from enough samples including control conditions in the future, our data suggest that vTT acts as a hub that sends context-dependent signals from the mPFC to broad olfactory areas.

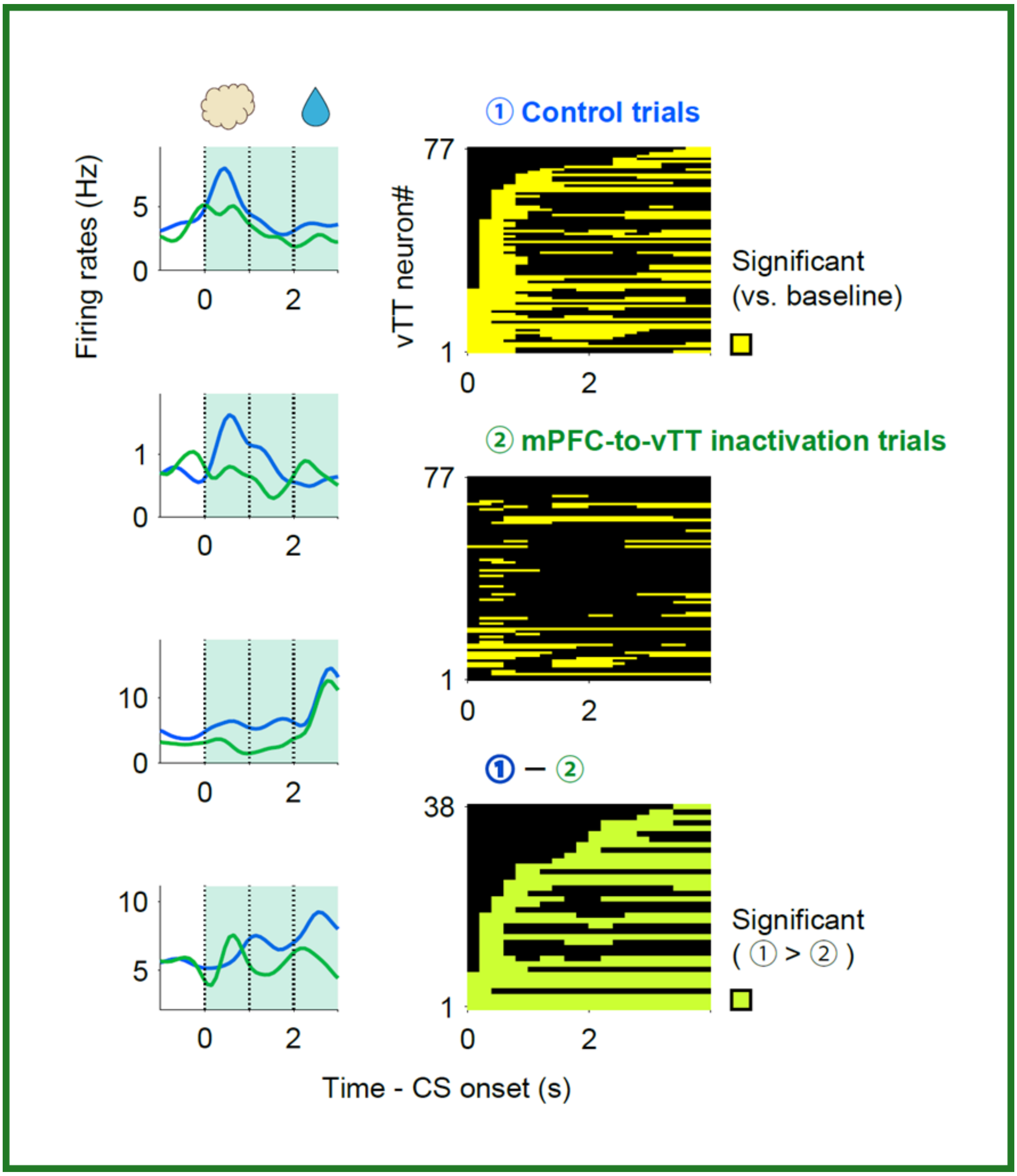

Figure 4-5 | mPFC-to-vTT top-down input potentially shares behavioral state signals to the olfactory cortex

Left panel: Examples of spike data for four representative cells tuned to specific behaviors. Blue line indicates odor-reward trials (control trials); green line indicates odor-reward trials with the optogenetic inactivation. Light green shading indicates the optogenetic inactivation periods. Right panel: Colored boxes indicate bins with significant auROC values ($p>0.01$, permutation test). auROC values were calculated by comparing odor-reward trials and baseline in sliding bins.

4.8. Discussion

In the present study, we reported seminal recordings of neuronal activity in the vTT in freely behaving mice during the performance of odor-guided behaviors. We characterized the neural activities of the vTT cells in mice performing the odor-guided goal-directed behavioral task. Our results demonstrated characteristic tuning of individual vTT cells to specific temporal windows in the behavioral context of goal-directed tasks.

In the odor-guided go/no-go task, 25% of vTT cells exhibited increased firing during the learned odor presentation phases (**Figure 4-1**). Although many of these vTT cells exhibited peak firing ~100 msec after odor onset, they did not encode learned odor differences during the odor presentation phases (**Figure 4-1E**). Firing rate differences in a subset of cells emerged just before the odor port exit during which mice performed behavioral choices (**Figure 4-3**). These features resembled the response pattern for learned odor-guided tasks observed in the piriform cortex (Gadziola et al., 2020; Gire et al., 2013). However, many vTT cells increased their firing rate before the odor presentation (**Figures 4-1D and 4-2B**), and individual vTT cells exhibited a particular tuning pattern characterized by peak tuning and tuning duration. Therefore, we hypothesized that the firing activity of vTT cells mainly reflected animal behavior and was dependent on task context.

During the odor-guided go/no-go task used here (**Figure 4-2**), vTT cells exhibited a specific firing rate tuning to each behavioral epoch (e.g., moving to the odor port, odor-sampling in the odor port, moving to the water reward port, waiting for the reward, and obtaining the water reward) of the go trials. Furthermore, these cells tended to suppress their firing activity during epochs other than the most preferred epoch. Collectively, these results indicate that each vTT cell has a unique behavior- and context-dependent preference, demonstrated by tuning peak time and tuning duration. These properties of vTT cells may contribute to the representation of a series of specific behavioral context information (i.e., an episode) during odor-guided behaviors in the vTT. As vTT cells send their axons to other olfactory cortex areas such as the AON and piriform cortex (**Figure 4-4**) (Luskin and Price, 1983a, 1983b), we speculate that the vTT may provide information to widespread olfactory areas regarding moment-to-moment changes in behaviors within certain behavioral contexts. Indeed, context-dependent modulation of neural activity is observed in mitral cells in the OB, an area that receives direct inputs from the vTT during the performance of odor-reinforcer association learning (Kay and Laurent, 1999).

We conjecture that behavioral context-dependent inputs from other higher-brain areas may contribute to the context-dependent activity of vTT cells because it is difficult to explain how behavioral context-dependent activity may otherwise be induced by bottom-up olfactory sensory input alone. The vTT receives direct top-down projections from the mPFC and indirect projections from other olfactory cortical areas (**Figure 4-4**) (Luskin and Price, 1983a). Note that mPFC neurons are implicated in contextual encoding when animals move between different environmental contexts (Hyman et al., 2012) and preferentially fire at a specific position in the trajectory of a maze during a working memory task involving odor place-matching (Fujisawa et al., 2008). Along with the evidence presented here, these findings suggest that context-specific activity of the mPFC may contribute to the generation of context-dependent activity in the vTT. In addition, Allen et al. recently reported that odor cue-induced reward-predicting responses were not restricted to the olfactory cortex but occurred throughout the brain, including sensory, motor, and prefrontal cortices, as well as subcortical regions (Allen et al., 2019). This suggests that context-dependent cells are located throughout the brain, and their activity may drive specific information processing modes in the brain. In this regard, the vTT may play an important role in entraining specific information processing modes in olfactory areas by acting as a hub, amplifier, or rectifier that sends context-dependent signals from the mPFC to broad olfactory areas. Indeed, our preliminary data (**Figure 4-5**) support this hypothesis. The direction of future research is to examine how the top-down input from the frontal cortex to the olfactory cortex is distributed to each cortex subregion and how it is involved in unique information processing to create an overall map of the bottom-up and top-down communication circuits.

Chapter 5. Research: nucleus of the lateral olfactory tract (NLOT) in the OC

5.1. Short summary

To explore how the top-down inputs to the OC suggested in the above chapters are distributed to the OC subareas, it is necessary to investigate the activity of subareas with unique anatomical backgrounds. The nucleus of the lateral olfactory tract (NLOT) is not only a part of the olfactory cortex, but also a part of the cortical amygdala. Using an extracellular recording, we demonstrate NLOT neurons exhibit context-based odor-outcome associations, suggesting they play an important role in the translation from context-based odor information to appropriate behavior (Tanisumi et al., 2021).

5.2. Introduction

The NLOT is part of the olfactory cortex that receives direct sensory inputs from the olfactory bulb and the olfactory cortex, including the piriform cortex shown by neural tracing studies (Luskin and Price, 1983a; Price, 1973). Alternately, it also receives projections from the anterior amygdaloid area, anterior cortical and posterolateral cortical amygdaloid nuclei, and amygdalo-piriform transition area, and forms part of the olfactory amygdala. While some authors have considered the NLOT to be a component of the olfactory cortex (Price, 1973; Swanson and Petrovich, 1998), others have regarded it as a component of the cortical amygdala areas that plays a critical role in generating odor-driven behaviors. The NLOT not only has a bi-directional connection with the olfactory bulb and piriform cortex, but also strongly innervates the basolateral amygdala and ventral striatum shown by neural tracing studies (Luskin and Price, 1983a; Price, 1973; Santiago and Shammah-Lagnado, 2004). Due to its anatomical features, it is possible that the NLOT is involved in odor-evoked motivational behaviors. In addition to this anatomical evidence, a recent study (Vaz et al., 2017) has shown functional evidence that NLOT integrity is required for normal functioning of the olfactory system. Researchers have conducted a series of behavioral tests using rats with bilateral excitotoxic lesions of the NLOT. The NLOT-lesioned rats exhibited severe olfactory deficits with an inability to detect and discriminate between odors.

Despite the accumulation of knowledge, there are no reports of *in vivo* recording of neuronal activity in the NLOT. Therefore, the electrophysiological features of NLOT neurons on odor-evoked motivational behavior have not been clarified. The purpose of our study was to investigate how neural activity is modulated by motivational processes that occur during various behavioral states in a goal-directed task. Here, we recorded the neural spike activities in the NLOT of freely moving mice performing an odor-guided go/no-go task. We observed that the majority of NLOT neurons exhibited go-cue excitation and no-go-cue suppression responses triggered by an odor onset. The bi-directional cue encoding strongly contributed to the NLOT neuron population dynamics before executing cue-odor-evoked behaviors; additionally, the go-cue responsive neurons encoded a reward drinking state, indicating context-based odor-outcome associations. Our results suggest that the NLOT is critical for encoding context-based cue-outcome signals and may play an important role in the translation of odor stimulus information to appropriate behavior.

5.3. Results: *In vivo* recording in the NLOT and the odor-guided go/no-go tasks

We obtained recordings from 365 well-isolated neurons in the NLOT of four mice performing odor-guided go/no-go tasks (**Figures 5-1A and 5-1B**). Briefly, the go trial required the mice to first sample a go-cue odor stimulus presented at an odor port and then to move to a reward port to obtain a water reward. Conversely, the no-go trial required the mice to first sample a no-go-cue odor stimulus presented at the odor port and then to stay near it to wait for the next trial. It is important to note that the mice were required to keep their nose inserted into the odor port during odor presentation (500 ms).

After the mice were well-trained, their behavioral accuracy remained >80% throughout the session. For all mice, the median of the odor-sampling epoch (the time from odor valve opening until the withdrawal of the snout by the mouse from the odor port) was 788 ms (interquartile range: 669–962 ms) in the go trials, and 642 ms (interquartile range: 562–798 ms) in the no-go trials (44 sessions from four mice).

However, it is possible that these reaction times reflect the time lag between the start of odor stimulation and the arrival of the odor molecules to the mouse's nose. We, therefore, examined how quickly the mouse decides on its behavior by shortening the duration of odor presentation and measuring the reaction time (from the onset of odor presentation to the timing of nose withdrawal) (**Figure 5-1C**). When the duration of odor presentation was shortened without the forced nose-poking during odor presentations, the mice showed shorter reaction times; however, the behavioral accuracy remained >80%. These results indicate that the arrival of the odors was at least within 400 ms after the opening of the odor valve, and the mice could make decisions within the odor presentation. In the following sections, we describe our analyses of the neural activity recorded during odor-sampling and the following odor-guided behaviors.

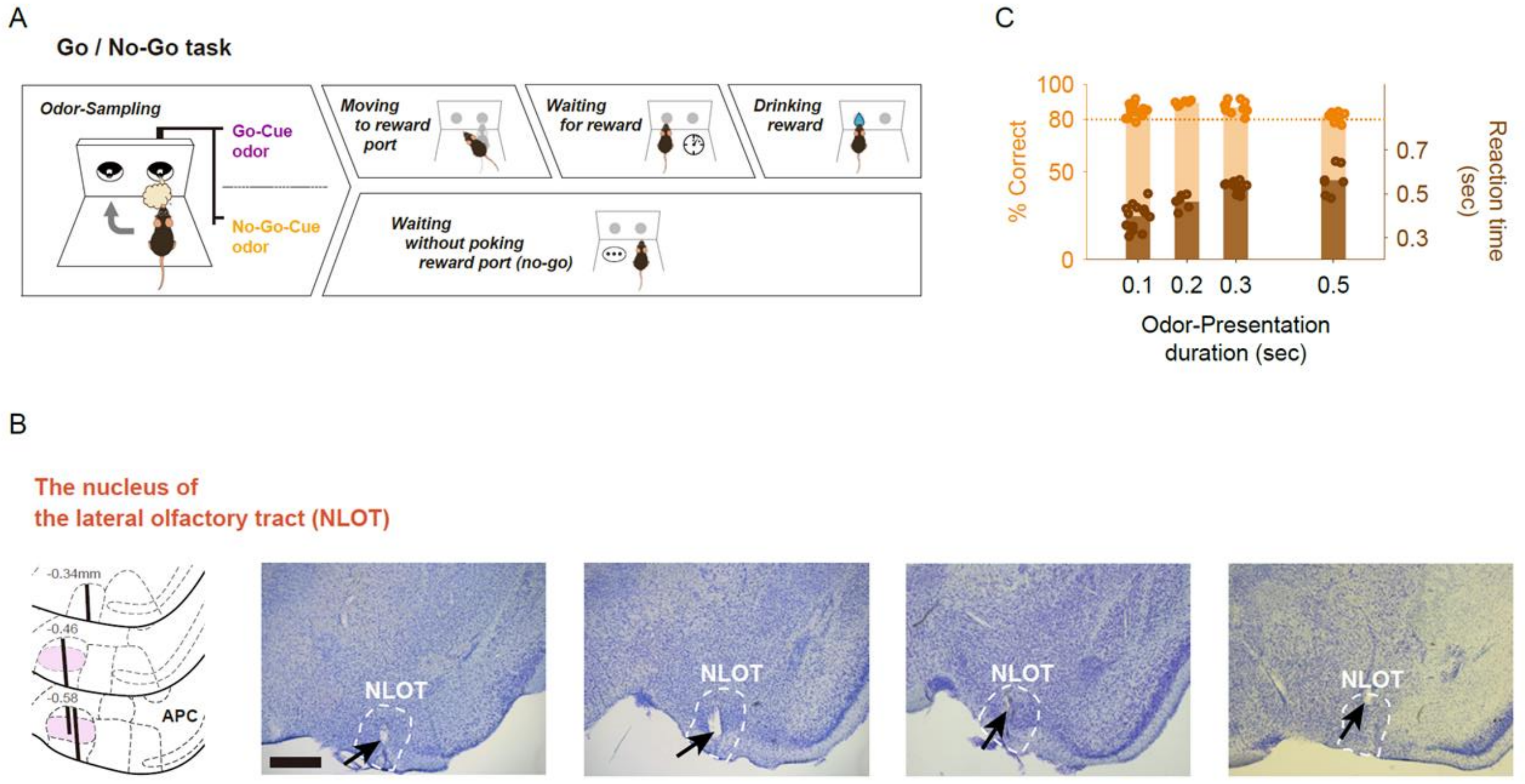
A
Go / No-Go task
Odor-Sampling
Go-Cue odor
No-Go-Cue odor
Moving to reward port
Waiting for reward
Drinking reward
Waiting without poking reward port (no-go)
C
% Correct
100
80
50
0
Reaction time (sec)
0.7
0.5
0.3
0.1
0.2
0.3
0.5
Odor-Presentation duration (sec)
B
The nucleus of the lateral olfactory tract (NLOT)
-0.34mm
-0.46
-0.58
APC
NLOT
NLOT
NLOT
NLOT

Figure 5-1 | Odor-guided go/no-go task and the NLOT

(**A**) Time course of the odor-guided go/no-go task.

(**B**) Nissl-stained frontal section (arrows indicate tips of the tetrodes) and recording tracks (vertical thick lines) of the NLOT. Scale bar, 500 μm.

(**C**) The reaction times (from the onset of odor presentation to the timing of nose withdrawal, right axis, brown) in the odor-guided go/no-go tasks without keeping the mice's nose inserted into the odor port. To test the time lag between the start of odor stimulation and the arrival of the odor molecules to the mouse's nose, we verified odor presentation durations of 100, 200, 300, and 500 ms in each session. When the duration of odor presentation was shortened, the mice showed a shorter reaction; however, the behavioral accuracy remained >80% (left axis, orange), indicating that the arrival of the odors was within 400 ms after odor valve opening, and that the mice could make decisions within the period.

5.4. Results: Five-type classification of NLOT neurons based on odor-sampling epoch response

As the NLOT receives direct inputs from the mitral cells of the olfactory bulb, we first focused on the neural activity during the odor-sampling epoch. We observed that the firing rates of the NLOT neurons increased or decreased during the odor-sampling epoch. For a large subset of neurons, these firing rate changes depended on whether the presented odor was a go-cue or no-go-cue (examples shown in **Figure 5-2**, left). To quantify the dependence of the firing rate on cue odor presentation, we used a ROC analysis approach. We calculated the firing rate changes from baseline (1,000-0 ms before the end of the inter-trial interval) during the odor-sampling epoch. Across the population, 73.2% of the NLOT neurons exhibited significant responses to at least one cue odor presentation ($p < 0.01$, permutation test). In this cue odor selective population, we also calculated the preference for go-cue and no-go-cue odor presentation. We observed that 53.2% of the population showed a significant go-cue odor preference, whereas 7.9% showed a significant no-go-cue odor preference ($p < 0.01$, permutation test). The other population exhibited increased or decreased responses to both go-cue and no-go-cue odor presentations. Thus, most of the NLOT neurons showed a wide variety of firing rate changes during an odor-sampling epoch.

Based on these response profiles of the odor-sampling epoch, we classified the NLOT neurons into five response types (**Figure 5-2**). The first neuron group (type I, 38.9% of all neurons) exhibited significant preference for the presented go-cue odor; we will refer to these as “go-cue responsive neurons” (purple pie chart in **Figure 5-2**). The second neuron group (type II, 5.8% of all neurons) exhibited significant preference for the presented no-go-cue odor; we will refer to these as “no-go-cue responsive neurons” (orange pie chart in **Figure 5-2**). Two other neuron groups (type III and IV, 11.5% and 17.0% of all neurons, respectively) showed significant excitatory and suppressed responses, respectively, for both presented cue odors without preference for a particular cue odor; we will refer to these as “cue excitatory neurons” (pink pie chart in **Figure 5-2**) and “cue suppressed neurons” (light blue pie chart in **Figure 5-2**), respectively. The remaining neuron group (type V, 26.8% of all neurons) did not show significant responses for either presented cue odors; we will refer to these as “cue non-responsive neurons” (gray pie chart in **Figure 5-2**). This classification demonstrated the diverse cue encoding patterns in the NLOT, suggesting that the NLOT neurons did not represent a particular odorant profile from the olfactory bulb; instead, they represented the complex and diverse odor information leading to odor-guided behaviors.

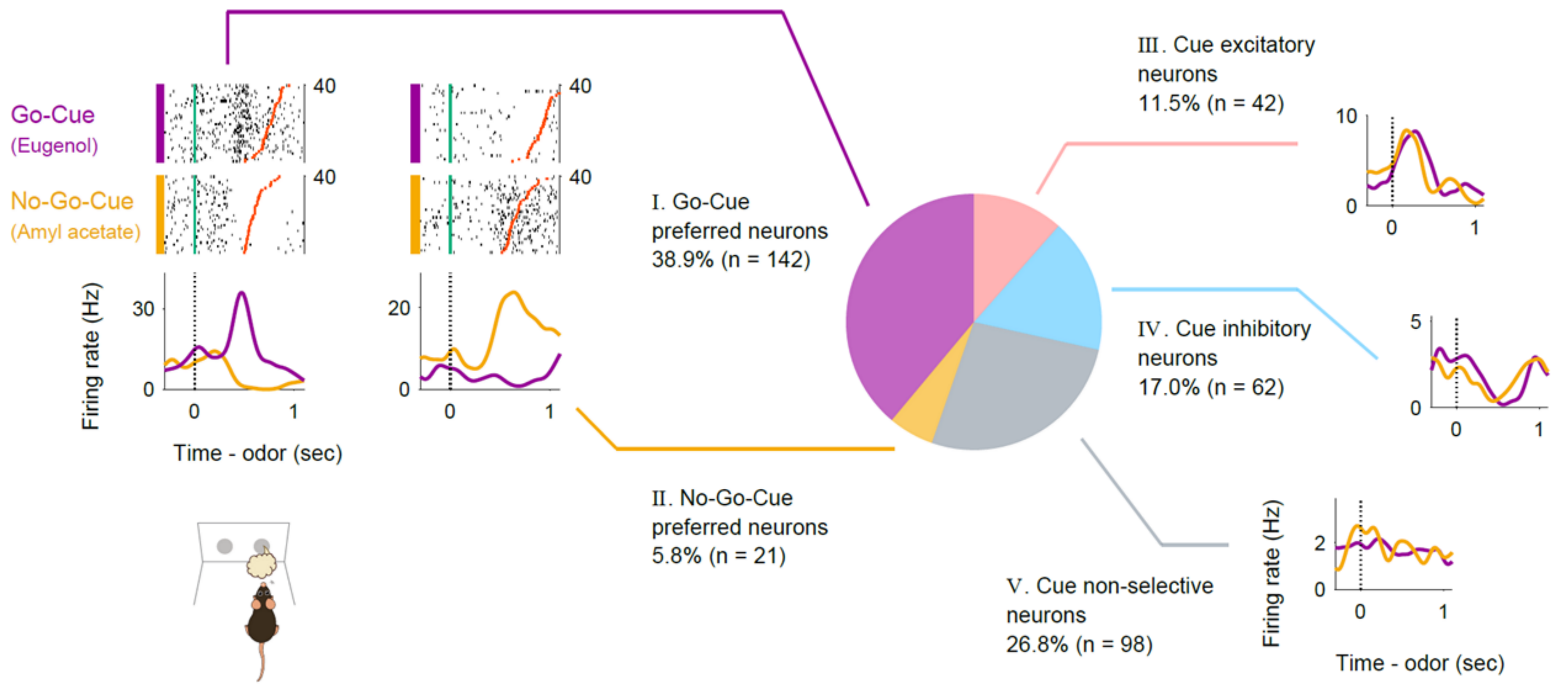
Go-Cue
(Eugenol)
No-Go-Cue
(Amyl acetate)
40
40
40
40
Firing rate (Hz)
30
0
20
0
0
1
0
1
Time - odor (sec)
I. Go-Cue
preferred neurons
38.9% (n = 142)
II. No-Go-Cue
preferred neurons
5.8% (n = 21)
III. Cue excitatory
neurons
11.5% (n = 42)
10
0
0
1
IV. Cue inhibitory
neurons
17.0% (n = 62)
5
0
0
1
V. Cue non-selective
neurons
26.8% (n = 98)
Firing rate (Hz)
2
0
0
1
Time - odor (sec)

Figure 5-2 | NLOT neuron activity patterns during the odor-guided go/no-go task

Example firing patterns of NLOT neurons during the odor sampling epoch (the time from odor valve opening to odor port exit) in the odor-guided go/no-go task. Each row contains the spikes (black ticks) for one trial, aligned to the time of odor valve opening (corresponding to the odor port entry, green ticks). Red ticks refer to the times of odor port exit. NLOT neurons were classified into five types (purple pie, type I; orange pie, type II; pink pie, type III; light blue pie, type Ⅳ; and gray pie, type Ⅴ) based on the odor-sampling epoch response.

5.5. Results: Go-cue responsive neurons bi-directionally encode cue odors with excitations and suppressions

Among the go-cue responsive neurons (type I neurons, n = 142), which represented the major population of the NLOT neurons (**Figure 5-2**), each neuron showed a sharp peak in the firing rate after ~600 ms of go-cue odor presentation and persistent suppression during the latter part of the no-go-cue odor sampling epoch (**Figure 5-3A**). To quantify the dynamics of this bi-directional cue encoding, we calculated the firing rate changes from the baseline (200-0 ms before the end of the inter-trial interval) in the sliding bins during the odor-sampling epoch for each neuron. For each accurate trial type, we calculated the auROC value at each time bin (width: 100 ms, step: 20 ms) (**Figures 5-3B-C**), and three measures from the auROC values: “onset time,” “time of center of mass,” and “duration”. The durations of the go-cue excitation responses were sharper ($p < 0.05$, Wilcoxon rank-sum test) than those of the no-go-cue suppression responses (**Figure 5-3D**). The no-go-cue suppression responses were sustained until the mice withdrew their snouts from the odor port. For each neuron, both the go-cue excitation response and the no-go-cue suppression response were observed at 450-550 ms after the odor onset (**Figure 5-3E**, $p < 0.01$, permutation test). Thus, each go-cue responsive neuron exhibited both sharp go-cue excitation and persistent no-go-cue suppression at specific times during the odor-sampling epoch.

It is possible that the sharp go-cue excitation responses correlated with the execution of the go behaviors or contained the premotor signals. To verify this possibility, we compared the peak firing rates and the half-width of firing in the go-cue excitation between the two alignment conditions (odor valve opening versus odor port exit). We observed that the peak firing rates were higher relative to the odor onset ($p < 10^{-15}$, Wilcoxon signed-rank test) and the temporal organizations were significantly tighter ($p < 0.001$, Wilcoxon signed-rank test) than the firing rate relative to the odor port exit (**Figures 5-4A-B**). Moreover, we developed an encoding model (GLM) that incorporated task-related variables from 370 ms after the odor onset (corresponding to the time that is the median of the go-cue excitation onsets measured by the auROC values) to the odor port exit as predictors of each neuron's activity to help isolate the go-cue excitation responses triggered by odor onset and action (**Figures 5-4C-D**) (Engelhard et al., 2019). Using this encoding model, we quantified the relative contribution of each behavioral variable to the response of each neuron by determining how much the explained variance declined when that variable was removed from the model. Averaged across the go-cue responsive neurons, the relative contribution of the odor-triggered response (65.6 ± 1.4%

of the total variance explained, mean ± standard error of mean [SEM]) was significantly higher than that of the pre-odor port exit (34.4 ± 1.4%) ($p < 10^{-9}$, Wilcoxon signed-rank test) (**Figure 5-4E**). These results indicated that the go-cue excitation responses of the go-cue responsive neurons were triggered by odor onset rather than pre-motor activities. Furthermore, distinct cue responses were observed in the correct go trials, and not in the trials that were correct no-go, error, or odorless, suggesting that the distinct go-cue excitation responses reflected signals eliciting appropriate motivational behavior. Notably, the intensities of majority of the cue responses remained stable across trials. In conclusion, the distinct go-cue excitation responses were triggered by odor onset and were stable with respect to the appropriate odor-guided behaviors.

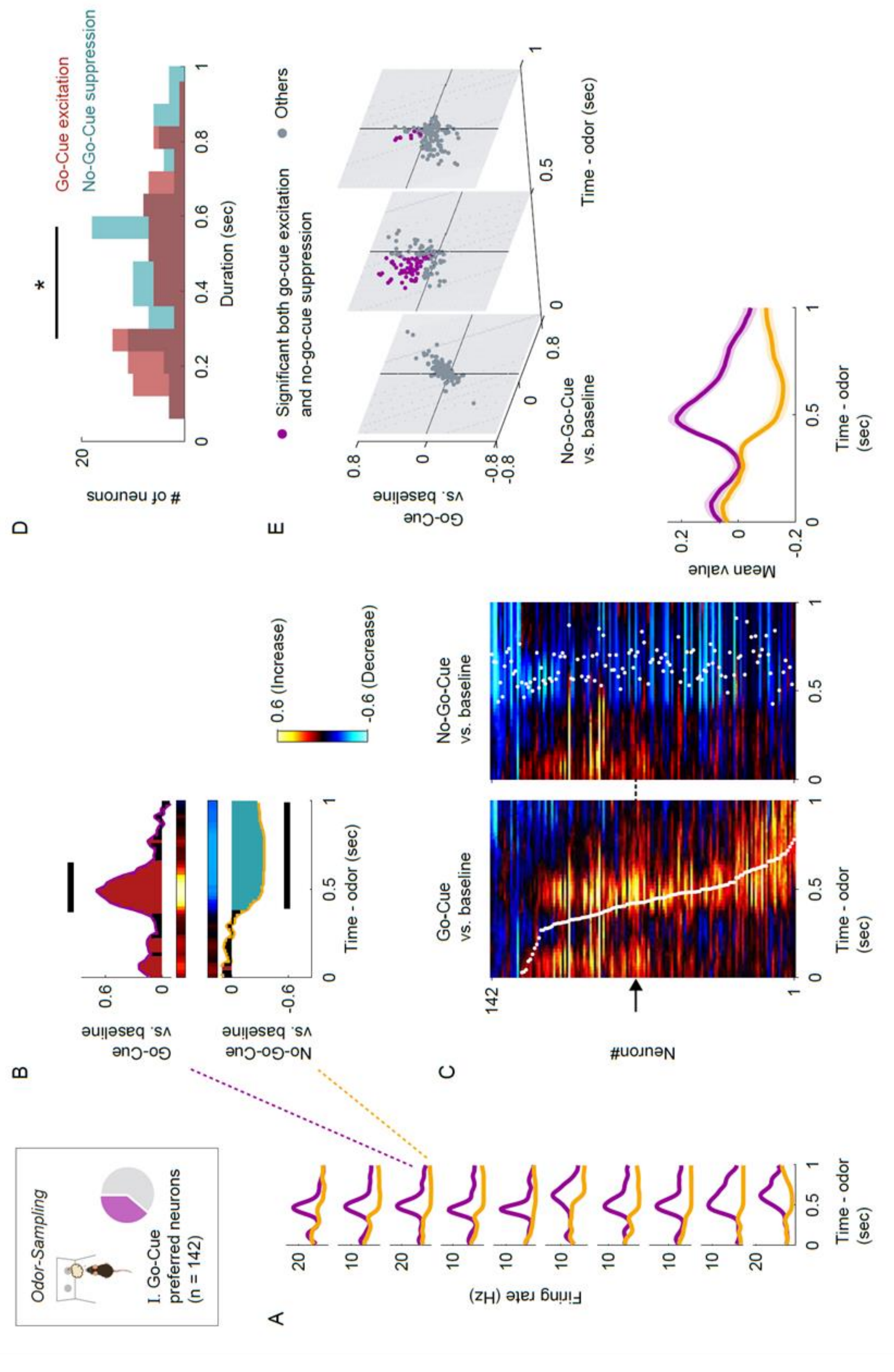
A
Odor-Sampling
I. Go-Cue preferred neurons (n = 142)
Firing rate (Hz)
20
10
20
10
10
10
10
10
10
20
0
0.5
1
Time - odor (sec)
B
Go-Cue vs. baseline
0.6
0
No-Go-Cue vs. baseline
0
-0.6
0
0.5
1
Time - odor (sec)
0.6 (Increase)
-0.6 (Decrease)
C
Neuron#
142
1
Go-Cue vs. baseline
No-Go-Cue vs. baseline
0
0.5
1
Time - odor (sec)
D
# of neurons
20
0
0.2
0.4
0.6
0.8
1
Duration (sec)
*
Go-Cue excitation
No-Go-Cue suppression
E
Go-Cue vs. baseline
0.8
0
-0.8
-0.8
0
0.8
No-Go-Cue vs. baseline
0
0.5
1
Time - odor (sec)
Significant both go-cue excitation and no-go-cue suppression
Others
Mean value
0.2
0
-0.2
0
0.5
1
Time - odor (sec)

Figure 5-3 | Go-cue responsive neurons show phasic excitation to go-cue odor and persistent suppression to no-go-cue odor

(**A**) Example firing patterns of go-cue responsive neurons during the odor-sampling epoch.

(**B**) Example of the area under the auROC values for a go-cue responsive neuron. The auROC values (aligned by odor valve opening) were calculated by go-cue odor presentation versus baseline (top), and no-go-cue odor presentation versus baseline (bottom) in the sliding bins. The red bars show significant excitation, and blue bars show significant suppression ($p < 0.01$, permutation test). Based on the significant time points, the response "durations" (black horizontal lines) were calculated.

(**C**) The auROC values for go-cue responsive neurons (n = 142, type I neurons). Each row corresponds to one neuron, with neurons in the left and middle graphs in the same order. The neurons are sorted by the times of center of mass (white dots) of the auROC values calculated by go-cue odor presentation versus baseline. The color scale is as in (**B**). An arrow indicates the same neuron as in (**B**). The average firing patterns of go-cue responsive group during the odor-sampling epoch (right).

(**D**) Distributions of the response durations for significant excitations (red) and significant suppressions (blue). Statistical significance between excitations and suppressions (*$p < 0.05$) was assessed by the Wilcoxon rank-sum test.

(**E**) Time course of excitation to go-cue odor and suppression to no-go-cue odor. Purple dots, significant both go-cue excitation and no-go-cue suppression ($p < 0.01$, permutation test); gray dots, other responses.

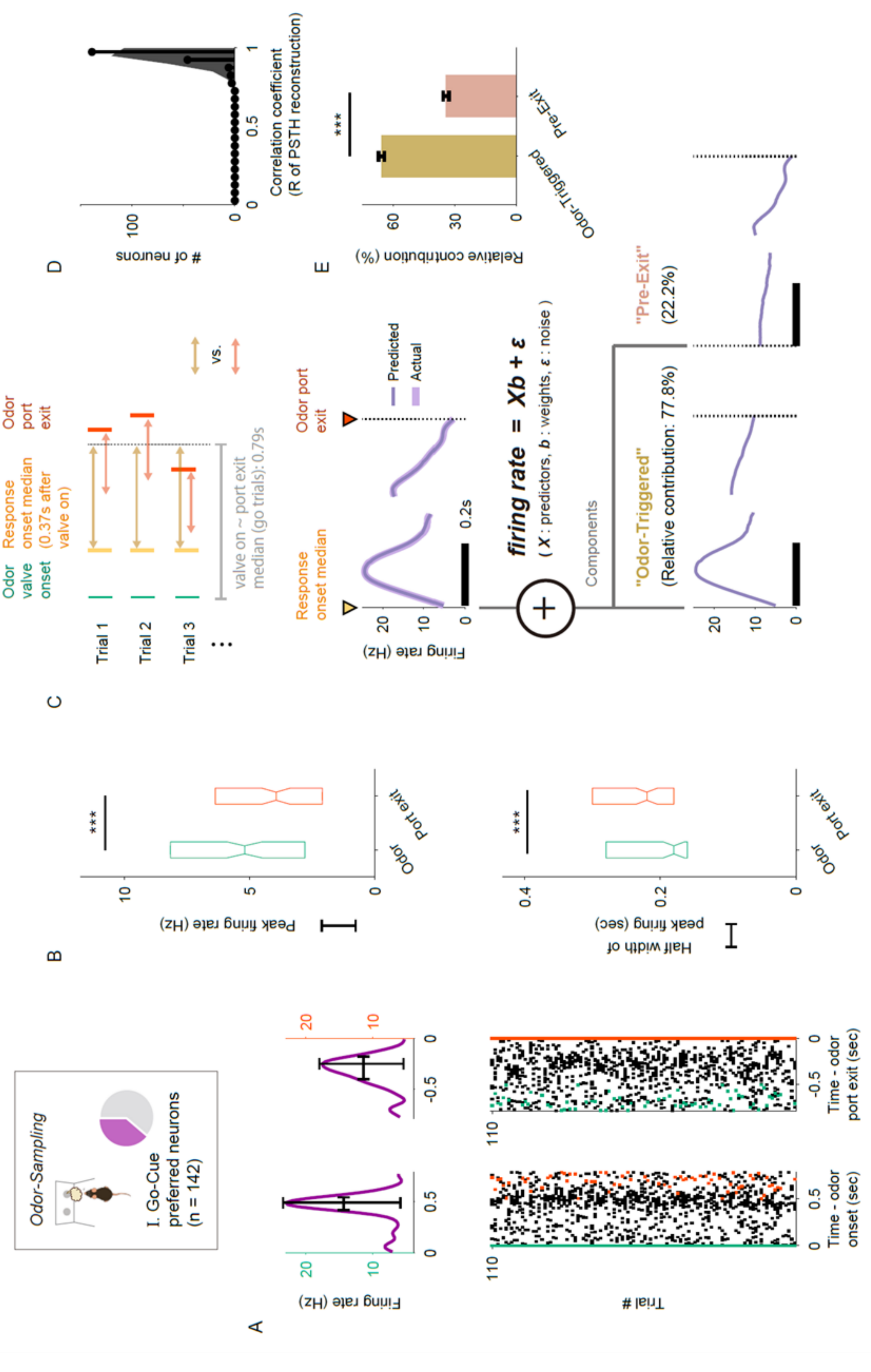
A
Odor-Sampling
I. Go-Cue preferred neurons (n = 142)
Firing rate (Hz)
20
10
0
0.5
-0.5
0
Trial #
110
Time - odor onset (sec)
Time - odor port exit (sec)
B
Peak firing rate (Hz)
10
5
0
***
Odor
Port exit
Half width of peak firing (sec)
0.4
0.2
0
C
Odor valve onset
Response onset median (0.37s after valve on)
Odor port exit
Trial 1
Trial 2
Trial 3
...
valve on ~ port exit median (go trials): 0.79s
vs.
Response onset median
Odor port exit
Predicted
Actual
Firing rate (Hz)
0.2s
firing rate = Xb + ε
(X : predictors, b : weights, ε : noise)
Components
"Odor-Triggered"
(Relative contribution: 77.8%)
"Pre-Exit"
(22.2%)
D
# of neurons
100
0
0.5
1
Correlation coefficient (R of PSTH reconstruction)
E
Relative contribution (%)
60
30
0
***
Odor-Triggered
Pre-Exit

Figure 5-4 | Go-cue excitation response triggered by odor onset rather than the initiation of an odor-guided behavior

(**A**) The activity of an example go-cue responsive neuron aligned to onset of odor valve opening (left, green ticks) or odor port exit (right, red ticks). The peak firing rate (black vertical line) and temporal half-width of the peak firing (black horizontal line) are defined from the spike histogram.

(**B**) Comparison of the peak firing rates (top) and half widths of the peak firings (bottom) between the two alignment conditions (odor valve opening versus odor port exit). The peak firing rates were higher when triggered by odor valve opening (***$p < 10^{-15}$, Wilcoxon signed-rank test). Half widths of the peak firings were longer when triggered by odor port exit (***$p < 0.001$, Wilcoxon signed-rank test).

(**C**) Schematic of the encoding model used to quantify the relationship between behavioral variables and the activity of each neuron. Inset, predicted and actual averaged firing rate relative to the odor onset and odor port exit for one neuron.

(**D**) Correlation coefficients (R of PSTH reconstructions) between predicted and actual averaged firing rate relative to the odor onset and odor port exit across the go-cue responsive neurons.

(**E**) Relative contribution of each behavioral variable to the explained variance of the neural activity, averaged across the go-cue responsive neurons. Relative contribution of the odor-triggered response was significantly higher than that of the pre-odor port exit (***$p < 10^{-9}$, Wilcoxon signed-rank test). All error bars are standard error of the mean (SEM).

5.6. Results: NLOT neuron population exhibits rapid response dynamics before executing cue-odor-evoked behaviors

We demonstrated that the go-cue responsive neurons exhibited specific temporal dynamics during odor sampling as a representative population of NLOT neurons (**Figure 5-3**). Similarly, the no-go-cue responsive neurons exhibited both no-go-cue excitation and persistent go-cue suppression during cue odor presentation (**Figure 5-2**). The cue excitatory neurons and the cue suppressed neurons also changed their firing rates during odor-sampling (**Figure 5-2**). Thus, the NLOT neurons exhibited diverse firing patterns and complex temporal dynamics during odor sampling. In this section, we examine the NLOT population encoding and the contribution of each neuron group during odor sampling using different methods of analysis.

Calculating go-cue versus no-go-cue preference during odor-sampling clearly showed the strong encodings of cue preference at 400-500 ms after odor onset across the population (**Figure 5-5A**, $p < 0.01$, permutation test). To gain insight into the dynamics of the population response, we visualized the average population activity using principal component analysis, a dimensionality reduction method. **Figure 5-5B** shows the trajectories of the mean response of the NLOT neuron population to go-cue and no-go-cue odors, represented as the projections onto the first three PCs during the odor-sampling epoch. Throughout the ~300 ms interval from the odor onset, trajectories remained converged, showing little difference across conditions. Over the late phase of odor-sampling, specifically 400-500 ms from the odor onset, trajectories in the odor-sampling epoch subspace began to spread out and were clearly separated at the population level. To quantify these observations, we measured the instantaneous separation between the population cue responses (**Figure 5-5C**). The separation reached a maximum at ~500 ms and remained above the baseline levels until the odor port exited. Additionally, we calculated the rate at which the population activity vectors changed (width: 100 ms, step: 20 ms; **Figure 5-5D**). These rates increased to a maximum within ~500 ms and remained above the baseline levels over the initiation of cue-odor-evoked behaviors (go or no-go behaviors). Thus, the NLOT neuron population showed dramatic transformations in the dynamics of cue encoding at 400-500 ms after odor onset.

Next, we examined the mechanism of the contribution of individual NLOT neurons to the population response to evaluate the absolute values of the principal component (PC) coefficients as the neural weights (**Figure 5-5E**). The values of the neural weights in the first dimension of the odor-sampling epoch subspaces showed that type I neurons contributed considerably to the population response. To further examine the contributions along the time course, we calculated the absolute values of the PC coefficients in the sliding bins (width: 100 ms, step: 20 ms) during the odor-sampling epoch (**Figure 5-5F**). The values of the neural weights in the first dimension of each bin exhibited significant contributions of type I neurons to the population response, especially during 400-500 ms after the odor onset, corresponding to the dynamics of cue encoding. These results indicated that the go-cue responsive neurons strongly contributed to the profound transformations in the dynamics of NLOT cue encoding.

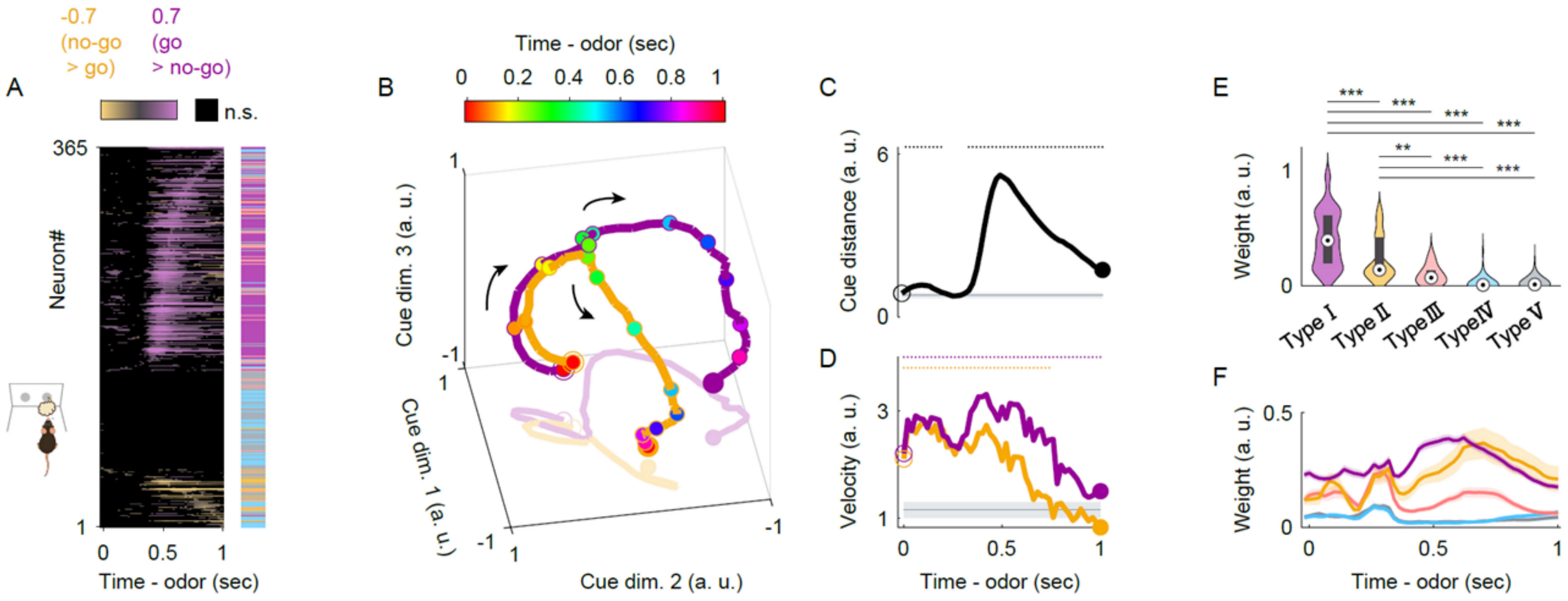A
-0.7
(no-go
> go)
0.7
(go
> no-go)
n.s.
365
Neuron#
1
0
0.5
1
Time - odor (sec)
B
Time - odor (sec)
0
0.2
0.4
0.6
0.8
1
Cue dim. 3 (a. u.)
1
-1
1
Cue dim. 1 (a. u.)
-1
1
Cue dim. 2 (a. u.)
-1
C
Cue distance (a. u.)
6
0
D
Velocity (a. u.)
3
1
0
0.5
1
Time - odor (sec)
E
Weight (a. u.)
1
0
***
***
***
***
**
***
***
Type I
Type II
Type III
Type IV
Type V
F
Weight (a. u.)
0.5
0
0
0.5
1
Time - odor (sec)

Figure 5-5 | NLOT neuron population response before the initiation of odor-guided behaviors

(**A**) The auROC values (go-cue versus no-go-cue odor presentation, aligned by odor valve opening) for all neurons. Each row corresponds to one neuron. Neurons are sorted by the peak time for the auROC values. The color scale indicates significant preferences ($p < 0.01$, permutation test; positive values correspond to the go-cue responsive responses). The black boxes indicate bins with non-significant preferences ($p > 0.01$, permutation test). The colored box on the right shows the neuron type for each neuron (purple, type I; orange, type II; pink, type III; light blue, type Ⅳ; gray, type Ⅴ).

(**B**) Visualization of the NLOT neuron population responses during odor-sampling epoch using principal-component analysis ($n = 365$ NLOT neurons). The responses to cue odors are projected onto the first three PCs corresponding to the odor-sampling epoch subspaces. Purple line, go-cue odor; orange line, no-go-cue odor. Temporal progression is depicted from unfilled purple/orange spheres to filled purple/orange spheres.

(**C**) The distance between NLOT neuron population responses. The gray line and shaded areas show the mean ±2 standard deviation (SD) baseline values during the baseline epoch. Top dots indicate the time bins showing values more than mean +2 SD baseline values.

(**D**) Rate of change (velocity) of NLOT neuron population responses. Purple line, go-cue odor; orange line, no-go-cue odor. The gray line and shaded areas show the mean ±2 SD baseline values during the baseline epoch. Top dots indicate the time bins showing values more than mean +2 SD baseline values.

(**E**) Neural weights in the first dimension of the odor-sampling epoch subspaces. Box plots in violin plots indicate medians and interquartile ranges. Purple, type I; orange, type II; pink, type III; light blue, type Ⅳ; gray, type Ⅴ. The statistical significance among five groups (**$p < 0.01$, ***$p < 0.001$) was assessed by one-way analysis of variance (ANOVA) with Tukey's post hoc test.

(**F**) Neural weights along the time course in the first dimension of each sliding bin (width: 100 ms, step: 20 ms). The shaded areas represent Gstandard error of the mean (SEM). Purple, type I; orange, type II; pink, type III; light blue, type Ⅳ; gray, type Ⅴ.

5.7. Results: NLOT neurons provided sufficient information to account for behavioral accuracy

To examine whether the population activity accounted for the animals' behavioral accuracy, we performed a decoding analysis. This analysis determined whether the firing rates of the NLOT neuron populations could be used to classify each individual trial as go or no-go. We used SVMs with linear kernels as a decoder. Analyses of the decoding time course based on NLOT neurons using a sliding time window revealed that the decoding accuracy was maintained at chance levels 300 ms after odor onset; subsequently, it dramatically increased above the level of animals' behavioral accuracy 400-500 ms after the odor onset (**Figure 5-6**). In the 400-500 ms period, 124 neurons provided sufficient information to account for behavioral accuracy (the top right panel in **Figure 5-6**). Thus, <150 NLOT neurons provided sufficient information to account for behavioral accuracy at least 500 ms after odor onset.

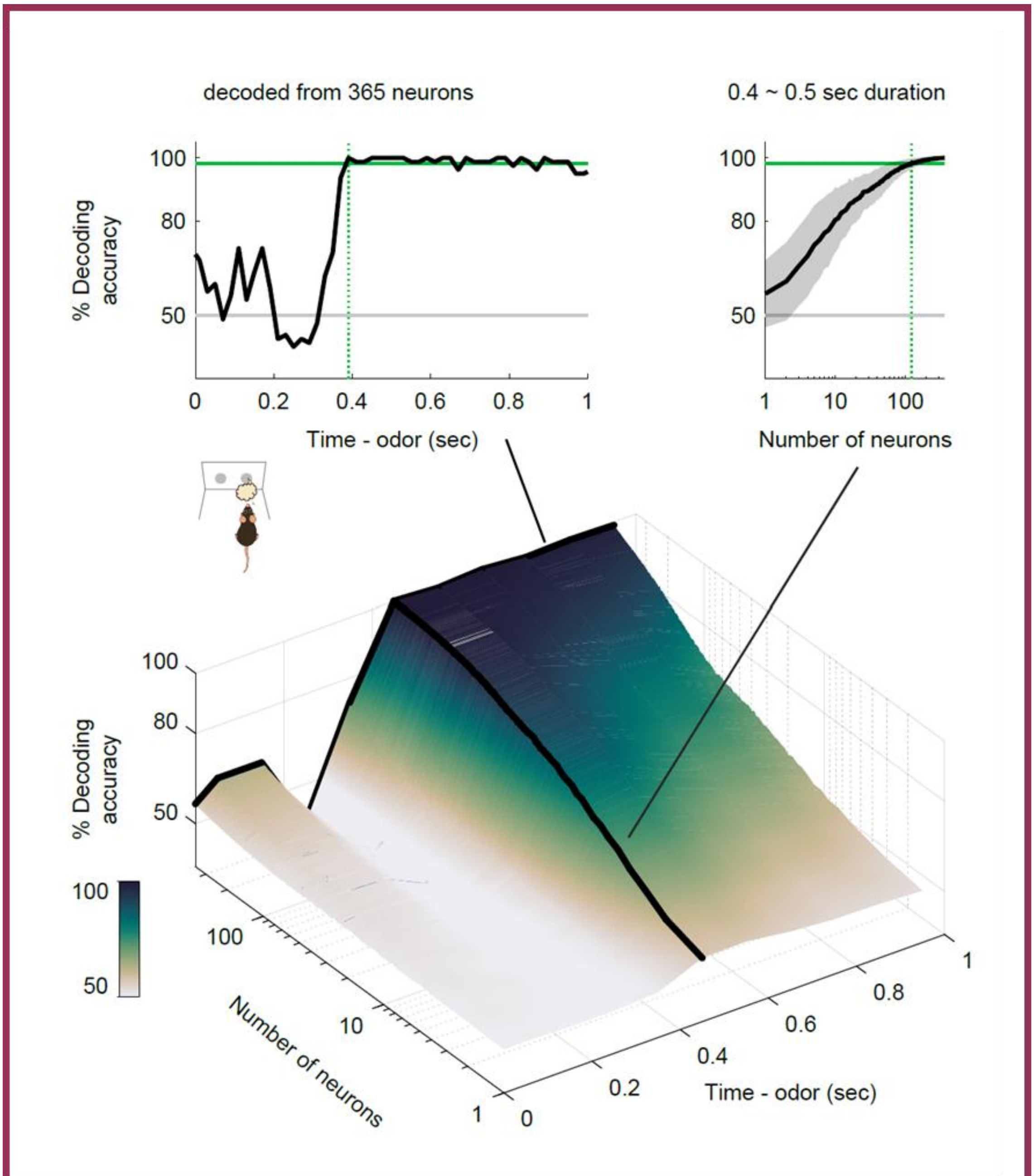

Figure 5-6 | NLOT neurons provided sufficient information to account for behavioral choices

Time course of odor decoding accuracy. A vector consisting of instantaneous spike counts for 1–365 neurons in a sliding window was used as an input for the classifier. Training of the classifier and testing was performed at every time point.

Green horizontal lines indicate the level of animal behavioral performance. Gray horizontal lines indicate chance levels (50%). Green vertical dashed lines indicate the first points wherein the decoding accuracy reached the level of the animal behavioral performance. Areas with shading represent ±SD.

5.8. Results: Bi-directional cue-outcome encoding following odor-guided behaviors

Our analyses of the dynamics of cue encoding suggest that several NLOT neurons maintained cue selective responses during cue-odor-evoked behaviors after odor sampling. Notably, the persistent suppression responses of type I neurons during no-go-cue odor-sampling were sustained over the odor port exit (**Figures 5-3B-D**). This raises the question of whether the selectivity disappears or persists once the cue-odor-evoked behaviors are executed. By aligning the neural activity to behavioral events, we noticed that type I neurons were selective for the reward drinking behavior after go-cue odor-sampling and the persistent suppression responses were sustained during the no-go waiting behavior after no-go-cue odor sampling (**Figure 5-7A**). We quantified the response profiles of each neuron group during odor-evoked behaviors by calculating the firing rate changes from baseline (**Figures 5-7B-C**, the spike data were aligned to the odor port exit and water port entry). Across the population, several type I neurons showed significant excitatory responses for drinking behavior (purple histogram at the top in **Figure 5-7B**, $p < 0.01$, permutation test), and significantly suppressed responses for the no-go waiting behavior (purple histogram at the bottom in **Figure 5-7C**, $p < 0.01$, permutation test). The drinking responses of type I neurons were higher than those of other groups, and the no-go waiting responses of type I neurons were lower than those of other groups, indicating that they were type I neuron specific responses (one-way analysis of variance with Tukey's post hoc test). For each neuron, the suppressions were maintained for 800 ms (interquartile range: 290-1,480 ms) from the initiation of the no-go behavior. Thus, type I neurons exhibited associations between the go-cue excitations and excitatory responses for drinking behavior with persistent no-go-cue suppressions, suggesting that NLOT neurons are involved in cue-outcome associations.

We aimed to determine whether other neuron groups responded to cue-odor-evoked behavioral states. Several type II neurons showed significantly suppressed responses for drinking behavior (orange histogram at the bottom in **Figure 5-7B**, $p < 0.01$, permutation test) and significant excitatory responses for the no-go waiting behavior (orange histogram at the top in **Figure 5-7C**, $p < 0.01$, permutation test). The drinking responses of type II neurons were lower than those of type I neurons, and the no-go waiting responses of type II neurons were higher than those of type I neurons (one-way analysis of variance with Tukey's post hoc test). Thus, the type I and type II neurons contrastingly encoded the go/no-go behavioral states after odor-sampling. Furthermore, a subset of type III, IV, and V neurons tended to show an excitatory response in a specific time window in behavioral epochs, with suppressed responses relative to other behavioral epochs, which is consistent with our previous findings in the ventral tenia tecta of the olfactory cortex (Shiotani et al., 2020b). In particular, each type IV neuron maintained the excitatory response to the no-go waiting state (light blue histogram at the top in **Figure 5-7C**, $p < 0.01$, permutation test) for 560 ms (interquartile range: 205–1,200 ms), from 290 ms (interquartile range: 210–650 ms) after initiation of the no-go behavior. These results indicate that each NLOT neuron group showed a specific firing pattern during odor-guided behaviors, depending on the response profiles in the odor-sampling epochs.

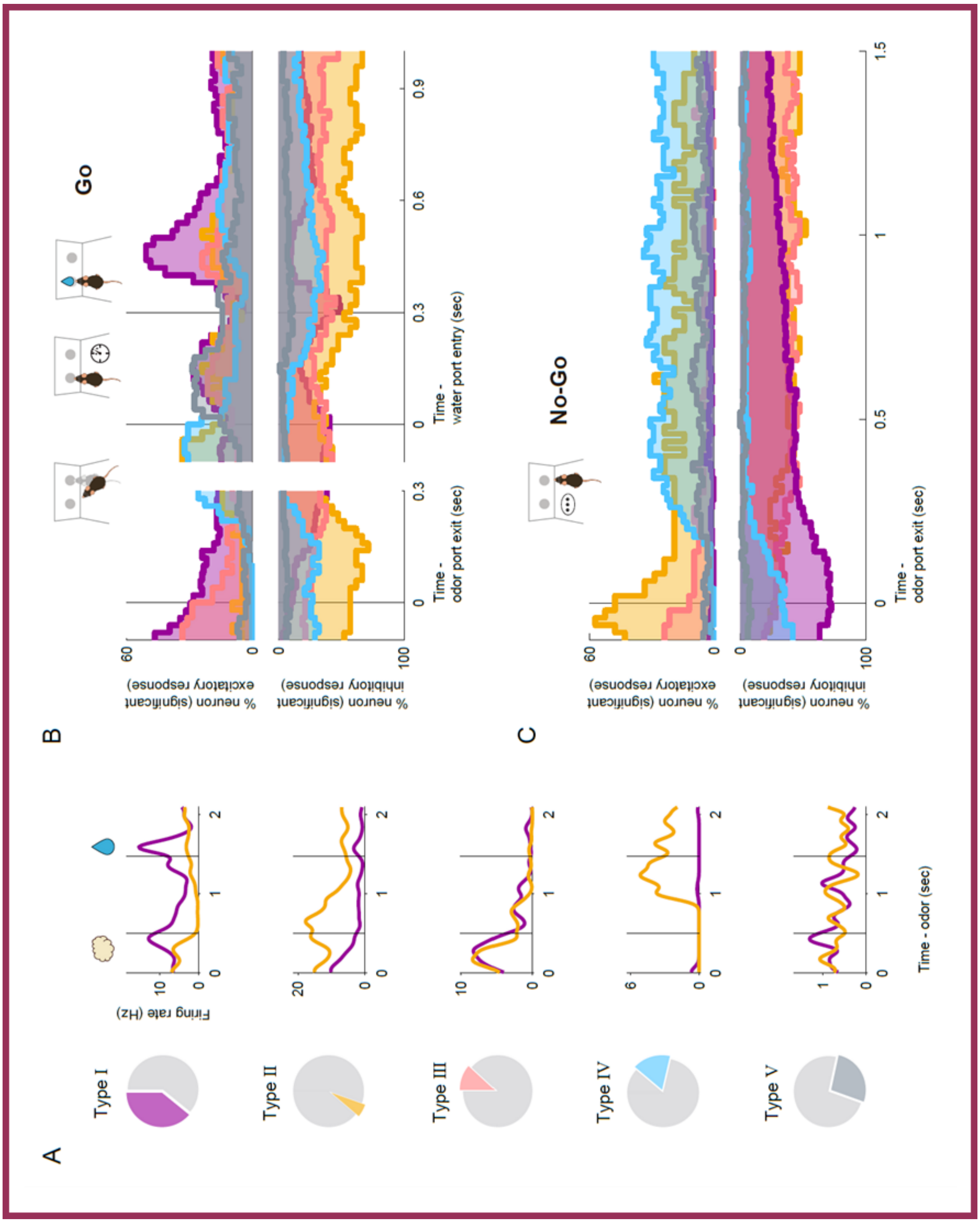
A
Type I
Type II
Type III
Type IV
Type V
Firing rate (Hz)
10
0
20
0
10
0
6
0
1
0
0
1
2
Time - odor (sec)
B
Go
% neuron (significant excitatory response)
60
0
% neuron (significant inhibitory response)
0
100
0
0.3
Time - odor port exit (sec)
0
0.3
0.6
0.9
Time - water port entry (sec)
C
No-Go
% neuron (significant excitatory response)
60
0
% neuron (significant inhibitory response)
0
100
0
0.5
1
1.5
Time - odor port exit (sec)

Figure 5-7 | NLOT neurons exhibits bidirectional cue-outcome encoding following odor-guided behaviors

(**A**) Example firing pattern of each neuron group following odor-guided behaviors. Vertical black lines indicate the odor valve offset and the onset of water reward.

(**B**) The proportions of neurons that exhibited significant responses were calculated from the auROC values ($p < 0.01$, permutation test) in correct go trials for each neuron group (top, excitation; bottom, suppression). Vertical black lines indicate the odor port exit, water port entry, and the onsetofwater reward. Purple, type I; orange, type II; pink, type III; light blue, type Ⅳ; gray, type Ⅴ.

(**C**) Same as (B), for correct no-go trials.

5.9. Discussion: Insights based on the results

The purpose of the study was to understand the electrophysiological features of NLOT neurons in decision-making processes that occur during various behavioral states in odor-guided go/no-go tasks. In this study (Tanisumi et al., 2021), we provided the first recording of neuronal activity in the NLOT in freely behaving mice performing odor-guided go/no-go tasks. Indeed, NLOT neurons exhibited diverse neural activities in response to odor presentations and cue odor-evoked behaviors in the task.

Previous anatomical studies have shown that the NLOT receives odor information from the olfactory bulb and various areas of the olfactory cortex, including the piriform cortex (Luskin and Price, 1983a; Price, 1973). Subsequently, NLOT neurons project to the ventral striatum consisting of the olfactory tubercle (OT) and the nucleus accumbens (NAc), and also send the axons into the basolateral amygdala (BLA) (Luskin and Price, 1983a; Price, 1973; Santiago and Shammah-Lagnado, 2004), which plays a critical role in regulating motivated behaviors (Cox and Witten, 2019; Janak and Tye, 2015; Murata et al., 2015). Moreover, a recent study (Vaz et al., 2017) has shown that NLOT-lesioned rats exhibited olfactory-related behavioral deficits with an inability to identify and discriminate between odors and interfere with the display of innate odor-evoked behaviors, such as sexual behavior, aggression, and avoidance of predators.

Despite the accumulation of knowledge, the role of NLOT in the functional circuit to convert odor information into appropriate behaviors has not been clarified.

In this study, we classified five types of neurons based on their firing patterns during the odor-sampling epochs. A majority of NLOT neurons (type I neurons, go-cue responsive neurons) exhibited phasic excitatory responses during go-cue odor-sampling epochs and sustained suppressed responses during no-go-cue odor-sampling epochs (**Figures 5-2, 5-3, and 5-4**). The activity pattern of the no-go-cue responsive neurons (type II neurons) was opposite to that of the go-cue responsive neurons. These bi-directional cue encoding patterns were similar to the cue encoding in the brain reward circuit, including the ventral striatum and the ventral tegmental area (Cohen et al., 2012; Menegas et al., 2017; Stephenson-Jones et al., 2020) rather than the olfactory circuit (Cury and Uchida, 2010; Miura et al., 2012; Uchida et al., 2014) during cue-outcome association tasks. We also demonstrated that the go-cue and no-go-cue responsive neurons highly contributed to the population dynamics of cue encoding and decoding, for accuracy of the animal's choices (**Figure 5-5**), suggesting that these bi-directional response neurons for cue odors effectively provided sufficient information to account for the behavioral choices. These bi-directional cues encoding a small number of neurons with a high level of information may be effective in the NLOT with only a small volume of 0.24 mm^3 and 19,000 neurons (Vaz et al., 2016).

The go-cue responsive neurons also showed firing activities during drinking behavior (**Figure 5-7B**), consistent with other brain areas involved in motivational processes (Steinmetz et al., 2019; Watabe-Uchida et al., 2017). Additionally, the go-cue responsive neurons exhibited suppressed responses to the no-go waiting behavioral states (**Figure 5-7C**). Moreover, the no-go-cue responsive neurons suppressed their firing activity during the go behavioral states and exhibited excitatory activities in the no-go behavioral states (**Figures 5-7B-C**). These results suggest that these NLOT neurons functionally associated cue odor with the precise task outcomes derived from odor information. In other olfactory cortical areas, including the piriform cortex and OT, the odor-reward association reflects the cue odor responses (Calu et al., 2007; Gadziola et al., 2020, 2015; Gadziola and Wesson, 2016; Millman and Murthy, 2020; Roesch et al., 2006). Although further studies are required to determine whether cue responses in the NLOT represent cue-reward learning, these cue-reward combination activities may play a role in odor-reward association learning. We speculated that the NLOT is one of the critical components of the circuitry responsible for creating and providing signals eliciting appropriate behaviors. Due to the function of NLOT, we assumed that the lesion in NLOT caused suppression of olfactory-driven behaviors (Vaz et al., 2017).

The subsets of type III, IV, and V neurons exhibited an excitatory response in a specific time window in behavioral epochs and suppressed responses relative to other behavioral epochs. Similarly, our recent study has revealed that the individual neuron in the ventral tenia tecta, which is a part of the olfactory cortex, is tuned to a specific behavioral state in mice encountered during odor-guided behaviors (Shiotani et al., 2020b). Moreover, a recent study has shown the brain-wide global representation of state-dependent activity during odor-guided motivated behavior (Allen et al., 2019; Steinmetz et al., 2019). Together, the context-dependent activities of the type III, IV, and V neurons may contribute to the brain-wide specific information processing mode in the brain and be shared across the olfactory cortex.

5.10. Discussion: The hypothesis of the NLOT with layer-specific functional projections and future directions.

Olfactory information is transmitted to the NLOT with a three-layered structure (layers I, II, and III). The NLOT layer II neurons contribute to >80% of the total neuronal population of the NLOT (Vaz et al., 2016), and project to the dwarf cell regions in the

OT (Santiago and Shammah-Lagnado, 2004). The OT sends a major projection to the ventral pallidum regulating expected positive and negative valences. The layer II neurons also project to the NAc shell (Santiago and Shammah-Lagnado, 2004) that processes hedonic or motivational values. Similar to the neural responses in these areas, we demonstrated the reward-predicting cue and reward signals of type I neurons in the NLOT (**Figures 5-3 and 5-7**). Based on a recent frontal cortex research showing a connectivity-defined neuron type that carries a single variable (Hirokawa et al., 2019). we speculated that type I neuron outputs in the NLOT layer II to the OT and NAc contribute to the encoding of positive or negative valences of expected and actual outcomes, and hedonic or motivational value.

Conversely, the NLOT layer III neurons project to the BLA (Santiago and Shammah-Lagnado, 2004), which is an essential component of the amygdala underlying fear conditioning memory. We demonstrated the no-go-cue responses of the type II neurons (**Figure 5-7**) and the sustained positive responses to the no-go behaviors of type IV neurons. We assumed that these specific firing patterns in the NLOT layer III might contribute to the fear-conditioning memory circuits. However, we did not verify the firing pattern of NLOT neurons in fear memory tasks. Future experiments are required to monitor the changes in the firing activity in the NLOT during odor-punishment association tasks.

We acknowledge that there are several limitations to this study. First, although we performed the first in vivo recording of neuronal activity in the NLOT during only an odor-guided go/no-go task, our data do not reflect the neuronal activity across different cue modalities, behavioral paradigms, and contexts. However, our data are potentially important in that the NLOT neural activity in freely behaving mice is modulated by the motivation of learned, odor-guided, and goal-directed behaviors, and may provide basic information regarding NLOT encoding in positive and negative motivational contexts, reversal learning, and innate odor-driven behaviors (Root et al., 2014). Second, a direct relationship between the distinct cue response of NLOT neurons and context-dependent motivated behaviors is unclear. Third, the response profiles and functions of the NLOT-specific projections to OT, NAc, and BLA on motivational processes have not yet been clarified. By using optogenetic manipulation or the fiber photometry tool to monitor cell-type and projection specific population activity, future studies can build on the paradigm and findings described here to address how the NLOT interacts with the projected areas to mediate the processes necessary for odor-guided behavior.

In conclusion, we extended the concept that NLOT integrity is required for normal functioning of the olfactory system (Vaz et al., 2017), and hypothesized that the NLOT plays a critical role in providing odor information that elicits appropriate behavioral motivation in the motivation circuits in odor-guided behavior. From a broad perspective, the verification of this hypothesis may have important implications for studying and leveraging neural circuits underlying odor-evoked motivation in health and disease.

Chapter 6. Research: anterior cortical amygdaloid nucleus (ACo) in the OC

6.1. Short summary

To explore how the top-down inputs to the OC suggested in the above chapters are distributed to the OC subareas, it is necessary to investigate the activity of subareas with unique anatomical backgrounds. The anterior cortical amygdaloid nucleus (ACo) is one of the olfactory cortices and a part of the olfactory cortical amygdala. Using an extracellular recording, we demonstrate ACo neurons encode reward-related cue preference and reward anticipation, suggesting they may be involved in reward-related behavioral learning by associating the olfactory information with reward anticipation (Shiotani et al., 2020a).

6.2. Introduction

The ACo is a part of the olfactory cortical amygdala and has a bidirectional connection with the amygdala. A neural tracing study reported that the ACo receives dense projections from the main olfactory bulb, moderate projections from the piriform cortex, lateral entorhinal cortex, basomedial amygdaloid nucleus (BMA), and medial amygdaloid nucleus (Me), and scarce projections from the ventral tegmental area (VTA) and the ventral tenia tecta (vTT) (Cádiz-Moretti et al., 2017). Moreover, the ACo projects densely to BMA (Cádiz-Moretti et al., 2017). These anatomical studies indicate that the ACo is closely related to the amygdala, and it is possible that the ACo is involved in odor-evoked motivational behaviors.

A behavioral study revealed that the ACo participates in olfactory fear conditioning in rats as electrical stimulation of the olfactory bulb induces evoked field potential signals, that are persistently potentiated specifically in the ACo after training (Sevelinges et al., 2004). Moreover, electrical stimulation of the VTA showed that the ACo, besides other mesolimbic structures, displays increased Fos expression in rats (Majkutewicz et al., 2010). A whole-cell patch clamp study showed that with the activation of sodium conductance, pyramidal neurons of the ACo displayed rhythmic fluctuations of intrinsically generated voltage-dependent membrane potential in the theta-low beta range, suggesting that the ACo was related to synaptic plasticity and learning (Sanhueza and Bacigalupo, 2005). The ACo has been poorly investigated, but comprehensive evidence suggests that it may play a prominent role in reward-related behavioral learning by olfactory stimulation.

However, little is known about the electrophysiological features of the ACo neurons for reward-related behavioral tasks. Here, we recorded the neural activity of ACo neurons during odor-guided reward-directed behaviors. Many ACo neurons responded to the go-cue odor stimulus at the late phase of the odor-sampling epoch. The ACo neuron population showed profound and persistent transformations in the dynamics of cue encoding over 400 ms after odor onset. Furthermore, we found that the ACo neuron groups each coded a different type of anticipation signal: one neuron group type exhibited gradual increases in the signals to the reward, while the other type showed phasic anticipation signals with the go-cue preference responses during odor sampling. Our results suggest that the ACo neurons may play an important role in odor-guided reward-directed learning.

6.3. Results: Go-cue-odor preferred responses of ACo neurons during the late phase of odor-sampling epoch

We recorded 158 well-isolated neurons in the ACo of four mice performing an odor-guided go/no-go task (**Figures 6-1A-B**). After the mice were well trained, their behavioral accuracy remained above 80% throughout the session. For all mice, the median duration of the odor-sampling epoch (the time from odor valve opening until the mouse withdrew its snout from the odor port) was 1053 ms (interquartile range: 902–1212 ms) in the go trials, and 764 ms (interquartile range: 657–968 ms) in the no-go trials (31 sessions from four mice).

Since the ACo receives direct inputs from the mitral cells of the olfactory bulb, we first focused on whether ACo neurons exhibited cue-odor selective activity during odor-sampling epochs (from odor poke-in to odor poke-out). We found that a subset of ACo neurons increased their firing rates during the odor presentation phase (0–500 ms after the odor valve opening) during both go and no-go trials, and then showed a go-cue-odor preferred response 500 ms after the odor onset (an example shown in **Figure 6-1C**). To quantify the dynamics of the cue-encoding, we calculated the firing rate changes from baseline (200 to 0 ms before the end of the inter-trial interval) in the sliding bins during the odor-sampling epoch for each neuron. For each correct trial, we calculated the auROC value at each time bin (width: 100 ms, step: 20 ms), and defined the go-cue selective neurons (n = 57 neurons, 36.1 % of the recorded neurons) as those neurons that significantly increased their firing rates from the baseline ($p < 0.01$, permutation test) for five consecutive bins (100 ms) during the odor-sampling epoch in the go correct trials (**Figure 6-1D**). Across the go-cue odor-selective population, calculation of go-cue versus no-go-cue preferences during odor-sampling epochs clearly showed a go-cue preference manner from 500 ms after the odor onset to the odor poke-out (late phase of the odor sampling epoch) (**Figure 6-1E**, $p < 0.01$, permutation test). These results suggest that the ACo received not only a particular odorant profile directly from the olfactory bulb but rather the complex odor information, including behavioral contexts from other olfactory cortical areas and top-down inputs from higher areas.

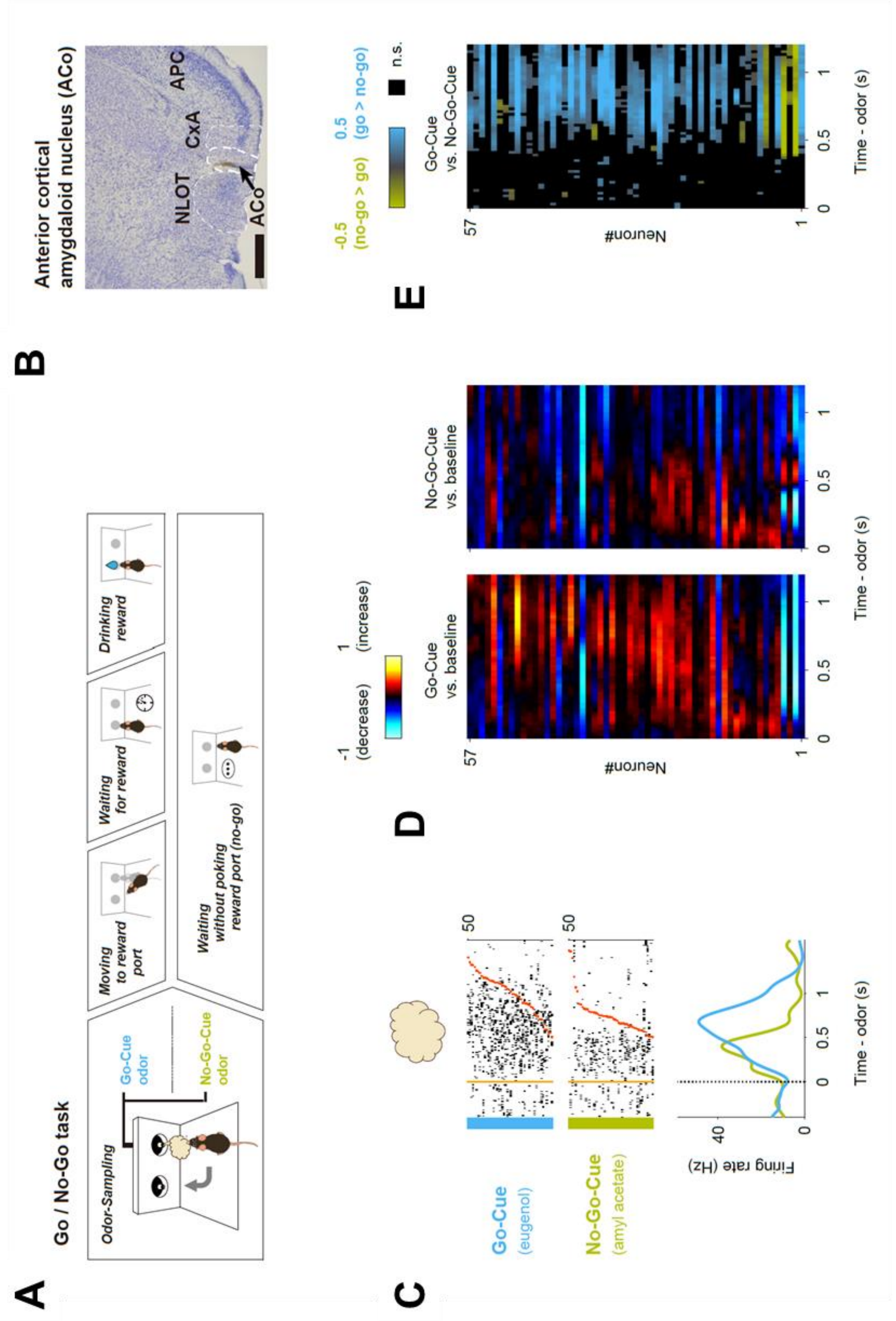
A
Go / No-Go task
Odor-Sampling
Go-Cue odor
No-Go-Cue odor
Moving to reward port
Waiting for reward
Drinking reward
Waiting without poking reward port (no-go)
B
Anterior cortical amygdaloid nucleus (ACo)
NLOT
CxA
APC
ACo
C
Go-Cue (eugenol)
No-Go-Cue (amyl acetate)
50
50
Firing rate (Hz)
40
0
0
0.5
1
Time - odor (s)
D
-1 (decrease)
1 (increase)
Go-Cue vs. baseline
No-Go-Cue vs. baseline
57
Neuron#
1
0
0.5
1
Time - odor (s)
E
-0.5 (no-go > go)
0.5 (go > no-go)
n.s.
Go-Cue vs. No-Go-Cue
57
Neuron#
1
0
0.5
1
Time - odor (s)

Figure 6-1 | Cue-Odor-preferred responses of ACo neurons during the late phase of odor-sampling in the odor-guided go/no-go task

(**A**) Time course of the odor-guided go/no-go task.

(**B**) Nissl-stained frontal section (an arrow indicates recording track) and recording tracks (vertical thick lines) of the ACo. Scale bar: 500 μm.

(**C**) Example firing patterns of ACo neurons during odor-sampling epoch (the time from odor valve opening to odor port exit) in the odor-guided go/no-go task. Red ticks represent times of odor port exit.

(**D**) auROC values for go-cue selective neurons (n = 57). auROC values (aligned by odor valve opening) were calculated by go-cue odor presentation versus baseline (left) and no-go-cue odor presentation versus baseline (right) in the sliding bins. Red, increase from baseline; blue, decrease from baseline. Each row corresponds to one neuron, with neurons in the left and right graphs in the same order. Neurons are sorted by the peak time for auROC values calculated by go-cue odor presentation versus baseline.

(**E**) Cue preference curves (auROC values, go-cue versus no-go-cue odor presentation, aligned by odor valve opening, odor port exit) for go-cue selective neurons. Each row corresponds to one neuron, with neurons in the left and right graphs in the same order of (**D**). Color scale indicates significant preferences ($p < 0.01$, permutation test; positive values correspond to the go-cue preferred responses). The black boxes indicate bins with non-significant preferences ($p > 0.01$, permutation test).

6.4. Results: Late phase of go-cue odor preferred responses were evoked by the odor onsets and were stable across trials

The go-cue odor-selective population showed cue-odor-preferred responses during the late phase of the odor sampling epoch (**Figure 6-1C**). It is possible that the late phase of odor-preferred responses was tuned to the odor port exit behaviors or contained the premotor signals that were observed in many brain regions (Allen et al., 2019; Parker et al., 2020; Steinmetz et al., 2019). To take these signals into account, and to help isolate signals related to odor presentation and action, we developed an encoding model (GLM). This model incorporated task-related variables during the odor-sampling epoch as predictors of each neuron's activity (**Figure 6-2A**) (Engelhard et al., 2019).

Using this encoding model, we quantified the relative contribution of each behavioral variable during the odor-sampling epoch to the response of each neuron by determining how much the explained variance declined when that variable was removed from the model (a relative contribution for an example neuron is shown in **Figure 6-2A**). Averaged across the go-cue odor selective population, the highest relative contribution during odor-sampling epochs was attributed to late go-cue odor sampling (36.1 ± 3.3% of the total variance explained during the odor-sampling epoch), followed in descending order by the go-cue odor presentation (23.2 ± 1.7%), the no-go-cue odor presentation

(18.5 ± 1.6%), the late no-go-cue odor sampling (9.9 ± 1.5%), pre-go-behavior (8.2 ± 1.7%), and pre-no-go behavior (4.2 ± 0.7%) (bars in **Figure 6-2B**). The relative contributions of the late go-cue odor sampling were significantly positive across 71.9% of the go-cue odor-selective neurons (a pie chart in **Figure 6-2B**). Furthermore, across the population, the go-cue responses during odor-sampling epochs in both correct and error trials were higher than those in the no-go-cue correct and odorless trials (**Figure 6-2C**), suggesting that the go-cue excitation responses mainly reflected signals of encoding cue-odor information. Notably, the intensities of most of the go-cue responses remained stable across trials (**Figure 6-2D**). Taken together, the go-cue-preferred responses during the late phase of the odor-sampling epoch were considered to reflect the go-cue odor information.

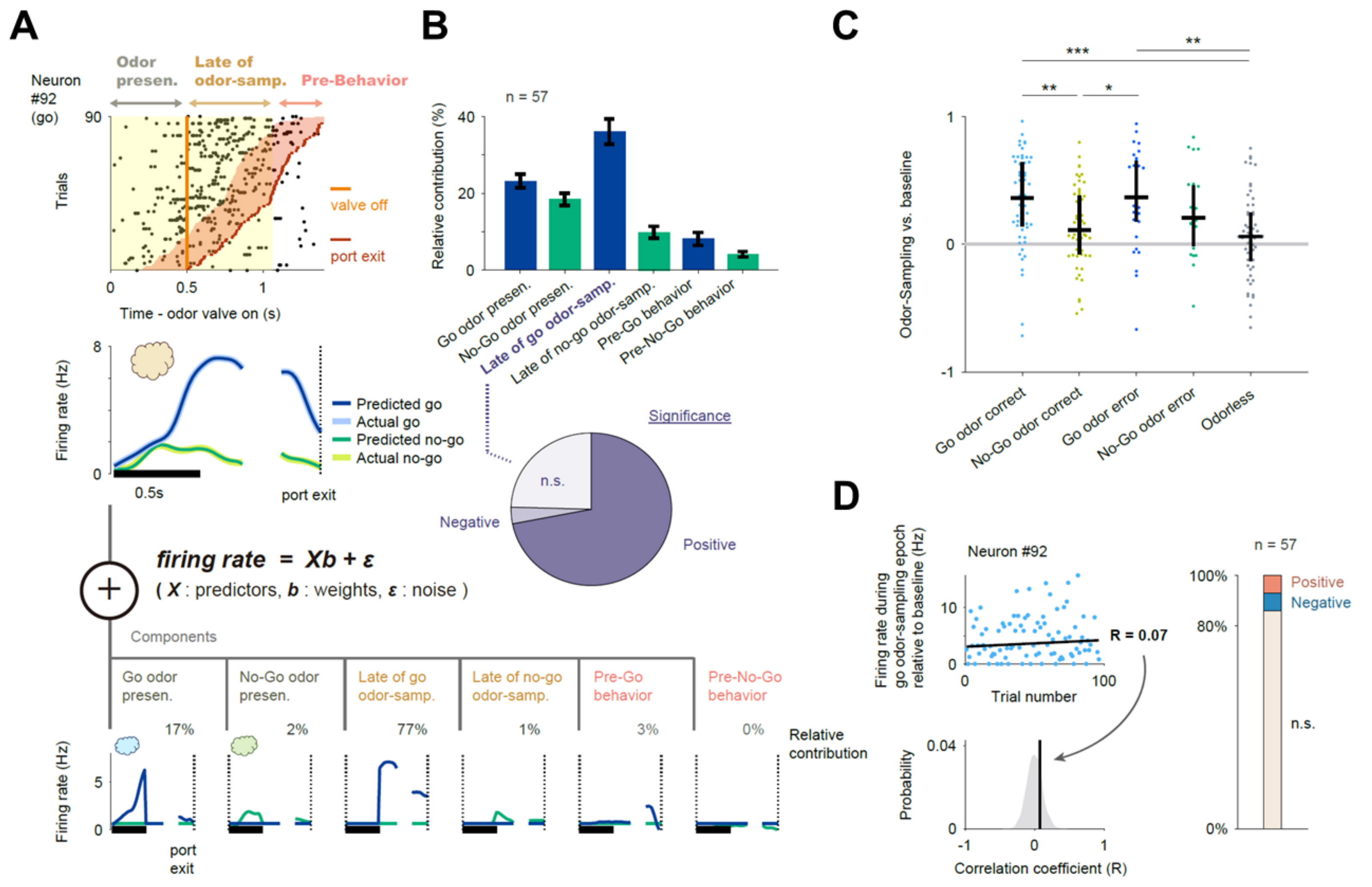
A
Neuron #92 (go)
Odor presen.
Late of odor-samp.
Pre-Behavior
Trials
90
0
0.5
1
Time - odor valve on (s)
valve off
port exit
Firing rate (Hz)
8
0
0.5s
port exit
Predicted go
Actual go
Predicted no-go
Actual no-go
firing rate = Xb + ε
(X : predictors, b : weights, ε : noise)
Components
Go odor presen.
No-Go odor presen.
Late of go odor-samp.
Late of no-go odor-samp.
Pre-Go behavior
Pre-No-Go behavior
17%
2%
77%
1%
3%
0%
Relative contribution
Firing rate (Hz)
5
0
port exit
B
n = 57
Relative contribution (%)
40
20
0
Go odor presen.
No-Go odor presen.
Late of go odor-samp.
Late of no-go odor-samp.
Pre-Go behavior
Pre-No-Go behavior
Significance
n.s.
Negative
Positive
C
***
**
**
*
Odor-Sampling vs. baseline
1
0
-1
Go odor correct
No-Go odor correct
Go odor error
No-Go odor error
Odorless
D
Neuron #92
Firing rate during go odor-sampling epoch relative to baseline (Hz)
10
0
0
100
Trial number
R = 0.07
Probability
0.04
0
-1
0
1
Correlation coefficient (R)
n = 57
100%
80%
0%
Positive
Negative
n.s.

Figure 6-2 | Late go-cue odor-preferred responses were evoked by the odor onsets and were stable

(**A**) Schematic of the encoding model used to quantify the relationship between behavioral variables and the activity of each neuron. Behavioral predictors for the odor stimulus-presentation epoch are supported over the window 0 to 500 ms relative to the onset of odor valve, as well as late phase of odor-sampling epoch that are supported over the window 0 to 553/264 ms relative to the offset of odor valve in either go/no-go trials (median of the valve offset to odor port exit), and pre odor port exit epoch that are supported over the window -300 to 0 ms relative to the odor port exit. Inset, predicted and actual averaged firing rate relative to the odor onset and odor port exit for one neuron.

(**B**) Top: relative contribution of each behavioral variable to the explained variance of the neural activity, averaged across the go-cue-selective neurons. All error bars represent the standard error of the mean. Bottom: relative contribution significance of the late phase of go-cue odor-sampling variable.

(**C**) Go-cue odor-preferred responses during correct trials, error trials, and catch (odorless) trials. The auROC values were calculated during the odor-sampling epochs and only neurons with a minimum number of three trials for each analyzed condition were included in this analysis. Black horizontal lines and black vertical lines indicate medians and interquartile ranges. The statistical significance among five groups (*$p < 0.05$, **$p < 0.01$, ***$p < 0.001$) was assessed by one-way analysis of variance (ANOVA) with Tukey's post hoc test.

(**D**) The development of go-cue responses in go-cue-selective neurons during learning. For each go-cue-selective neuron, we calculated the correlation between the firing rate during the go-cue odor-sampling epoch relative to the baseline (a mean firing rate during inter trial interval was subtracted for each neuron) and the order of go trial from the start of the session. The correlation coefficient was compared with control values calculated by the 1000 trial-shuffled data (gray shaded area) and then the statistical significance was determined (< 0.5th percentiles of the control values, negative correlation; > 99.5th percentiles of the control values, positive correlation). Across go-cue-selective neurons, many of the go-cue responses were not correlated with trial progression (86.0%, not significant; 7.0%, negative; 7.0%, positive).

6.5. Results: Response dynamics of the ACo neuron population during the late phase of odor-sampling epoch

We demonstrated that ACo neurons showed odor-evoked cue-preferred responses during the late phase of the odor-sampling epoch. Were the distinct cue responses reflected in the ACo neuron population dynamics, and how much could the population activity account for animals’ behavioral accuracy? First, to gain insight into the dynamics of the population response, we visualized average population activity using principal component analysis, a dimensionality reduction method. **Figure 6-3A** shows trajectories of the mean response of the ACo neuron population to go-cue and no-go-cue odors, represented as projections onto the first three PCs during the odor-sampling epochs. Throughout the approximately 400 ms interval from the odor onset, trajectories remained converged, showing little difference across conditions. Over the late phase of odor-sampling epochs, trajectories in the odor-sampling epoch subspace began to spread out and were clearly separated at the population level. To quantify these observations, we measured the instantaneous separation between the population cue responses (**Figure 6-3B**). The separation started to increase from 400 ms after odor onset, reaching a maximum at ~800 ms, and remained above baseline levels until odor port exit. Thus, the ACo neuron population showed profound and persistent transformations in the dynamics of cue-encoding, 400 ms after odor onset.

Second, to examine whether the population activity accounted for the animals' behavioral accuracy, we performed a decoding analysis to determine whether the firing rates of the ACo neuron populations could be used to classify each individual trial as go or no-go. We used SVMs with linear kernels as a decoder. Based on ACo neurons, analyses of the decoding time course, using a sliding time window, revealed that decoding accuracy was first maintained at chance levels 400 ms after the odor onset, and then increased above the behavioral accuracy level of the animals around 500–600 ms after odor onset (the top-right graph in **Figure 6-3C**). In the 700–800 ms period, about 100 neurons provided sufficient information to account for the behavioral accuracy (the bottom right graph in **Figure 6-3C**). Thus, a hundred ACo neurons accounted for animals' behavioral accuracy in the late phase of odor sampling.

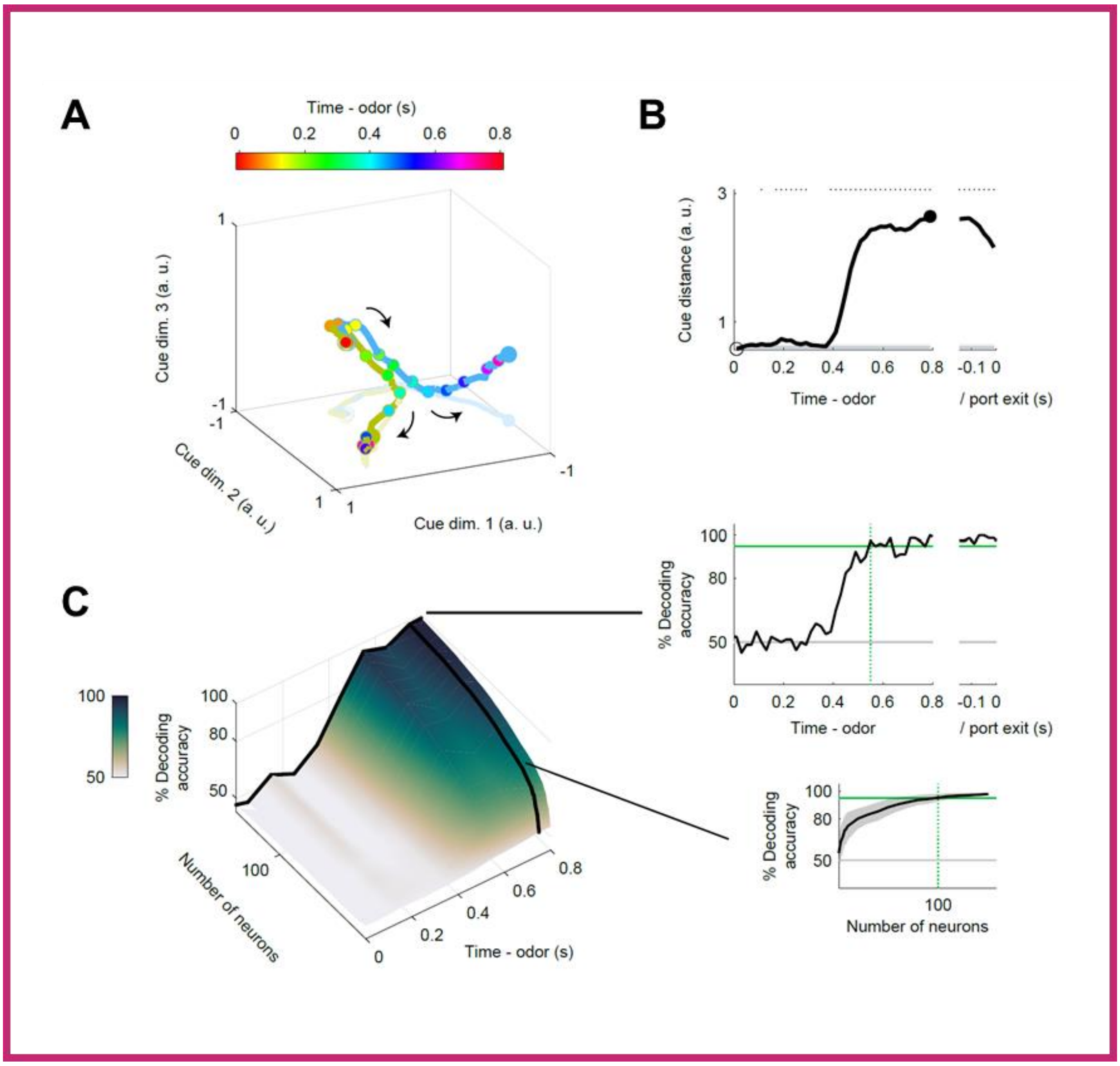

Figure 6-3 | Dynamics of ACo neuron population response during the late phase of odor-sampling

(**A**) Visualization of ACo neuron population responses during odor-sampling epoch using principal component analysis (158 neurons). The responses to cue odors are projected onto the first three PCs corresponding to odor-sampling epoch subspaces. Blue line, go-cue odor; green line, no-go-cue odor. Temporal progression from unfilled blue/green spheres to filled spheres.

(**B**) Distance between ACo neuron population responses. Gray line and shaded area show mean ±2SD baseline values during pre-odor-sampling epoch. Top dots indicate time bins showing values more than mean +2SD baseline values.

(**C**) The time course of odor decoding accuracy. A vector consisting of instantaneous spike counts for 1–158 neurons in a sliding window was used as input for the classifier. Training of the classifier and testing were done at every time point. Green horizontal lines indicate the level of animal behavioral performance. Gray horizontal lines indicate chance level (50%). Green vertical dashed lines indicate the first points at which the decoding accuracy reached the level of animal behavioral performance. Shaded areas represent ±SD.

6.6. Results: Two types of reward anticipation responses of ACo neurons

We then focused on the ACo activity during odor-evoked behaviors after an odor-sampling epoch. A subset of ACo neurons gradually increased their firing rates from the time of water port entry till the reward was received, and another subset of neurons increased their firing rates while waiting for reward (examples shown in **Figure 6-4A**). We quantified the data by calculating firing rate changes from baseline (spike data were aligned to the water port entry), and three measures from the values: “time of center of mass”, “onset time”, and “duration” (from water port entry to 1000 ms after opening the water valve, **Figure 6-4B**). The drinking epoch selective neurons ($n = 30$, 19.0 % of the recorded neurons) were defined as neurons that had the time of center of mass during the drinking epoch, and the waiting epoch selective neurons ($n = 14$, 8.9 % of the recorded neurons) were defined as neurons that had the time of center of mass during the waiting epoch. Across the population, the drinking-epoch-selective neurons gradually increased their firing rates -190 ms before the water valve opened for 432 ms, and the waiting-epoch-selective neurons increased their firing rates 10 ms after water port entry for 108 ms (**Figures 6-4C-D**, $p < 0.01$, permutation test). Thus, ACo neurons exhibited two distinct types of reward anticipation responses.

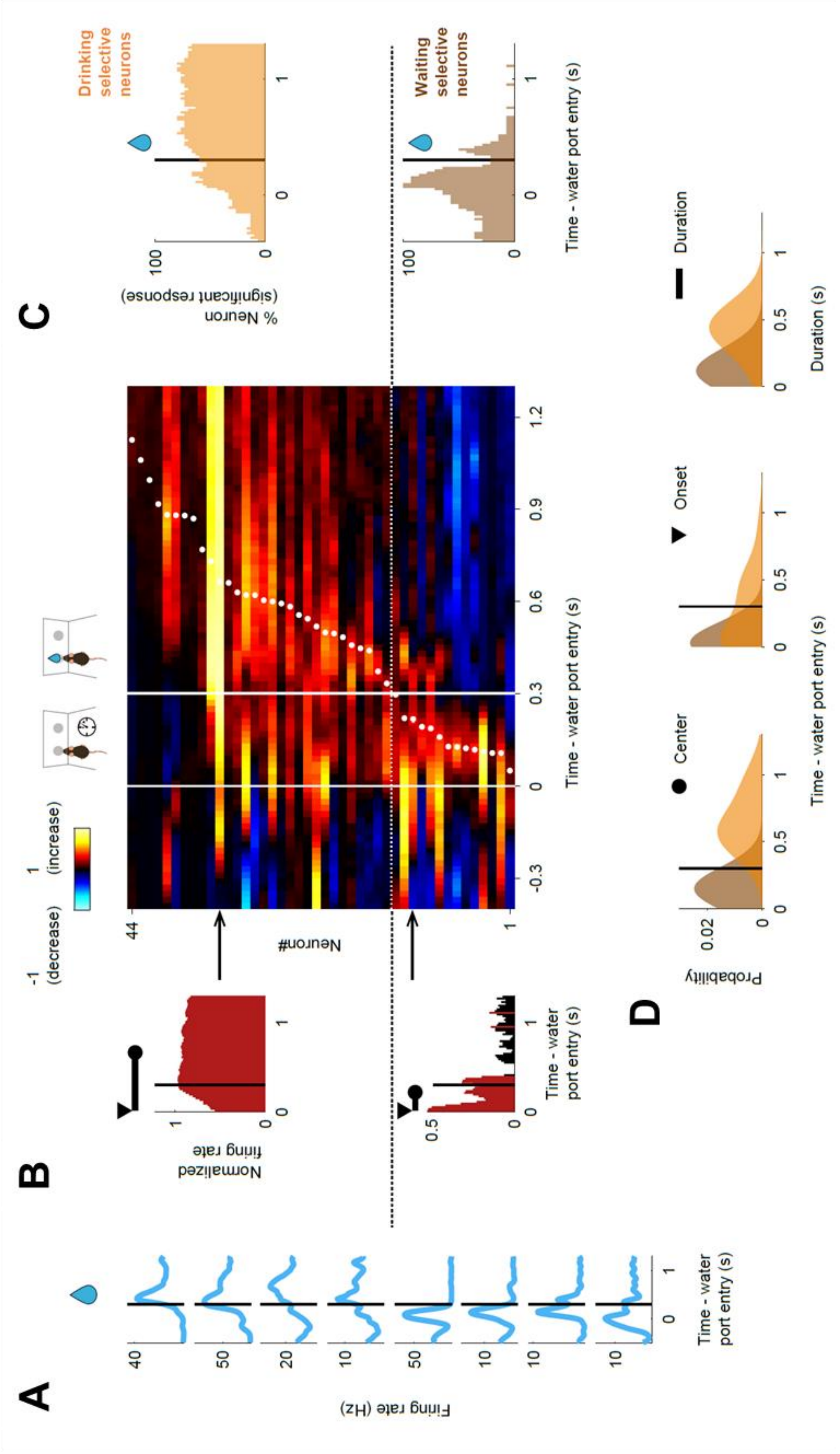
A
Firing rate (Hz)
40
50
20
10
50
10
10
10
0
1
Time - water port entry (s)
B
Normalized firing rate
1
0
0.5
0
1
Time - water port entry (s)
-1 (decrease)
1 (increase)
Neuron#
44
1
-0.3
0
0.3
0.6
0.9
1.2
Time - water port entry (s)
C
% Neuron (significant response)
100
0
Drinking selective neurons
Waiting selective neurons
0
1
Time - water port entry (s)
D
Probability
0.02
0
Center
Onset
Duration
0
0.5
1
Time - water port entry (s)
Duration (s)

Figure 6-4 | Two types of reward-related responses of ACo neurons

(**A**) Example firing patterns of reward-related responses. A vertical black line indicates the water valve opening.

(**B**) Evaluation of the reward-related responses. auROC values were calculated by go-behavior versus baseline in the sliding bins. Left: red bars show significant excitation ($p < 0.01$, permutation test). Based on the significant time points, onset time (black triangle), time of center of mass (black circle) and duration (black horizontal line) were calculated. Vertical black lines indicate the water valve opening. Right: each row corresponds to one neuron and neurons are sorted by times of center of mass (white dots) of auROC values. Based on the times of center of mass, drinking-selective neurons and waiting-selective neurons were defined (a horizontal dashed line). Color scale as in **Figure 6-1D**. Vertical white lines indicate the water port entry and the water valve opening.

(**C**) The proportions of neurons that exhibited a significant response, calculated from auROC values ($p < 0.01$, permutation test) for each neuron group (orange, drinking selective neurons; brown, waiting selective neurons).

(**D**) Distributions of the times of center of mass, onset times and durations (orange, drinking-selective neurons; brown, waiting-selective neurons).

6.7. Results: Association of go-cue excitations with excitatory responses for the reward anticipation behavior

We observed that the waiting-epoch-selective neurons showed go-cue-preferred activity during the odor-sampling epoch; however, the drinking-epoch-selective neurons did not (examples shown in **Figure 6-5A**). To examine the relationship between the reward anticipation responses and cue encoding, we quantified the response profiles of each neuron group during odor-evoked behaviors by calculating the firing rate changes from baseline (**Figure 6-5B**). Across the population, drinking-epoch-selective neurons showed significant excitatory responses for the waiting and drinking epochs (red histogram at the top in **Figure 6-5B**, $p < 0.01$, permutation test), and significant inhibitory responses for other behavioral epochs (blue histogram at the top in **Figure 6-5B**, $p < 0.01$, permutation test). Alternatively, waiting-epoch-selective neurons showed significant excitatory responses for the late phase of go-cue odor-sampling and waiting epochs (red histogram at the bottom in **Figure 6-5B**, $p < 0.01$, permutation test), and significant inhibitory responses for the drinking and no-go waiting epochs (blue histogram at the bottom in **Figure 6-5B**, $p < 0.01$, permutation test). The waiting-epoch-selective neurons showed higher responses during the go-cue odor-sampling epoch than those of other groups (**Figure 6-5C**, one-way analysis of variance with Tukey’s post hoc test). Thus, waiting-epoch-selective neurons exhibited associations between the go-cue excitations and excitatory responses for waiting behavior, suggesting that a subset of ACo neurons was involved in cue-outcome associations.

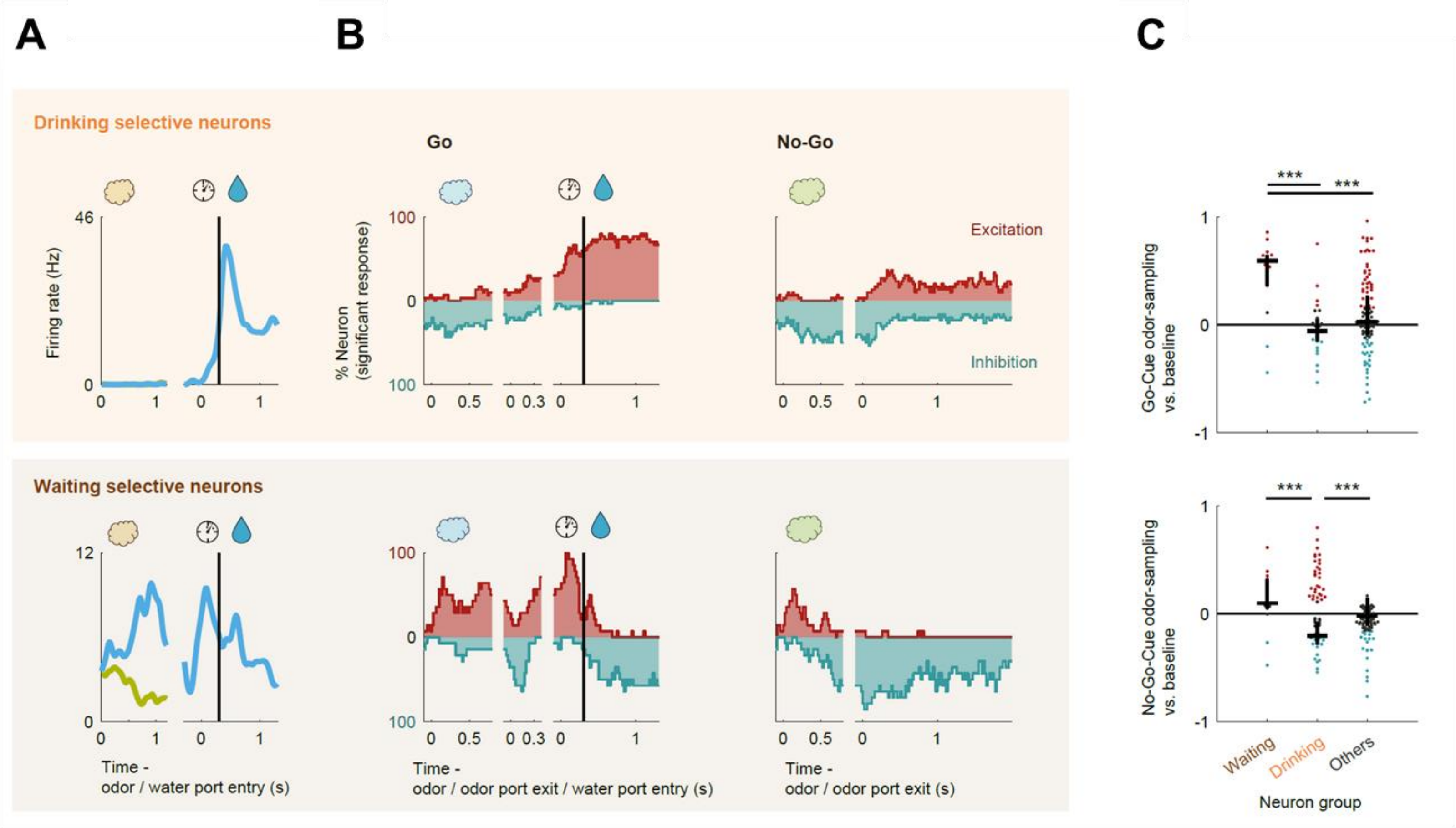
A
B
C
Drinking selective neurons
Waiting selective neurons
Firing rate (Hz)
46
12
0
0
1
0
1
Time -
odor / water port entry (s)
Go
No-Go
% Neuron
(significant response)
100
0
100
0
0.5
0
0.3
0
1
Excitation
Inhibition
Time -
odor / odor port exit / water port entry (s)
Time -
odor / odor port exit (s)
Go-Cue odor-sampling
vs. baseline
No-Go-Cue odor-sampling
vs. baseline
1
0
-1
***
***
Waiting
Drinking
Others
Neuron group

Figure 6-5 | Waiting-selective neurons showed go-cue odor-preferred responses during odor-sampling

(**A**) Example firing patterns of cue-outcome responses. A vertical black line indicates the water valve opening.

(**B**) The proportions of neurons that exhibited significant excitatory and inhibitory response calculated from auROC values ($p < 0.01$, permutation test) for each neuron group.

(**C**) auROC values during odor-sampling epoch of go-cue odor-selective responses (top graph) and no-go-cue odor-selective responses (bottom graph) for each neuron group. Black horizontal lines and black vertical lines indicate medians and interquartile ranges. Red dots, significant excitation; blue dots, significant inhibition; gray dots, non-significant ($p < 0.01$, permutation test). Statistical significance among three groups (***$P < 0.001$) was assessed by one-way analysis of variance (ANOVA) with Tukey’s post hoc test.

6.8. Discussion: Insights based on the results

The purpose of the study was to understand the electrophysiological features of ACo neurons on odor-evoked reward-related behavioral tasks. We found that many ACo neurons exhibited go-cue odor-preferred responses at the late phase of the odor-sampling epoch (**Figures 6-1 and 6-2**). Consequently, the ACo population showed profound and persistent transformations in the dynamics of cue encoding and provided sufficient information to account for the behavioral performance before executing the odor-evoked behaviors (**Figure 6-3**). In addition to the late phase of odor-evoked activities, we also found two types of reward anticipation signals during the odor-evoked behaviors: ramp-like gradual increases in the signals to the reward exhibited by drinking-epoch-selective neurons, and phasic anticipation signals exhibited by waiting-epoch-selective-neurons (**Figure 6-4**). The waiting-epoch-selective neurons exhibited associations between the go-cue excitations and excitatory responses for the waiting behavior (**Figure 6-5**). Thus, the ACo showed unique encodings during various behavioral states in the task, suggesting that the ACo neurons play an important role in reward-related learning evoked by olfactory stimulus.

The ACo was a previously unexplored area in the olfactory amygdala located caudally to the lateral olfactory tract and rostromedially to the posterolateral cortical nucleus of the amygdala. Neural tracing studies showed that the projection from the OB terminates in the outer portion of the most superficial layer (layer Ia) of the cortex, and the projection from other olfactory cortex areas terminates in the deep portion of the ACo (Carmichael et al., 1994; Scalia and Winans, 1975). We found using an electrophysiological approach that ACo neurons exhibited cue-odor-preferred responses at the late phase of odor-sampling epochs. The peak firing in ACo neurons during odor-sampling epochs was later than that in other olfactory cortical areas (e.g., the piriform cortex (Miura et al., 2012); and the ventral tenia tecta (Shiotani et al., 2020b)). This late phase coding in the ACo neurons was not the premotor signal (**Figure 6-2**). This may reflect the input of other olfactory cortex from layers Ib, II, and III, and the top-down inputs from other brain areas, rather than the direct sensory inputs from OB in layer Ia. Therefore, we speculate that ACo neurons send task-modulated olfactory information to other amygdala areas.

6.9. Discussion: Two types of reward-related responses that are unique properties of the ACo

Since the ACo sends many axons to the basolateral amygdaloid complex (BLA) (Cádiz-Moretti et al., 2017) which plays a role in learning and memory of the CS-US association

(Gore et al., 2015), this projection is thought to carry olfactory information for the CS-US association in the odor-guided learning task. Given that the ACo receives direct input from the BLA (Cádiz-Moretti et al., 2017), our finding that the type of ACo activity that shows go-cue-odor preference with increased activity in the reward anticipation epoch (**Figure 6-5**, “waiting selective neurons”) may play a role in the CS-US association by linking olfactory information with reward anticipation. In addition, a previous study revealed that pyramidal neurons of the ACo displayed rhythmic fluctuations of the intrinsically generated voltage-dependent membrane potential in the theta-low beta range with the activation of sodium conductance (Sanhueza and Bacigalupo, 2005). Increased synchronization of theta oscillations between regions, important for enhanced communication during memory acquisition and goal selection (Benchenane et al., 2010; Hoffmann and Berry, 2009; Jones and Wilson, 2005), is observed between the lateral olfactory entorhinal cortex (LEC) as a part of the olfactory cortex and the hippocampus during the learning phase of the CS-US associative learning task (Takehara-Nishiuchi et al., 2012). Taking these evidence together with the fact that ACo has a bidirectional connection with the LEC (Cádiz-Moretti et al., 2017), we speculate that the ACo additionally drives the LEC-HPC circuit and supports the CS-US association by synchronizing the ACo-LEC-HPC theta oscillations during the learning stage.

A subset of ACo neurons started to increase their firing rate before the drinking epoch and these activities persisted during the epoch (**Figures 6-4 and 6-5**, “drinking selective neurons”). Previous studies reported that similar firing patterns were observed in the dopamine neurons in the VTA (Kim et al., 2020; Song and Lee, 2020). After learning, dopamine activity may change phasic responses to cues and rewards, and ramping activity may arise as the agent approaches the reward. Given that the ACo receives direct projections from the VTA (Cádiz-Moretti et al., 2017), it is assumed that the ramping-like response in the ACo may reflect the inputs from the VTA. In addition, ACo has anatomical connections with other olfactory cortices (Cádiz-Moretti et al., 2017). We speculate that the VTA reward signals may be transmitted to other olfactory cortical areas via ACo, making learning more efficient in the olfactory cortex. Finally, a previous behavioral study revealed that electrical stimulation of the VTA showed that the ACo, besides other mesolimbic structures, displayed increased Fos expression in rats (Majkutewicz et al., 2010). ACo sends excitatory glutamatergic/aspartatergic projections to the nucleus accumbens (NAc) (Ray et al., 1992). Dopamine projections from the VTA to the NAc, which constitute the mesolimbic dopamine system (Björklund and Dunnett, 2007; Ikemoto, 2007; Morales and Margolis, 2017), play an essential role in motivated behaviors, reinforcement learning, and reward processing (Hamid et al., 2016; Watabe-

Uchida et al., 2017). Therefore, the ACo may assist in driving the NAc-VTA circuit for reward-related behavior.

Chapter 7. General Discussion

7.1. “Odor-functions map” hypothesis in the OC

In this doctoral dissertation, I summarized the research on the OC subregions aPCx, vTT, NLOT, and ACo, in which distinct neural spike activity patterns were recorded by extracellular recordings in each region during odor-guided tasks (**Figures 7-1 and 7-2**). Based on the general idea that different brain regions have different functional features consistent with their electrophysiological features, as well as the traditional theory on the localization of brain functions, we propose the hypothesis that different subregions of the OC have different electrophysiological and functional features, forming an “odor-functions map”. In the 30-year history of olfaction research, since the finding of odorant receptors in 1991 (Buck and Axel, 1991), the existence of an “odor-molecular map” in the olfactory bulb had been revealed (Igarashi et al., 2012), and we now consider the next generation hypothesis that there is possibly the “odor-functions map” in the OC as reasonable, consistent with the knowledge that there is no topographical map based on odorant molecular profiles in the OC (Miura et al., 2012; Rennaker et al., 2007; Stettler and Axel, 2009; Uchida et al., 2014; Zhan and Luo, 2010). Given the idea that the OC processes sensory information in different subregions for each kind of functional meaning of odor and leads to the function of inducing behavior, we may shed a new light on the process of translating odor molecular information into odor-evoked behavioral information in olfactory neural circuits.

In the aPCx, which is the most studied OC, in addition to the traditional distributed odor information representation patterns (Miura et al., 2012; Stettler and Axel, 2009), various behavioral state response patterns were observed, such as those related to the association between odor information and the animal's behavioral state (**Figures 3-2 and 3-3**). Since the aPCx is the largest region in the OC and has connections with all OC subregions (Luskin and Price, 1983b), one of the anatomical features of the region is that it receives and mixes a variety of top-down information with a wide variety of odor information, which is consistent with our results. Furthermore, although the response properties of individual neurons are diverse and learning-dependent (**Figure 3-3**), the results that odor discrimination capabilities and odor-outcome associations are maintained at the population level (**Figure 3-4**) are consistent with the drift representation of the aPCx during odor representation (Schoonover et al., 2021) and extends the characteristics of the region, supporting our hypothesis from the point of view that it may represent a functional profile of the aPCx in the OC.

Where does the behavioral state signal that characterizes the response pattern of the aPCx come from? The first candidate source of input is a direct projection from the frontal cortex to the OC (Johnson et al., 2000). This possibility has been shown in previous studies (Calu et al., 2007; Roesch et al., 2006), but future studies will need to prove this causal relationship by applying pathway-specific optogenetic approaches. Another candidate input source is the projection pattern from the mPFC to the OC wide area via the vTT (**Figure 4-4**) (Shiotani et al., 2020b). Individual neurons in the vTT show various behavioral state signals in transient firings as a characteristic of the region (**Figure 4-2**), and we have proposed that the vTT is an ideal region as a hub to supply behavioral state signals to the OC wide area. Supporting our idea based on the anatomical background and electrophysiological features, optogenetic inhibition of the mPFC-to-vTT input reduced the behavioral state representation of the vTT (**Figure 4-5**). These results indicate that at least the mPFC-to-vTT input contributes to the behavioral state representation of the vTT and suggest that higher-order information is supplied from the frontal cortex to the OC, where different information processing takes place based on the anatomical characteristics of the OC subregions.

Supporting this idea, characteristic electrophysiological features were observed in the NLOT, which is closely related to the amygdala that is particularly involved in the stimulus-reward association. NLOT neurons that selectively responded to go-cue odor also responded during reward acquisition, thereby contributing to association learning (**Figure 5-7**). Similarly, in the ACo, which is closely related to the amygdala and located next to the NLOT, characteristic reward expectation and reward responses were observed that contribute to reward-based learning (**Figure 6-5**). We propose a circuit model in which behavioral state signals are supplied to the OC, and each subregion plays a different role in the formation of an “odor-functions map” based on the functions that guide behavior.

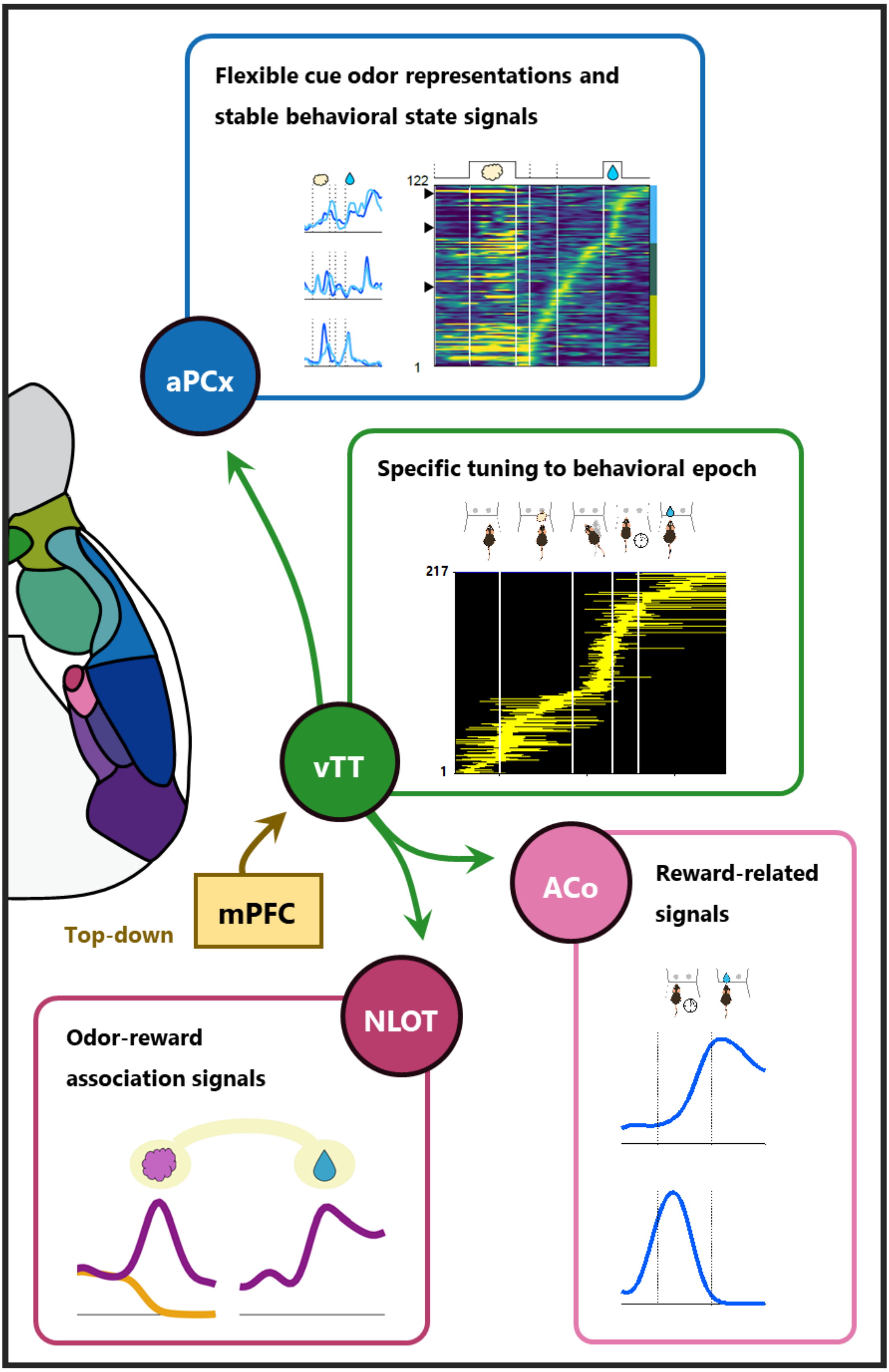
Flexible cue odor representations and stable behavioral state signals
122
1
aPCx
Specific tuning to behavioral epoch
217
1
vTT
mPFC
Top-down
ACo
Reward-related signals
NLOT
Odor-reward association signals

Figure 7-1 | Summary: “Odor-functions map” hypothesis in the OC

In this doctoral dissertation, I summarized the research on the OC subareas aPCx, vTT, NLOT, and ACo, in which distinct neural spike activity patterns were recorded by extracellular recordings in each region during odor-guided tasks. The aPCx neurons responded to a specific combination of cue odors with increased firings during a specific state of the subsequent behaviors (**Chapter 3**). We hypothesized that not only the aPCx but also the other subareas have their own unique top-down signal processing. As one of the candidate sources of the top-down signals, we next focused on the vTT, which receives top-down projections from the mPFC and projects to the broad olfactory areas (**Chapter 4**). We found that individual vTT neurons tuned to a specific behavioral state, and the vTT state representations were degraded with optogenetic inactivation of the mPFC-to-vTT inputs. To investigate how such top-down inputs to the OC are distributed to the subareas, we finally focused on the NLOT and ACo. Many NLOT neurons that selectively responded to go-cue odor also increased their firing rates during drinking reward, suggesting that the NLOT is involved in odor-reward association learning (**Chapter 5**). On the other hand, ACo neurons exhibited two types of reward anticipation signals: one neuron group type exhibited gradual increases in the signals to the reward, while the other type showed phasic anticipation signals, suggesting that the ACo is involved in odor-guided reward-directed learning (**Chapter 6**). In conclusion, we propose a circuit model in which behavioral state signals are shared to the OC, and each subarea plays a distinct role in the formation of an “odor-functions map” based on the functions that lead to odor-evoked behaviors.

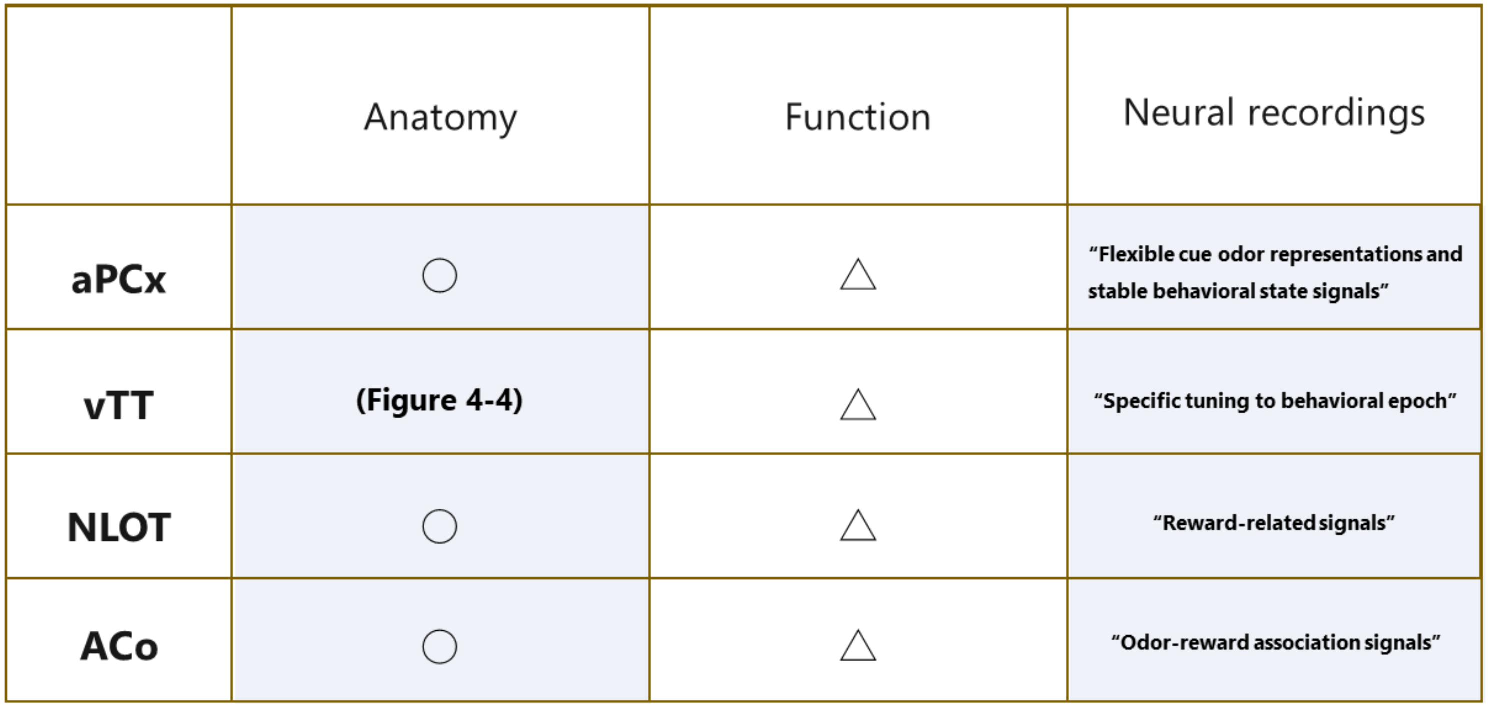

	Anatomy	Function	Neural recordings
aPCx	○	△	**“Flexible cue odor representations and stable behavioral state signals”**
vTT	**(Figure 4-4)**	△	**“Specific tuning to behavioral epoch”**
NLOT	○	△	**“Reward-related signals”**
ACo	○	△	**“Odor-reward association signals”**

Figure 7-2 | The accumulation of knowledge about anatomy, function, and neural recordings in the aPCx, vTT, NLOT, and ACo

Well-researched fields are shown by the blue shaded area, based on this thesis. The direction of future research is to examine how the top-down input to the OC is distributed to each subarea and how it is involved in unique information processing and the function.

7.2. Anatomical evidence for the “odor-functions map” in the OC

It was shown that the OC has contacts with various higher-order regions (Johnson et al., 2000). Recently, it has been suggested that the PCx output neurons that project to different target regions are enriched at specific locations along the A-P axis by using high-throughput single-neuron projection mapping techniques, Multiplexed Analysis of Projections by sequencing and Barcoded Anatomy Resolved by sequencing (Y. Chen et al., 2021). They also found that inputs from the OB correlated with specific PCx output projections that varied along the A-P axis. For example, OB inputs to the anterior olfactory nucleus were stronger in neurons that also innervated more strongly the aPCx than those projecting more strongly to the posterior piriform cortex (pPCx). Conversely, OB inputs to the cortical amygdala (CoA) and lateral entorhinal cortex (LEC) were correlated with strong projections to the pPCx. That is, they demonstrated that these gradients are matched: OB neurons targeting a specific location within the PCx co-innervate extra-piriform regions that receive strong inputs from the PCx neurons. Since CoA and LEC are closely related to behavior (photostimulation of odor-responsive CoA neurons induces specific behaviors that recapitulate innate attractive or aversive responses (Root et al., 2014)), the role of the projection system from the OB through each subregion may be determined not by the physical properties of the odorant molecules, but by the properties associated with the function and behavioral output system of the projected region.

Given the unique input-output patterns of the olfactory circuits described above, it appears that the behavioral state signals observed among the OC subregions have unique properties perhaps reflecting anatomical and common properties. For example, while all behavioral state signals were commonly represented in all subregions, the vTT encodings uniquely covered behavioral state signals all over in a transient response pattern (**Figure 4-2**) that seemed to reflect behavioral state inputs from the mPFC (Hyman et al., 2012). The NLOT encoded the association between odor and reward responses (**Figure 5-7**) as observed in reward-related regions (Cohen et al., 2012; Menegas et al., 2017; Stephenson-Jones et al., 2020) and the ACo encoded reward-related signals (**Figure 6-5**) such as dopaminergic ramping responses (Kim et al., 2020; Song and Lee, 2020). The unique signals of each subregion are thought to reflect the input or output factors used for computation in the reward and motivation systems in which each region participates. In contrast, the behavioral state signals observed in all subregions may be caused by state information-sharing mechanisms from higher regions to the sensory cortex, such as the mPFC-to-vTT input (**Figure 4-5**). Such a phenomenon is thought to be one of the basic principles of brain information encoding shared by the whole brain and has similarities with the recently reported brain-wide sharing of animal movement-related signals (Musall et al., 2019; Parker et al., 2020; Steinmetz et al., 2019; Stringer et al., 2019). Although specific optogenetic suppression of this motor-related signal did not affect the behavioral choices of the animals, suppression of the unique properties of the visual cortex for visual sensory processing disrupted the behavioral output (Zatka-Haas et al., 2021). However, motor-related signals can affect behavioral output in situations where it is necessary to distinguish between signals produced by oneself and from external sources, or in situations involving higher-order processing such as attention (Parker et al., 2020; Speed and Haider, 2021). Based on the above, it is necessary to carefully describe which parts of the observed neural activity elements are shared elements and which parts are unique elements, including causal relationships. This issue is one of the challenges of the present times when large-scale neural activity recording and systematic optogenetic neural manipulation are now possible.

Notably, the shared and unique properties were also observed in the olfactory system, implying that the olfactory system is an ideal model system to investigate the basic principles of state information sharing in the brain starting from the sensory input. This is because the olfactory system has anatomical characteristics that allow direct sensory bottom-up input from the olfactory bulb to the olfactory cortex without involving the thalamus, as well as a simple structure that allows direct top-down input from higher-order areas such as the frontal cortex. It has therefore the advantage that the correspondence between bottom-up and top-down communication can be easily clarified. In the future, I would like to develop an “odor-functions map” in the OC and explore the future of olfaction research, using the olfactory system as a model to clarify the shared and unique properties of the state signals observed in the whole brain.

7.3. Limitations and future direction

We acknowledge that there are several limitations to our studies. First, although we performed the first in vivo recording of neuronal activity in some OC subregions during only a simple odor-guided go/no-go task, our data do not reflect the neuronal activity across different cue modalities, behavioral paradigms, and contexts, which would account for multidimensional behavioral states. To understand the shared and unique properties of neural activity in each OC subregion in multiple aspects, it is necessary to develop behavioral tasks that quantify other behavioral states, such as motivational states in positive and negative stimulus-outcome learning (Stephenson-Jones et al., 2020; Zhang et al., 2021), and internal state changes including arousal and sleep states (Manabe et al., 2011). For example, behavioral tasks using the elevated plus maze (Gründemann et al., 2019; Hagihara et al., 2021; Yoshihara et al., 2021) and odors that elicit innate aversive behaviors (Root et al., 2014) are effective for understanding properties with an axis of negative and aversive behaviors. Meanwhile, since the factors that contribute to neural activity in situations where animals can move freely are complex, quantitative assessment and comparison of neural activity using a head-fixation task with restricted movement is also necessary. Comparing the activity during passive classical conditioning and active decision-making contexts improves our understanding of activity properties with behavioral freedom as the axis. To investigate learning as an axis of activity properties applied to behavioral tasks, task design that focuses on the learning process (Takamiya et al., 2021), and reversal learning (Ramesh et al., 2018) or set-shifting paradigms (Spellman et al., 2020) that change the relationship between stimuli and outcomes are effective. In this learning process, the axes related to the animal's perception and interpretation of the sensory stimuli are revealed by the context in which the difficulty of the stimuli to determine the behavior gradually changes (Miura et al., 2012), the context in which categorization of multiple stimuli is required (Reinert et al., 2021), and the context in which the same behavior is derived from multisensory stimuli (Ohnuki et al., 2020). To further examine axes related to changes in internal states in response to stimuli, tasks that measure the animal's confidence in its behavioral choices (Hirokawa et al., 2019; Kepecs et al., 2008), quantify the relationship between confidence and memory (Joo et al., 2021), evaluate internal states that change with the behavioral choice situation (Osako et al., 2021), evaluate the evidence accumulation for stimuli (Hanks et al., 2015), and evaluate working memory (Wang, 2021) and economic choice (Gardner et al., 2020) for stimuli are effective. Moreover, the task-related activity axes focused on in our study for time and place can be clarified in the context of freely exploring rewards in real mazes (Takahashi, 2015) and VR environments (Nieh et al., 2021; Radvansky et al., 2021), together with tasks that assess the neural coding of the absolute and relative time (Shimbo et al., 2021). Finally, it is necessary to introduce techniques for detailed analysis of animal behavior using deep learning (Mathis et al., 2018) and techniques for systematic quantification of various behavioral parameters (body movement (Parker et al., 2020), pupil (Cazettes et al., 2021; Lee et al., 2020), facial expression (Dolensek et al., 2020), respiration (Kepecs et al., 2007)) to define behavioral states in more detail. Considering these things, the future challenge is to design behavioral paradigms that allow us to observe external and internal variables for multiple aspects at once, and to the systematically reveal neural properties from lower-order to higher-order parameters of the OC subregion one by one in sequence. However, our data are potentially important in that OC subregions neural activity in freely behaving rodents is modulated by the odor-guided behaviors and may provide basic information regarding OC encoding in various behavioral contexts.

Second, in parallel with investigating the electrophysiological features of each OC subregion as described above, we need to clarify the pathway-specific functional features in comparison with them and break away from studies that simply collect the neural response profiles. To tackle this issue, it is necessary to investigate the function of individual subregions based on anatomical and electrophysiological findings. Specifically, we need to consider an experimental design that can quantify the behavioral changes that occur when each circuit is disrupted. For instance, the legion experiment of the NLOT has been reported to show olfactory behavioral disturbances (Vaz et al., 2017), while neural projections of the NLOT to different regions in different layers have been reported (Santiago and Shammah-Lagnado, 2004). Therefore, it is necessary to clarify the circuit structure and function spreading around the OC subregions by using genetic methods such as Cre-mice to reveal the function of each projection more specifically. Furthermore, to demonstrate that the vTT functions as a hub that supplies behavioral state signals within the OC, it is necessary to examine the effects on odor learning in animals when the mPFC-to-vTT pathway is suppressed, together with other subregional neural activity changes. Tools for probing pathway-specific neural activity in these deep brain regions include electrophysiological tagging techniques (Cohen et al., 2012; Hirokawa et al., 2019), fiber photometry (Matias et al., 2017), endoscope (Gründemann et al., 2019; Yoshizawa et al., 2018), and imaging techniques using a prism (Spellman et al., 2020). Finally, it is a major goal of our research to elucidate the details of olfactory neural pathways related to flavor sensation (Shepherd, 2006), as a target for the study of higher-level olfactory functions. Understanding the structure and function of the orthonasal and retronasal pathways (Shepherd, 2011) will also lead to a better insight into the food sensation and subjective functional aspects of the integration of olfactory and other sensory information. Thus, based on the electrophysiological and anatomical data we have obtained, it is important to clarify the causal relationship between the function of each OC subregion and neural activity in a pathway-specific manner and to develop a more detailed "odor-functions map" in the OC at the neural circuit level.

Third, analysis techniques that can properly evaluate the large-scale data collected need to be further developed with integration to other research fields. For example, in precisely comparing neural properties across regions, the approach of computing neural manifolds for responsive properties (Ebitz and Hayden, 2021) may be effective in comparing properties of each OC subregion at the population level. Using this analysis to test whether subregion-specific neural representations can be shared and complemented across animals (H.-T. Chen et al., 2021; Rubin et al., 2019) is a useful method for refining hypotheses and building neural circuits models. Furthermore, it would be useful to develop an OC circuit and computation model, which considers that vTT is the hub providing behavioral state signals within the OC. It provides an opportunity to deepen the mathematical aspects of the hypothesis, discuss it with outstanding research teams working on theory building, and expand the community. Beyond these connections with research in other fields, we can expect to see links with research on neural systems at the micro-scale (Iwata et al., 2019), research on primates (Sadakane et al., 2015), humans at the macro-scale, and brain-machine interface (BMI) and pathology research. In particular, the symptoms of COVID-19, which have posed a threat and challenge to human beings from the beginning of December 2019 until now in 2021, are also closely related to the olfactory system, and therefore provide significance for the olfactory research. With such a broad perspective, it is crucial to promote the development of phenomena and theories and to clarify the “odor-functions map” in the OC.

In conclusion, I believe that the approach described above can be applied not only to olfaction but also to other sensory cortices and help to reveal basic principles common to the whole brain. I am currently considering that the technologies that will be important for clarifying the problem are 1) large-scale electrophysiological and imaging data acquisition technologies that also provide long-term recording (Ota et al., 2021; Steinmetz et al., 2021; Stringer et al., 2021), and 2) technologies that allow neural manipulation of single cells to specific cell populations on a precise spatiotemporal activity scale (Adesnik and Abdeladim, 2021; Carrillo-Reid et al., 2019; Daie et al., 2021; Dalgleish et al., 2020; Gill et al., 2020; Jennings et al., 2019; Marshel et al., 2019; Okada et al., 2021; Robinson et al., 2020). For 1), it will enable us to study new aspects of neuroscience that have not been seen on a traditional scale, and it will also be necessary for researchers to provide large-scale data that is consistent not only with the surface of the brain but also with deeper regions such as the olfactory, reward, and emotional systems. For 2), neural manipulation on the spatiotemporal activity scale, we can study not only the manipulation of specific projection pathways, but also the overlap of spatial local circuits and activities that affect each other in a chain. For example, for the behavioral state responses of the OC found in our study, it is possible to artificially manipulate only the population of neurons that exhibit a particular state activity to test the causal relationship with the function. Since the manipulation of temporal activity patterns at the level of single cells is an unexplored field for neuroscientists, the combined manipulation of the spatiotemporal activity patterns of neural circuits may enable the identification of the Hebbian rule, the identification of memory engrams (Josselyn et al., 2015; Tonegawa et al., 2018) at the level of milliseconds, and the transfer of the neural information written in the circuits between animals. I believe that such research may lead to a better understanding of why neurons represent information “in groups” (Sakurai et al., 2018) — for example, how many different types of information can be written in a circuit formed by a particular group of cells? It could lead to a new stage in neuroscience: reading and writing the specific population activity patterns, such as the state representations observed in the OC, and verifying how they correspond to the dynamics of behavioral output in animals.

References

Adesnik H, Abdeladim L. 2021. Probing neural codes with two-photon holographic optogenetics. *Nat Neurosci* **24**:1356–1366. doi:10.1038/s41593-021-00902-9

Allen WE, Chen MZ, Pichamoorthy N, Tien RH, Pachitariu M, Luo L, Deisseroth K. 2019. Thirst regulates motivated behavior through modulation of brainwide neural population dynamics. *Science* **364**:1–15. doi:10.1126/science.aav3932

Banerjee A, Parente G, Teutsch J, Lewis C, Voigt FF, Helmchen F. 2020. Value-guided remapping of sensory cortex by lateral orbitofrontal cortex. *Nature* **585**:245–250. doi:10.1038/s41586-020-2704-z

Benchenane K, Peyrache A, Khamassi M, Tierney PL, Gioanni Y, Battaglia FP, Wiener SI. 2010. Coherent Theta Oscillations and Reorganization of Spike Timing in the Hippocampal- Prefrontal Network upon Learning. *Neuron* **66**:921–936. doi:10.1016/j.neuron.2010.05.013

Björklund A, Dunnett SB. 2007. Dopamine neuron systems in the brain: an update. *Trends Neurosci* **30**:194–202. doi:10.1016/j.tins.2007.03.006

Buck L, Axel R. 1991. A novel multigene family may encode odorant receptors: A molecular basis for odor recognition. *Cell* **65**:175–187. doi:10.1016/0092-8674(91)90418-X

Cádiz-Moretti B, Abellán-Álvaro M, Pardo-Bellver C, Martínez-García F, Lanuza E. 2017. Afferent and efferent projections of the anterior cortical amygdaloid nucleus in the mouse. *J Comp Neurol* **525**:2929–2954. doi:10.1002/cne.24248

Calu DJ, Roesch MR, Stalnaker TA, Schoenbaum G. 2007. Associative encoding in posterior piriform cortex during odor discrimination and reversal learning. *Cereb Cortex* **17**:1342–1349. doi:10.1093/cercor/bhl045

Carlson KS, Gadziola MA, Dauster ES, Wesson DW. 2018. Selective Attention Controls Olfactory Decisions and the Neural Encoding of Odors. *Curr Biol* **28**:2195-2205.e4. doi:10.1016/j.cub.2018.05.011

Carmichael ST, Clugnet M-C, Price JL. 1994. Central olfactory connections in the macaque monkey. *J Comp Neurol* **346**:403–434. doi:10.1002/cne.903460306

Carrillo-Reid L, Han S, Yang W, Akrouh A, Yuste R. 2019. Controlling Visually Guided Behavior by Holographic Recalling of Cortical Ensembles. *Cell* **178**:447-457.e5. doi:10.1016/j.cell.2019.05.045

Cazettes F, Reato D, Morais JP, Renart A, Mainen ZF. 2021. Phasic Activation of Dorsal Raphe Serotonergic Neurons Increases Pupil Size. *Curr Biol* **31**:192-197.e4. doi:10.1016/j.cub.2020.09.090

Chen H-T, Manning JR, van der Meer MAA. 2021. Between-subject prediction reveals a shared representational geometry in the rodent hippocampus. *Curr Biol* **31**:4293-4304.e5. doi:10.1016/j.cub.2021.07.061

Chen Y, Chen X, Baserdem B, Zhan H, Li Y, Davis MB, Kebschull JM, Zador AM, Koulakov AA, Albeanu DF. 2021. Wiring logic of the early rodent olfactory system revealed by high-throughput sequencing of single neuron projections. *bioRxiv* 2021.05.12.443929. doi:10.1101/2021.05.12.443929

Chu S. 2000. Odour-evoked Autobiographical Memories: Psychological Investigations of Proustian Phenomena. *Chem Senses* **25**:111–116. doi:10.1093/chemse/25.1.111

Cohen JY, Haesler S, Vong L, Lowell BB, Uchida N. 2012. Neuron-type-specific signals for reward and punishment in the ventral tegmental area. *Nature* **482**:85–88. doi:10.1038/nature10754

Cox J, Witten IB. 2019. Striatal circuits for reward learning and decision-making. *Nat Rev Neurosci* **20**:482–494. doi:10.1038/s41583-019-0189-2

Cury KM, Uchida N. 2010. Robust Odor Coding via Inhalation-Coupled Transient Activity in the Mammalian Olfactory Bulb. *Neuron* **68**:570–585. doi:10.1016/j.neuron.2010.09.040

Daie K, Svoboda K, Druckmann S. 2021. Targeted photostimulation uncovers circuit motifs supporting short-term memory. *Nat Neurosci* **24**:259–265. doi:10.1038/s41593-020-00776-3

Dalgleish HWP, Russell LE, Packer AM, Roth A, Gauld OM, Greenstreet F, Thompson EJ, Häusser M. 2020. How many neurons are sufficient for perception of cortical activity? *Elife* **9**:1–99. doi:10.7554/eLife.58889

Deitch D, Rubin A, Ziv Y. 2021. Representational drift in the mouse visual cortex. *Curr Biol* 1–13. doi:10.1016/j.cub.2021.07.062

Dolensek N, Gehrlach DA, Klein AS, Gogolla N. 2020. Facial expressions of emotion states and their neuronal correlates in mice. *Science* **368**:89–94. doi:10.1126/science.aaz9468

Ebitz RB, Hayden BY. 2021. The population doctrine in cognitive neuroscience. *Neuron* **109**:3055–3068. doi:10.1016/j.neuron.2021.07.011

Engelhard B, Finkelstein J, Cox J, Fleming W, Jang HJ, Ornelas S, Koay SA, Thiberge SY, Daw ND, Tank DW, Witten IB. 2019. Specialized coding of sensory, motor and cognitive variables in VTA dopamine neurons. *Nature* **570**:509–513. doi:10.1038/s41586-019-1261-9

Felsen G, Mainen ZF. 2008. Neural Substrates of Sensory-Guided Locomotor Decisions in the Rat Superior Colliculus. *Neuron* **60**:137–148. doi:10.1016/j.neuron.2008.09.019

Fujisawa S, Amarasingham A, Harrison MT, Buzsáki G. 2008. Behavior-dependent short-term assembly dynamics in the medial prefrontal cortex. *Nat Neurosci* **11**:823–833. doi:10.1038/nn.2134

Gadziola MA, Stetzik LA, Wright KN, Milton AJ, Arakawa K, del Mar Cortijo M, Wesson DW. 2020. A Neural System that Represents the Association of Odors with Rewarded Outcomes and Promotes Behavioral Engagement. *Cell Rep* **32**:107919. doi:10.1016/j.celrep.2020.107919

Gadziola MA, Tylicki KA, Christian DL, Wesson DW. 2015. The Olfactory Tubercle Encodes Odor Valence in Behaving Mice. *J Neurosci* **35**:4515–4527. doi:10.1523/JNEUROSCI.4750-14.2015

Gadziola MA, Wesson DW. 2016. The Neural Representation of Goal-Directed Actions and Outcomes in the Ventral Striatum's Olfactory Tubercle. *J Neurosci* **36**:548–560. doi:10.1523/JNEUROSCI.3328-15.2016

Gardner MPH, Sanchez D, Conroy JC, Wikenheiser AM, Zhou J, Schoenbaum G. 2020. Processing in Lateral Orbitofrontal Cortex Is Required to Estimate Subjective Preference during Initial, but Not Established, Economic Choice. *Neuron* **108**:526-537.e4. doi:10.1016/j.neuron.2020.08.010

Ghosh S, Larson SD, Hefzi H, Marnoy Z, Cutforth T, Dokka K, Baldwin KK. 2011. Sensory maps in the olfactory cortex defined by long-range viral tracing of single neurons. *Nature* **472**:217–220. doi:10.1038/nature09945

Gilbert CD, Sigman M. 2007. Brain States: Top-Down Influences in Sensory Processing. *Neuron* **54**:677–696. doi:10.1016/j.neuron.2007.05.019

Gill J V, Lerman GM, Zhao H, Stetler BJ, Rinberg D, Shoham S. 2020. Precise Holographic Manipulation of Olfactory Circuits Reveals Coding Features Determining Perceptual Detection. *Neuron* **108**:382-393.e5. doi:10.1016/j.neuron.2020.07.034

Gire DH, Whitesell JD, Doucette W, Restrepo D. 2013. Information for decision-making and stimulus identification is multiplexed in sensory cortex. *Nat Neurosci* **16**:991–993. doi:10.1038/nn.3432

Gore F, Schwartz EC, Brangers BC, Aladi S, Stujenske JM, Likhtik E, Russo MJ, Gordon JA, Salzman CD, Axel R. 2015. Neural Representations of Unconditioned

Stimuli in Basolateral Amygdala Mediate Innate and Learned Responses. *Cell* **162**:134–145. doi:10.1016/j.cell.2015.06.027

Gründemann J, Bitterman Y, Lu T, Krabbe S, Grewe BF, Schnitzer MJ, Lüthi A. 2019. Amygdala ensembles encode behavioral states. *Science* **364**:425736. doi:10.1126/science.aav8736

Haberly LB, Price JL. 1978. Association and commissural fiber systems of the olfactory cortex of the rat II. Systems originating in the olfactory peduncle. *J Comp Neurol* **181**:781–807. doi:10.1002/cne.901810407

Hagihara KM, Bukalo O, Zeller M, Aksoy-Aksel A, Karalis N, Limoges A, Rigg T, Campbell T, Mendez A, Weinholtz C, Mahn M, Zweifel LS, Palmiter RD, Ehrlich I, Lüthi A, Holmes A. 2021. Intercalated amygdala clusters orchestrate a switch in fear state. *Nature* **594**:403–407. doi:10.1038/s41586-021-03593-1

Hamid AA, Pettibone JR, Mabrouk OS, Hetrick VL, Schmidt R, Vander Weele CM, Kennedy RT, Aragona BJ, Berke JD. 2016. Mesolimbic dopamine signals the value of work. *Nat Neurosci* **19**:117–126. doi:10.1038/nn.4173

Hanks TD, Kopec CD, Brunton BW, Duan CA, Erlich JC, Brody CD. 2015. Distinct relationships of parietal and prefrontal cortices to evidence accumulation. *Nature* **520**:220–223. doi:10.1038/nature14066

Hirokawa J, Vaughan A, Masset P, Ott T, Kepecs A. 2019. Frontal cortex neuron types categorically encode single decision variables. *Nature* **576**:446–451. doi:10.1038/s41586-019-1816-9

Hoffmann LC, Berry SD. 2009. Cerebellar theta oscillations are synchronized during hippocampal theta-contingent trace conditioning. *Proc Natl Acad Sci* **106**:21371–21376. doi:10.1073/pnas.0908403106

Hoover WB, Vertes RP. 2011. Projections of the medial orbital and ventral orbital cortex in the rat. *J Comp Neurol* **519**:3766–3801. doi:10.1002/cne.22733

Hyman JM, Ma L, Balaguer-Ballester E, Durstewitz D, Seamans JK. 2012. Contextual encoding by ensembles of medial prefrontal cortex neurons. *Proc Natl Acad Sci* **109**:5086–5091. doi:10.1073/pnas.1114415109

Igarashi KM, Ieki N, An M, Yamaguchi Y, Nagayama S, Kobayakawa K, Kobayakawa R, Tanifuji M, Sakano H, Chen WR, Mori K. 2012. Parallel Mitral and Tufted Cell Pathways Route Distinct Odor Information to Different Targets in the Olfactory Cortex. *J Neurosci* **32**:7970–7985. doi:10.1523/JNEUROSCI.0154-12.2012

Ikemoto S. 2007. Dopamine reward circuitry: Two projection systems from the ventral midbrain to the nucleus accumbens–olfactory tubercle complex. *Brain Res Rev* **56**:27–78. doi:10.1016/j.brainresrev.2007.05.004

Ito M, Doya K. 2015. Distinct Neural Representation in the Dorsolateral, Dorsomedial, and Ventral Parts of the Striatum during Fixed- and Free-Choice Tasks. *J Neurosci* **35**:3499–3514. doi:10.1523/JNEUROSCI.1962-14.2015

Iwata M, Watanabe S, Yamane A, Miyasaka T, Misonou H. 2019. Regulatory mechanisms for the axonal localization of tau protein in neurons. *Mol Biol Cell* **30**:2441–2457. doi:10.1091/mbc.E19-03-0183

Janak PH, Tye KM. 2015. From circuits to behaviour in the amygdala. *Nature* **517**:284–292. doi:10.1038/nature14188

Jennings JH, Kim CK, Marshel JH, Raffiee M, Ye L, Quirin S, Pak S, Ramakrishnan C, Deisseroth K. 2019. Interacting neural ensembles in orbitofrontal cortex for social and feeding behaviour. *Nature* **565**:645–649. doi:10.1038/s41586-018-0866-8

Johnson DMG, Illig KR, Behan M, Haberly LB. 2000. New Features of Connectivity in Piriform Cortex Visualized by Intracellular Injection of Pyramidal Cells Suggest that “Primary” Olfactory Cortex Functions Like “Association” Cortex in Other Sensory Systems. *J Neurosci* **20**:6974–6982. doi:10.1523/JNEUROSCI.20-18-06974.2000

Jones MW, Wilson MA. 2005. Theta Rhythms Coordinate Hippocampal–Prefrontal Interactions in a Spatial Memory Task. *PLoS Biol* **3**:e402. doi:10.1371/journal.pbio.0030402

Joo HR, Liang H, Chung JE, Geaghan-Breiner C, Fan JL, Nachman BP, Kepecs A, Frank LM. 2021. Rats use memory confidence to guide decisions. *Curr Biol* **31**:4571-4583.e4. doi:10.1016/j.cub.2021.08.013

Josselyn SA, Köhler S, Frankland PW. 2015. Finding the engram. *Nat Rev Neurosci* **16**:521–534. doi:10.1038/nrn4000

Kay LM, Laurent G. 1999. Odor- and context-dependent modulation of mitral cell activity in behaving rats. *Nat Neurosci* **2**:1003–1009. doi:10.1038/14801

Kepecs A, Uchida N, Mainen ZF. 2007. Rapid and Precise Control of Sniffing During Olfactory Discrimination in Rats. *J Neurophysiol* **98**:205–213. doi:10.1152/jn.00071.2007

Kepecs A, Uchida N, Zariwala HA, Mainen ZF. 2008. Neural correlates, computation and behavioural impact of decision confidence. *Nature* **455**:227–231. doi:10.1038/nature07200

Kim HR, Malik AN, Mikhael JG, Bech P, Tsutsui-Kimura I, Sun F, Zhang Y, Li Y, Watabe-Uchida M, Gershman SJ, Uchida N. 2020. A Unified Framework for

Dopamine Signals across Timescales. *Cell* **183**:1600-1616.e25. doi:10.1016/j.cell.2020.11.013

Kobayakawa K, Kobayakawa R, Matsumoto H, Oka Y, Imai T, Ikawa M, Okabe M, Ikeda T, Itohara S, Kikusui T, Mori K, Sakano H. 2007. Innate versus learned odour processing in the mouse olfactory bulb. *Nature* **450**:503–508. doi:10.1038/nature06281

Larsson M, Willander J, Karlsson K, Arshamian A. 2014. Olfactory LOVER: behavioral and neural correlates of autobiographical odor memory. *Front Psychol* **5**:1–5. doi:10.3389/fpsyg.2014.00312

Lee CCY, Kheradpezhouh E, Diamond ME, Arabzadeh E. 2020. State-Dependent Changes in Perception and Coding in the Mouse Somatosensory Cortex. *Cell Rep* **32**:108197. doi:10.1016/j.celrep.2020.108197

Liu D, Deng J, Zhang Z, Zhang Z-Y, Sun Y-G, Yang T, Yao H. 2020. Orbitofrontal control of visual cortex gain promotes visual associative learning. *Nat Commun* **11**:2784. doi:10.1038/s41467-020-16609-7

Luskin MB, Price JL. 1983a. The topographic organization of associational fibers of the olfactory system in the rat, including centrifugal fibers to the olfactory bulb. *J Comp Neurol* **216**:264–291. doi:10.1002/cne.902160305

Luskin MB, Price JL. 1983b. The laminar distribution of intracortical fibers originating in the olfactory cortex of the rat. *J Comp Neurol* **216**:292–302. doi:10.1002/cne.902160306

Majkutewicz I, Cecot T, Jerzemowska G, Myślińska D, Plucińska K, Trojniar W, Wrona D. 2010. Lesion of the ventral tegmental area amplifies stimulation-induced Fos expression in the rat brain. *Brain Res* **1320**:95–105. doi:10.1016/j.brainres.2010.01.009

Manabe H, Kusumoto-Yoshida I, Ota M, Mori K. 2011. Olfactory Cortex Generates Synchronized Top-Down Inputs to the Olfactory Bulb during Slow-Wave Sleep. *J Neurosci* **31**:8123–8133. doi:10.1523/JNEUROSCI.6578-10.2011

Marshel JH, Kim YS, Machado TA, Quirin S, Benson B, Kadmon J, Raja C, Chibukhchyan A, Ramakrishnan C, Inoue M, Shane JC, McKnight DJ, Yoshizawa S, Kato HE, Ganguli S, Deisseroth K. 2019. Cortical layer–specific critical dynamics triggering perception. *Science* **365**. doi:10.1126/science.aaw5202

Mathis A, Mamidanna P, Cury KM, Abe T, Murthy VN, Mathis MW, Bethge M. 2018. DeepLabCut: markerless pose estimation of user-defined body parts with deep learning. *Nat Neurosci* **21**:1281–1289. doi:10.1038/s41593-018-0209-y

Matias S, Lottem E, Dugué GP, Mainen ZF. 2017. Activity patterns of serotonin neurons underlying cognitive flexibility. *Elife* **6**:1–24. doi:10.7554/eLife.20552

Menegas W, Babayan BM, Uchida N, Watabe-Uchida M. 2017. Opposite initialization to novel cues in dopamine signaling in ventral and posterior striatum in mice. *Elife* **6**:1–26. doi:10.7554/eLife.21886

Millman DJ, Murthy VN. 2020. Rapid Learning of Odor–Value Association in the Olfactory Striatum. *J Neurosci* **40**:4335–4347. doi:10.1523/JNEUROSCI.2604-19.2020

Miura K, Mainen ZF, Uchida N. 2012. Odor Representations in Olfactory Cortex: Distributed Rate Coding and Decorrelated Population Activity. *Neuron* **74**:1087–1098. doi:10.1016/j.neuron.2012.04.021

Miyamichi K, Amat F, Moussavi F, Wang C, Wickersham I, Wall NR, Taniguchi H, Tasic B, Huang ZJ, He Z, Callaway EM, Horowitz MA, Luo L. 2011. Cortical representations of olfactory input by trans-synaptic tracing. *Nature* **472**:191–196. doi:10.1038/nature09714

Morales M, Margolis EB. 2017. Ventral tegmental area: cellular heterogeneity, connectivity and behaviour. *Nat Rev Neurosci* **18**:73–85. doi:10.1038/nrn.2016.165

Mori K. 2010. [Odor map in the brain] Nou no naka no nioi chizu (in Japanese). PHP Science World.

Mori K, Sakano H. 2011. How Is the Olfactory Map Formed and Interpreted in the Mammalian Brain? *Annu Rev Neurosci* **34**:467–499. doi:10.1146/annurev-neuro-112210-112917

Murakami M, Kashiwadani H, Kirino Y, Mori K. 2005. State-Dependent Sensory Gating in Olfactory Cortex. *Neuron* **46**:285–296. doi:10.1016/j.neuron.2005.02.025

Murata K, Kanno M, Ieki N, Mori K, Yamaguchi M. 2015. Mapping of Learned Odor-Induced Motivated Behaviors in the Mouse Olfactory Tubercle. *J Neurosci* **35**:10581–10599. doi:10.1523/JNEUROSCI.0073-15.2015

Musall S, Kaufman MT, Juavinett AL, Gluf S, Churchland AK. 2019. Single-trial neural dynamics are dominated by richly varied movements. *Nat Neurosci* **22**:1677–1686. doi:10.1038/s41593-019-0502-4

Nagayama S. 2010. Differential Axonal Projection of Mitral and Tufted Cells in the Mouse Main Olfactory System. *Front Neural Circuits* **4**:1–8. doi:10.3389/fncir.2010.00120

Nieh EH, Schottdorf M, Freeman NW, Low RJ, Lewallen S, Koay SA, Pinto L, Gauthier JL, Brody CD, Tank DW. 2021. Geometry of abstract learned knowledge in the hippocampus. *Nature* **595**:80–84. doi:10.1038/s41586-021-03652-7

Ohnuki T, Osako Y, Manabe H, Sakurai Y, Hirokawa J. 2020. Dynamic coordination of the perirhinal cortical neurons supports coherent representations between task epochs. *Commun Biol* **3**:406. doi:10.1038/s42003-020-01129-3

Okada T, Kato D, Nomura Y, Obata N, Quan X, Morinaga A, Yano H, Guo Z, Aoyama Y, Tachibana Y, Moorhouse AJ, Matoba O, Takiguchi T, Mizobuchi S, Wake H. 2021. Pain induces stable, active microcircuits in the somatosensory cortex that provide a therapeutic target. *Sci Adv* **7**. doi:10.1126/sciadv.abd8261

Osako Y, Ohnuki T, Tanisumi Y, Shiotani K, Manabe H, Sakurai Y, Hirokawa J. 2021. Contribution of non-sensory neurons in visual cortical areas to visually guided decisions in the rat. *Curr Biol* **31**:2757-2769.e6. doi:10.1016/j.cub.2021.03.099

Ota K, Oisi Y, Suzuki T, Ikeda M, Ito Y, Ito T, Uwamori H, Kobayashi K, Kobayashi M, Odagawa M, Matsubara C, Kuroiwa Y, Horikoshi M, Matsushita J, Hioki H, Ohkura M, Nakai J, Oizumi M, Miyawaki A, Aonishi T, Ode T, Murayama M. 2021. Fast, cell-resolution, contiguous-wide two-photon imaging to reveal functional network architectures across multi-modal cortical areas. *Neuron* **109**:1810-1824.e9. doi:10.1016/j.neuron.2021.03.032

O'Doherty J, Rolls ET, Francis S, Bowtell R, McGlone F, Kobal G, Renner B, Ahne G. 2000. Sensory-specific satiety-related olfactory activation of the human orbitofrontal cortex. *Neuroreport* **11**:893–897. doi:10.1097/00001756-200003200-00046

Parker PRL, Brown MA, Smear MC, Niell CM. 2020. Movement-Related Signals in Sensory Areas: Roles in Natural Behavior. *Trends Neurosci* **43**:581–595. doi:10.1016/j.tins.2020.05.005

Pashkovski SL, Iurilli G, Brann D, Chicharro D, Drummey K, Franks KM, Panzeri S, Datta SR. 2020. Structure and flexibility in cortical representations of odour space. *Nature* **583**:253–258. doi:10.1038/s41586-020-2451-1

Pho GN, Goard MJ, Woodson J, Crawford B, Sur M. 2018. Task-dependent representations of stimulus and choice in mouse parietal cortex. *Nat Commun* **9**:2596. doi:10.1038/s41467-018-05012-y

Price JL. 1973. An autoradiographic study of complementary laminar patterns of termination of afferent fibers to the olfactory cortex. *J Comp Neurol* **150**:87–108. doi:10.1002/cne.901500105

Radvansky BA, Oh JY, Climer JR, Dombeck DA. 2021. Behavior determines the hippocampal spatial mapping of a multisensory environment. *Cell Rep* **36**:109444. doi:10.1016/j.celrep.2021.109444

Ramesh RN, Burgess CR, Sugden AU, Gyetvan M, Andermann ML. 2018. Intermingled Ensembles in Visual Association Cortex Encode Stimulus Identity or Predicted Outcome. *Neuron* **100**:900-915.e9. doi:10.1016/j.neuron.2018.09.024

Ray JP, Russchen FT, Fuller TA, Price JL. 1992. Sources of presumptive glutamatergic/aspartatergic afferents to the mediodorsal nucleus of the thalamus in the rat. *J Comp Neurol* **320**:435–456. doi:10.1002/cne.903200403

Reinert S, Hübener M, Bonhoeffer T, Goltstein PM. 2021. Mouse prefrontal cortex represents learned rules for categorization. *Nature* **593**:411–417. doi:10.1038/s41586-021-03452-z

Rennaker RL, Chen C-FF, Ruyle AM, Sloan AM, Wilson DA. 2007. Spatial and Temporal Distribution of Odorant-Evoked Activity in the Piriform Cortex. *J Neurosci* **27**:1534–1542. doi:10.1523/JNEUROSCI.4072-06.2007

Robinson NTM, Descamps LAL, Russell LE, Buchholz MO, Bicknell BA, Antonov GK, Lau JYN, Nutbrown R, Schmidt-Hieber C, Häusser M. 2020. Targeted

Activation of Hippocampal Place Cells Drives Memory-Guided Spatial Behavior. *Cell* **183**:1586-1599.e10. doi:10.1016/j.cell.2020.09.061

Roelfsema PR, de Lange FP. 2016. Early Visual Cortex as a Multiscale Cognitive Blackboard. *Annu Rev Vis Sci* **2**:131–151. doi:10.1146/annurev-vision-111815-114443

Roesch MR, Stalnaker TA, Schoenbaum G. 2006. Associative Encoding in Anterior Piriform Cortex versus Orbitofrontal Cortex during Odor Discrimination and Reversal Learning. *Cereb Cortex* **17**:643–652. doi:10.1093/cercor/bhk009

Rolls ET. 2004. The functions of the orbitofrontal cortex. *Brain Cogn* **55**:11–29. doi:10.1016/S0278-2626(03)00277-X

Rolls ET. 2000. The Orbitofrontal Cortex and Reward. *Cereb Cortex* **10**:284–294. doi:10.1093/cercor/10.3.284

Root CM, Denny CA, Hen R, Axel R. 2014. The participation of cortical amygdala in innate, odour-driven behaviour. *Nature* **515**:269–273. doi:10.1038/nature13897

Rubin A, Sheintuch L, Brande-Eilat N, Pinchasof O, Rechavi Y, Geva N, Ziv Y. 2019. Revealing neural correlates of behavior without behavioral measurements. *Nat Commun* **10**:4745. doi:10.1038/s41467-019-12724-2

Sadakane O, Masamizu Y, Watakabe A, Terada S-I, Ohtsuka M, Takaji M, Mizukami H, Ozawa K, Kawasaki H, Matsuzaki M, Yamamori T. 2015. Long-Term Two-Photon Calcium Imaging of Neuronal Populations with Subcellular Resolution in Adult Non-human Primates. *Cell Rep* **13**:1989–1999. doi:10.1016/j.celrep.2015.10.050

Sakurai Y, Osako Y, Tanisumi Y, Ishihara E, Hirokawa J, Manabe H. 2018. Multiple Approaches to the Investigation of Cell Assembly in Memory Research—Present and Future. *Front Syst Neurosci* **12**:1–13. doi:10.3389/fnsys.2018.00021

Sanhueza M, Bacigalupo J. 2005. Intrinsic subthreshold oscillations of the membrane potential in pyramidal neurons of the olfactory amygdala. *Eur J Neurosci* **22**:1618–1626. doi:10.1111/j.1460-9568.2005.04341.x

Santiago AC, Shammah-Lagnado SJ. 2004. Efferent connections of the nucleus of the lateral olfactory tract in the rat. *J Comp Neurol* **471**:314–332. doi:10.1002/cne.20028

Scalia F, Winans SS. 1975. The differential projections of the olfactory bulb and accessory olfactory bulb in mammals. *J Comp Neurol* **161**:31–55. doi:10.1002/cne.901610105

Schoonover CE, Ohashi SN, Axel R, Fink AJP. 2021. Representational drift in primary olfactory cortex. *Nature* **594**:541–546. doi:10.1038/s41586-021-03628-7

Schuck NW, Cai MB, Wilson RC, Niv Y. 2016. Human Orbitofrontal Cortex Represents a Cognitive Map of State Space. *Neuron* **91**:1402–1412. doi:10.1016/j.neuron.2016.08.019

Sevelinges Y, Gervais R, Messaoudi B, Granjon L, Mouly A-M. 2004. Olfactory fear conditioning induces field potential potentiation in rat olfactory cortex and amygdala. *Learn Mem* **11**:761–769. doi:10.1101/lm.83604

Shepherd GM. 2011. Neurogastronomy. New York Chichester, West Sussex: Columbia University Press. doi:10.7312/shep15910

Shepherd GM. 2006. Smell images and the flavour system in the human brain. *Nature* **444**:316–321. doi:10.1038/nature05405

Shepherd GM. 2004. The Synaptic Organization of the Brain, 5th ed. New York: Oxford University Press. doi:10.1093/acprof:oso/9780195159561.001.1

Shimbo A, Izawa E-I, Fujisawa S. 2021. Scalable representation of time in the hippocampus. *Sci Adv* **7**. doi:10.1126/sciadv.abd7013

Shiotani K, Tanisumi Y, Hirokawa J, Sakurai Y, Manabe H. 2020a. Encoding of odor information and reward anticipation in anterior cortical amygdaloid nucleus. *bioRxiv* 2020.11.19.390740. doi:https://doi.org/10.1101/2020.11.19.390740

Shiotani K, Tanisumi Y, Murata K, Hirokawa J, Sakurai Y, Manabe H. 2020b. Tuning of olfactory cortex ventral tenia tecta neurons to distinct task elements of goal-directed behavior. *Elife* **9**:1–24. doi:10.7554/eLife.57268

Song MR, Lee SW. 2020. Dynamic resource allocation during reinforcement learning accounts for ramping and phasic dopamine activity. *Neural Networks* **126**:95–107. doi:10.1016/j.neunet.2020.03.005

Sosulski DL, Bloom ML, Cutforth T, Axel R, Datta SR. 2011. Distinct representations of olfactory information in different cortical centres. *Nature* **472**:213–216. doi:10.1038/nature09868

Speed A, Haider B. 2021. Probing mechanisms of visual spatial attention in mice. *Trends Neurosci* **44**:822–836. doi:10.1016/j.tins.2021.07.009

Spellman T, Svei M, Liston C. 2020. Prefrontal Deep Projection Neurons Enable Cognitive Flexibility Via Persistent Feedback Monitoring. *SSRN Electron J* 1–17. doi:10.2139/ssrn.3520957

Steinmetz NA, Aydin C, Lebedeva A, Okun M, Pachitariu M, Bauza M, Beau M, Bhagat J, Böhm C, Broux M, Chen S, Colonell J, Gardner RJ, Karsh B, Kloosterman F, Kostadinov D, Mora-Lopez C, O'Callaghan J, Park J, Putzeys J, Sauerbrei B, van Daal RJJ, Vollan AZ, Wang S, Welkenhuysen M, Ye Z, Dudman JT, Dutta B, Hantman AW, Harris KD, Lee AK, Moser EI, O'Keefe J, Renart A, Svoboda K, Häusser M, Haesler S, Carandini M, Harris TD. 2021. Neuropixels 2.0: A miniaturized high-density probe for stable, long-term brain recordings. *Science* **372**. doi:10.1126/science.abf4588

Steinmetz NA, Zatka-Haas P, Carandini M, Harris KD. 2019. Distributed coding of choice, action and engagement across the mouse brain. *Nature* **576**:266–273. doi:10.1038/s41586-019-1787-x

Stephenson-Jones M, Bravo-Rivera C, Ahrens S, Furlan A, Xiao X, Fernandes-Henriques C, Li B. 2020. Opposing Contributions of GABAergic and Glutamatergic Ventral Pallidal Neurons to Motivational Behaviors. *Neuron* **105**:921-933.e5. doi:10.1016/j.neuron.2019.12.006

Stettler DD, Axel R. 2009. Representations of Odor in the Piriform Cortex. *Neuron* **63**:854–864. doi:10.1016/j.neuron.2009.09.005

Stringer C, Michaelos M, Tsyboulski D, Lindo SE, Pachitariu M. 2021. High-precision coding in visual cortex. *Cell* **184**:2767-2778.e15. doi:10.1016/j.cell.2021.03.042

Stringer C, Pachitariu M, Steinmetz N, Reddy CB, Carandini M, Harris KD. 2019. Spontaneous behaviors drive multidimensional, brainwide activity. *Science* **364**. doi:10.1126/science.aav7893

Swanson LW, Petrovich GD. 1998. What is the amygdala? *Trends Neurosci* **21**:323–331. doi:10.1016/S0166-2236(98)01265-X

Takahashi S. 2015. Episodic-like memory trace in awake replay of hippocampal place cell activity sequences. *Elife* **4**:1–22. doi:10.7554/eLife.08105

Takamiya S, Shiotani K, Ohnuki T, Osako Y, Tanisumi Y, Yuki S, Manabe H, Hirokawa J, Sakurai Y. 2021. Hippocampal CA1 Neurons Represent Positive Feedback During the Learning Process of an Associative Memory Task. *Front Syst Neurosci* **15**:1–8. doi:10.3389/fnsys.2021.718619

Takehara-Nishiuchi K, Maal-Bared G, Morrissey MD. 2012. Increased Entorhinal–Prefrontal Theta Synchronization Parallels Decreased Entorhinal–Hippocampal Theta Synchronization during Learning and Consolidation of Associative Memory. *Front Behav Neurosci* **5**:1–13. doi:10.3389/fnbeh.2011.00090

Tanabe T, Iino M, Takagi SF. 1975. Discrimination of odors in olfactory bulb, pyriform-amygdaloid areas, and orbitofrontal cortex of the monkey. *J Neurophysiol* **38**:1284–1296. doi:10.1152/jn.1975.38.5.1284

Tanisumi Y, Shiotani K, Hirokawa J, Sakurai Y, Manabe H. 2021. Bi-directional encoding of context-based odors and behavioral states by the nucleus of the lateral olfactory tract. *iScience* **24**:102381. doi:10.1016/j.isci.2021.102381

Tonegawa S, Morrissey MD, Kitamura T. 2018. The role of engram cells in the systems consolidation of memory. *Nat Rev Neurosci* **19**:485–498. doi:10.1038/s41583-018-0031-2

Uchida N, Poo C, Haddad R. 2014. Coding and Transformations in the Olfactory System. *Annu Rev Neurosci* **37**:363–385. doi:10.1146/annurev-neuro-071013-013941

Vaz RP, Cardoso A, Sá SI, Pereira PA, Madeira MD. 2017. The integrity of the nucleus of the lateral olfactory tract is essential for the normal functioning of the olfactory system. *Brain Struct Funct* **222**:3615–3637. doi:10.1007/s00429-017-1422-2

Vaz RP, Pereira PA, Madeira MD. 2016. Age effects on the nucleus of the lateral olfactory tract of the rat. *J Comp Neurol* **524**:759–771. doi:10.1002/cne.23863

Wang X-J. 2021. 50 years of mnemonic persistent activity: quo vadis? *Trends Neurosci* **44**:888–902. doi:10.1016/j.tins.2021.09.001

Watabe-Uchida M, Eshel N, Uchida N. 2017. Neural Circuitry of Reward Prediction Error. *Annu Rev Neurosci* **40**:373–394. doi:10.1146/annurev-neuro-072116-031109

Yarita H, Iino M, Tanabe T, Kogure S, Takagi SF. 1980. A transthalamic olfactory pathway to orbitofrontal cortex in the monkey. *J Neurophysiol* **43**:69–85. doi:10.1152/jn.1980.43.1.69

Yoshihara C, Tokita K, Maruyama T, Kaneko M, Tsuneoka Y, Fukumitsu K, Miyazawa E, Shinozuka K, Huang AJ, Nishimori K, McHugh TJ, Tanaka M, Itohara S, Touhara K, Miyamichi K, Kuroda KO. 2021. Calcitonin receptor signaling in the medial preoptic area enables risk-taking maternal care. *Cell Rep* **35**:109204. doi:10.1016/j.celrep.2021.109204

Yoshizawa T, Ito M, Doya K. 2018. Reward-Predictive Neural Activities in Striatal Striosome Compartments. *eneuro* **5**:ENEURO.0367-17.2018. doi:10.1523/ENEURO.0367-17.2018

Zatka-Haas P, Steinmetz NA, Carandini M, Harris KD. 2021. Sensory coding and the causal impact of mouse cortex in a visual decision. *Elife* **10**:1–25. doi:10.7554/eLife.63163

Zhan C, Luo M. 2010. Diverse Patterns of Odor Representation by Neurons in the Anterior Piriform Cortex of Awake Mice. *J Neurosci* **30**:16662–16672. doi:10.1523/JNEUROSCI.4400-10.2010

Zhang S, Xu M, Kamigaki T, Hoang Do JP, Chang W-C, Jenvay S, Miyamichi K, Luo L, Dan Y. 2014. Long-range and local circuits for top-down modulation of visual cortex processing. *Science* **345**:660–665. doi:10.1126/science.1254126

Zhang X, Guan W, Yang T, Furlan A, Xiao X, Yu K, An X, Galbavy W, Ramakrishnan C, Deisseroth K, Ritola K, Hantman A, He M, Josh Huang Z, Li B. 2021. Genetically identified amygdala–striatal circuits for valence-specific behaviors. *Nat Neurosci* **24**:1586–1600. doi:10.1038/s41593-021-00927-0

Zucco GM, Aiello L, Turuani L, Koster E. 2012. Odor-Evoked Autobiographical Memories: Age and Gender Differences Along the Life Span. *Chem Senses* **37**:179–189. doi:10.1093/chemse/bjr089